Magnetic Domains and Domain Wall Oscillations in Planar and 3D Curved Membranes

Dissertation

zur Erlangung des akademischen Grades
Doctor rerum naturalium
(Dr. rer. nat.)

vorgelegt dem
Bereich Mathematik und Naturwissenschaften
der Technischen Universität Dresden

von

M.Sc. Balram Singh

Gutachter:
Prof. Dr. Oliver G. Schmidt
Prof. Dr. Sibylle Gemming

Dresden, den 24 Februar 2023

Balram Singh, M.Sc.

Magnetic Domains and Domain Wall Oscillations in Planar and 3D Curved Membranes

Technical University Dresden, 2023
Nanophysics, Institute of Applied Physics

Keywords: self-assembly rolling, 3D microscale curved structures, strain-induced anisotropy, anisotropic magnetoresistance, integrated strain sensors, Landau domain configuration, magnetic force microscopy, nanoscale imaging, domain wall oscillations, time-averaged imaging

Abstract

This dissertation presents a substantial contribution to a new field of material science, the investigation of the magnetic properties of 3D curved surfaces, achieved by using a self-assembled geometrical transformation of an initially planar membrane. Essential magnetic properties of thin films can be modified by the process of transforming them from a 2D planar film to a 3D curved surface. By investigating and controlling the reasons that influence the properties, it is possible to improve the functionality of existing devices in addition to laying the foundation for the future development of microelectronic devices based on curved magnetic structures. To accomplish this, it is necessary both to fabricate high-quality 3D curved objects and to establish reliable characterization methods based on commonly available technology.

The primary objective of this dissertation is to develop techniques for characterizing the static and dynamic magnetic properties of self-assembled rolled 3D geometries. The second objective is to examine the origin of shape-, size- and strain/curvature-induced effects.

The developed approach based on anisotropic magnetoresistance (AMR) measurement can quantitatively define the rolling-induced static magnetic changes, namely the induced magnetoelastic anisotropy, thus eliminating the need for microscopic imaging to characterize the structures. The interpretation of the AMR signal obtained on curved stripes is enabled by simultaneous visualization of the domain patterns and micromagnetic simulations. The developed approach is used to examine the effect of sign and magnitude of curvature on the induced anisotropies by altering the rolling direction and diameter of the "Swiss-roll".

Furthermore, a time-averaged imaging technique based on conventional microscopies (magnetic force microscopy and Kerr microscopy) offers a novel strategy for investigating nanoscale periodic domain wall oscillations and hence dynamic magnetic characteristics of flat and curved structures. This method exploits the benefit of a position-dependent dwell time of periodically oscillating DWs and can determine the trajectory and amplitude of DW oscillation with sub-100 nm resolution. The uniqueness of this technique resides in the ease of the imaging procedure, unlike other DW dynamics imaging methods.

The combined understanding of rolling-induced anisotropy and imaging DW oscillation is utilized to examine the dependence of DW dynamics on external stimuli and the structure's physical properties, such as lateral size, film thickness, and curvature-induced anisotropy. The presented methods and fundamental studies help to comprehend the rapidly expanding field of 3-dimensional nanomagnetism and advance high-performance magneto-electronic devices based on self-assembly rolling.

Table of Contents

Abstract III
Table of Contents V
Acronyms and Symbols VIII

1. INTRODUCTION 1

1.1. MOTIVATION 1
1.1.1. MAGNETOELECTRONIC DEVICES BASED ON TUBULAR GEOMETRIES 1
1.1.2. MAGNETOPHORETIC DEVICES 3
1.1.3. CONCEPT FOR FUTURE ELECTRONIC DEVICES BASED ON MOVING DOMAIN WALLS 4

1.2. OBJECTIVE AND STRUCTURE OF DISSERTATION 8

2. SCIENTIFIC BACKGROUND 10

2.1. MAGNETISM AND MAGNETIC ENERGY DENSITIES 10
2.1.1. MAGNETOCRYSTALLINE ANISOTROPY 14
2.1.2. DEMAGNETIZING ENERGY 14
2.1.3. PHYSICAL ORIGIN OF SHAPE ANISOTROPY 16
2.1.4. MAGNETOSTRICTION 17
2.1.5. MAGNETOELASTIC EFFECT 18
2.1.6. PERMEABILITY 19

2.2. MAGNETIZATION DYNAMICS 20
2.2.1. LANDAU-LIFSHITZ-GILBERT EQUATION 20
2.2.2. DOMAIN WALL DYNAMICS IN PLANAR STRUCTURES 21
2.2.3. TECHNIQUES TO INVESTIGATE DOMAIN WALL OSCILLATIONS 23

2.3. CURVATURE-INDUCED MAGNETISM 26
2.3.1. CYLINDRICAL NANOTUBES 27
2.3.2. CYLINDRICAL MICROTUBULAR ARCHITECTURES 31
2.3.3. FABRICATION OF CYLINDRICAL TUBULAR GEOMETRIES 33
2.3.4. CHARACTERIZATION OF TUBULAR GEOMETRIES 36

3. FABRICATION METHODS 40

3.1. FABRICATION OF PLANAR STRUCTURES 40
3.1.1. DEPOSITION TECHNIQUES 40
3.1.2. LITHOGRAPHY PROCESSES 41

3.2. PREPARATION OF CURVED SURFACES 44
3.2.1. POLYMER FABRICATION PROCESS 47

4. Characterization Methods 50

4.1. Magnetic force microscopy 50

4.2. Kerr microscopy 53

4.3. Micromagnetic simulations 56

4.4. Electrical characterization & magneto-transport 58
  4.4.1. Anisotropic magnetoresistance (AMR) 58
  4.4.2. Microscopic calculation of AMR 59

5. Induced Anisotropies in Curved Magnetic Membranes 61

5.1. Rolled-down and rolled-up microelements 61
  5.1.1. Magnetic domains 63
  5.1.2. Magnetization reversal with an axial field 64
  5.1.3. Magnetization reversal with a transverse field 69

5.2. Curvature tuning of rolled-down magnetic structures 72
  5.2.1. Surface strain estimation 73
  5.2.2. Quantification of strain-induced anisotropy 75

5.3. Micro-magnetic simulations 76
  5.3.1. Magnetization reversal with an axial field 76
  5.3.2. Magnetization reversal with a transverse field 79

5.4. Conclusion 80

6. Direct Imaging of Nanoscale Domain Wall Oscillations 82

6.1. MFM Imaging 82
  6.1.1. Magnetic domain walls 82
  6.1.2. Real-time imaging 83
  6.1.3. Time-averaged imaging 84

6.2. Time-averaged Kerr imaging 89

6.3. Influence of structure size and thickness 92

6.4. Micromagnetic simulations 94
  6.4.1. Influence of structure size and thickness 94

6.5. Conclusion 99

7. Domain wall Dynamics of Rolled Membranes 100

7.1. Magnetic domains and domain wall oscillations 100

7.2. Micromagnetic simulations 102

7.3. Conclusion 105

8. CONCLUSION & OUTLOOK 106

8.1. INDUCED ANISOTROPIES IN CURVED MAGNETIC MEMBRANES 107
8.1.1. OUTLOOK 107

8.2. DW OSCILLATIONS IN PLANAR AND CURVED STRUCTURES 108
8.2.1. OUTLOOK 109

Bibliography 112
List of Figures and Tables 122
Selbstständigkeitserklärung 124
Acknowledgements 126
List of Publications 128
List of Presentations 129
Curriculum Vitae 131

Acronyms and Symbols

Acronyms

2D	two-dimensional
3D	three-dimensional
ac	alternating current
dc	direct current
AMR	anisotropic magnetoresistance
GMI	giant magnetoimpedance
DMI	Dzyaloshinskii-Moriya interaction
MOKE	magnetooptical Kerr effect
MFM	magnetic force microscopy
DW	domain wall
SPM	superparamagnetic
XMCD	X-ray magnetic circular dichroism
EM	electromagnetic
KB	kilobyte
MB	megabyte
TB	terabyte

Symbols

ϕ	diameter
ε	lateral strain
μ_0	vacuum permeability
μ_m	domain wall mobility

c	DW stiffness parameter
E_{ex}	exchange energy density
E_{demag}	demagnetizing energy density
E_{aniso}	anisotropy energy density
E_{UMA}	uniaxial magnetic anisotropy energy density
E_{total}	total energy density
p	position
t	time
d	thickness
W	width
L	length
$\mathbf{H}$	magnetic field
K_{u}	uniaxial magnetic anisotropy
M_{s}	saturation magnetization
$\mathbf{M}$	magnetization
$\mathbf{m}$	normalized magnetization
R	radius of curvature
l_x	exchange length
Py	Permalloy
N	demagnetizing factor
k	restoring force constant
l	length of the pendulum
g	gravitational constant
m	mass of the pendulum

Chapter 1 INTRODUCTION

Humans have been fascinated by magnetism ever since the discovery of the first magnetic stones, which were created by volcanic action. Since 1845, these stones have been known as magnetite. In the sixth century B.C., the Greek philosopher Thales of Miletus observed the extraordinary effects that these stones could move and stated that they contain souls. According to the ancient Greeks, the unseen force responsible for the movement was a manifestation of inner liveliness. Quantum theory successfully explained these effects during the early 20th century. According to that theory, the vector quantity magnetic moment originates mainly from a set of electrons revolving in fixed orbits around a nucleus in an atom.

Moreover, a quantum mechanical interaction between adjacent moments determines the magnetic characteristics and magnetization configuration of a whole magnetic sample. Magnetization configuration comprises magnetic domains and interfaces known as domain walls (DWs) separating these domains. Appropriate external actions can generate, manipulate, and annihilate them. The combination of stability and the flexibility to control the magnetization configuration makes magnetic materials particularly desirable for field sensors, magnetophoretic and memory devices.

1.1. MOTIVATION

1.1.1. MAGNETOELECTRONIC DEVICES BASED ON TUBULAR GEOMETRIES

In the field of 3D shapeable magnetoelectronics, the reshaping of magnetic materials may alter their domain pattern, and thus affecting electronic device behavior. Magnetic field sensors based on the magnetoresistance effect in soft ferromagnetic tubular geometries are crucial for position control in robotics and e-skin applications. [1–6] The performance of these 3D magnetic sensors is intimately connected to features of the functional material, such as residual strain, magnetic domain orientation, and magnetization rotation, which are the result of anisotropy induced during the device's transformation from a 2D membrane to a 3D architecture.

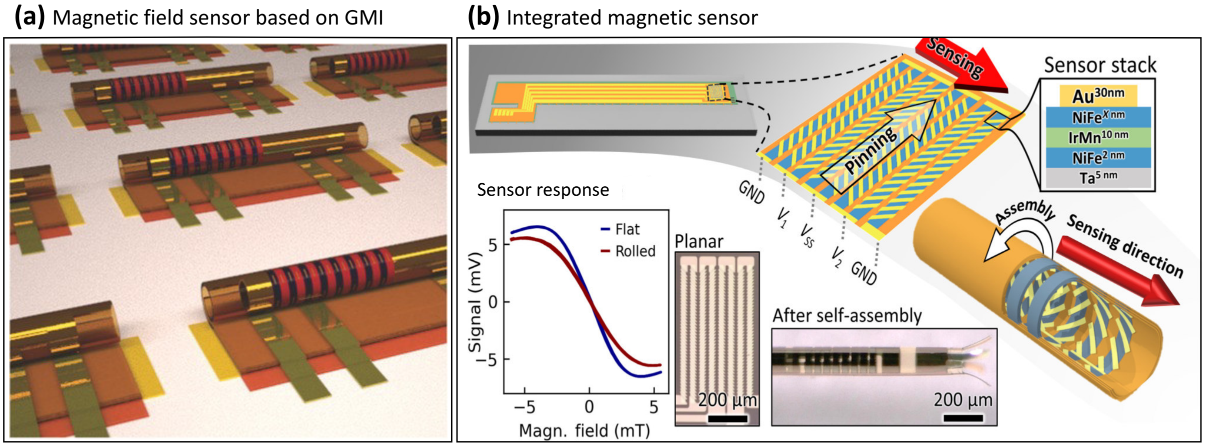
(a) Magnetic field sensor based on GMI

(b) Integrated magnetic sensor

Figure 1.1: Field sensors based on magnetoresistance. (a) The on-chip-integrated array of giant magneto-impedance (GMI) sensors equipped with pick-up coils (taken from[1]) and **(b)** anisotropic magnetoresistance (AMR) sensors fully integrated into micro-catheters by rolling a planar layer stack into self-assembled 3D architectures using strain engineering (taken from[3] under the term of CC BY license).

The highly sensitive nature of recently shown field sensors based on the GMI effect (Figure **1**a) benefits from the geometrically induced highly stable azimuthal domains achieved by changing the 2D $Ni_{81}Fe_{19}$ membrane into a 3D tubular architecture.[1] These compact microscale sensors offer an excellent alternative to atom-vapor-deposited magnetometers[7] and SQUIDs[8] for magnetoencephalography[8] applications by detecting the small magnetic fields generated by brain activity in neural tissue. However, attaining controlled azimuthal domain configuration in rolled permalloy membranes with permalloy composition close to zero magnetostriction remains difficult. In addition, learning what causes the GMI effect necessitates the development of an imaging technique capable of probing local ac-excited magnetization processes in the MHz frequency range. In contrast, for flexible and stretchable magnetoelectronic applications, researchers have worked to reduce the magnetosensitive capabilities and produce stable magnetic properties under deformation or strains (Figure **1**b).[2,3,5,6,9–11]

Because of this, future magnetoelectronic systems requiring a 3D shape would benefit greatly from research into the relationship between strain and static and dynamic magnetic characteristics of soft ferromagnetic thin film structures, including the possibility of probing them using magnetoresistance measurements.

1.1.2. MAGNETOPHORETIC DEVICES

Domain walls (DWs, width 10–100 nm) are nanoscale magnetic entities that generate significantly inhomogeneous near-surface fields. These serve as a pinning potential for magnetic micro-/nanoparticles above the DW (Figure **2**a). The force exerted by stray fields on a magnetic particle depends on the strength of the stray field **B**, the volume V, and the magnetic susceptibility of the particle χ_{v}, which can be written as follows;[12]

$$F = \left({\chi_{\mathrm{v}} V}/{2\mu_0} \right) \nabla(\mathbf{B} \cdot \mathbf{B}) \tag{1.1}$$

The controlled DW motion can precisely manipulate, and transport coupled magnetic beads. A sinusoidal oscillation of a magnetic bead coupled to a DW and observed under an optical microscope is utilized to assess the magnetic bead's mechanical characteristics, such as its resonance frequency (Figures **2**b–e).[13] It was shown that a super paramagnetic (SPM) bead trapped by a domain wall exhibits a distinct magneto-mechanical behavior that depends on its hydrodynamic characteristics in the host fluid. Such behavior offers means to distinguish single SPM and attached substances based on their physical characteristics. By measuring the mechanical response of SPMs trapped by a domain wall, driven sinusoidally up to 1 kHz, it was shown that a characteristic frequency exists that is a function of the SPM conformation and the strength of its interaction with the domain wall.

Thus, a dynamic motion of the domain walls provided a new approach for mechanical characterization of small-scale systems. As a result, establishing approaches to characterize oscillating DW and control the oscillation amplitude in the kHz frequency range and above would support the understanding of magnetophoretic devices.

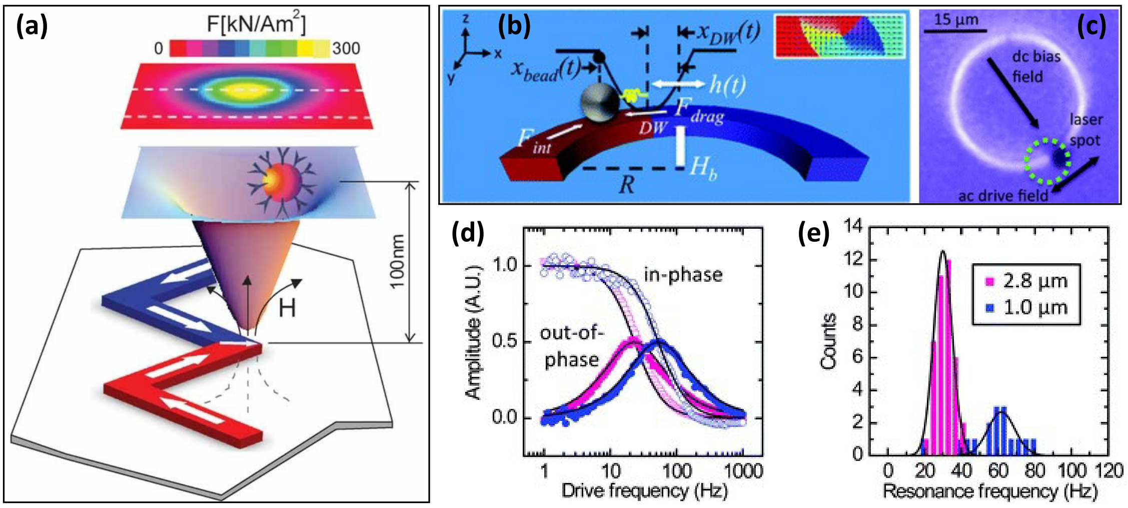

Figure 1.2: Magnetic bead manipulation using domain wall: (a) A magnetic bead trapped in a domain wall stray-field-generated attractive potential (taken from[14]). **(b)** Schematic of the coupled bead-DW system with the curved track. **(c)** Optical image of a 2.8 µm diameter superparamagnetic (SPM) bead trapped in a $Ni_{80}Fe_{20}$ track that is 800 nm wide and 40 nm thick. **(d)** Resonant excitation of a trapped SPM bead in an aqueous environment by an oscillating DW in a circular magnetic track. The curves depict in-phase and out-of-phase optical reflectivity signals that are approximately proportional to the amplitude of the bead oscillation. Two colors correspond to two microbead diameters, 2.8 µm, and 1.0 µm. **(e)** Histograms of resonance frequency measurements with mean resonance frequencies of 30.3 Hz and 58.3 Hz for 2.8 µm and 1.0 µm beads, respectively. ((b)-(e) Taken from[15]).

1.1.3. CONCEPT FOR FUTURE ELECTRONIC DEVICES BASED ON MOVING DOMAIN WALLS

After the 1898 demonstration by Danish engineer Valdemar Poulson that a magnetic medium might be used to record and playback information, there has been an ongoing effort to improve these devices by increasing their density and speed of storage. As a result, modern hard disk drives (HDDs) have an areal density of approximately 1 TB.[in]$^{-2}$,[16–18] which is about a billion times greater than the first HDD released in 1956 with a total storage capacity of 5 MB at a recording density of 2KB.[in]$^{-2}$. However, when considering the data growth pace, the demand is larger than what is currently available. In addition, reducing the energy needed for data storage and processing is a significant obstacle. In response to these issues, scientists came up with the concept of memory devices based on controlled domain wall unidirectional motion powered by dc-field or current.[19] The performance and efficiency of these devices are determined by the DW's speed and the threshold excitation strength necessary to displace the DW, respectively. Thus, for reliable device functioning, high domain wall velocity and sufficiently low current densities (to minimize energy dissipation) are necessary. In planar nanowires, however, the speed of the unidirectional DW motion is limited by the fact that DW structures collapse above a threshold velocity, a phenomenon known as Walker breakdown.[20] Recent simulation studies suggested that the curvature and geometry-induced effect (removal of side edges) suppressed the Walker breakdown in soft ferromagnetic nanotubes, resulting in a much higher domain wall velocity of the order of a few km[sec]$^{-1}$ compared to their planar counterparts (Figure **1.3**a).[21] As a result, nanotube-based devices are likely to perform better. Furthermore, ac-current-induced oscillatory DW dynamics are claimed to be driven by a significantly lower threshold current density than dc-current-induced DW motion in planar nanowires (Figure 1.3b).[13] As a result, systems based on oscillatory DW motion dissipate less heat and can thus be more efficient. As a result of combining the faster DW attribute of tubular geometry with the lower threshold current density characteristic of oscillatory dynamics, oscillatory DW dynamics in tubular geometry are expected to provide novel opportunities for future DW-based magnetoelectronic devices with improved performance and efficiency. (Figure **1.3**c).

Aside from the previously described field/current driven faster DW dynamics of nanotubes, theoretical investigations revealed that, for wires with monotonic increasing/decreasing curvature as a function of arc length, the curvature gradient results in a driving force, i.e., the DW moves in the absence of any external driving force (field/current). The curvature induced DMI resulting from the exchange interaction is the physical origin of this force. Depending on the magnitude of the wire's curvature gradient, the corresponding geometry-induced DW velocity can reach up to 150 m[sec]$^{-1}$.[22] Although the curvature-induced exchange-driven effects are generic, it is challenging to observe them in experiments because they are shaded by other effects and interactions, such as long-range magnetostatic interactions.

(a) Dc-field induced fast DW dynamics in nanotubes

(b) Ac-current-induced DW oscillations in planar nanostripes

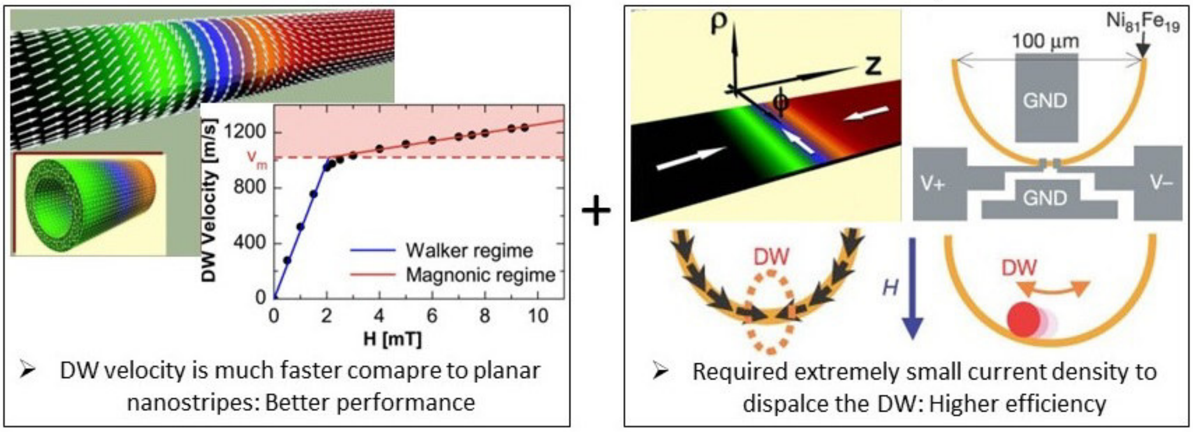

➢ DW velocity is much faster comapre to planar nanostripes: Better performance

➢ Required extremely small current density to dispalce the DW: Higher efficiency

=

(c) Ac-current induced DW oscillations in nanotubes

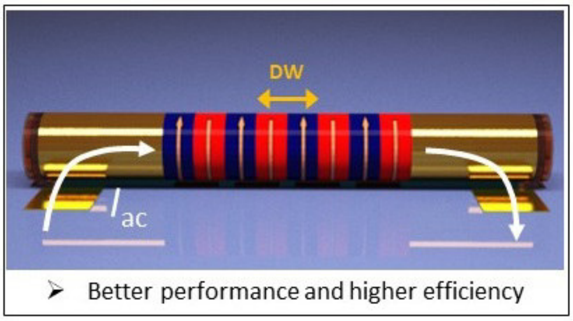

➢ Better performance and higher efficiency

Figure 1.3: DW dynamics in nanostructures. (a) A vortex DW formed in permalloy tube of dimensions: L = 4 µm, ϕ_{outer} = 60 nm and d = 10 nm and DW velocity as a function of field applied along the length of the tube (taken from[21]). **(b)** A transverse DW formed in permalloy stripe forming semicircle loop of dimensions: radius 50 µm, W = 70 nm and d = 45 nm. Schematic depicting the DW magnetostatic potential energy in a magnetic field (taken from[13,21]**). (c)** Schematic diagram depicting the ac-current driven DW oscillations in tubular geometry having azimuthal domains. Image (c) credit goes to, Dr. Daniil Karnaushenko (MAIN Chemnitz).

However, a few key obstacles must be overcome in order to make progress in the aforementioned areas.

First, a deeper understanding of the origin of static domain configuration in soft ferromagnetic tubular geometries, particularly in optimally composed (i.e., near zero magnetostriction) permalloy, is required, as the permalloy films with the optimal composition ensure the largest permeability for achieving a high domain wall velocity.

Electrochemical deposition and atomic layer deposition can be used to create cylindrical nanotubes; however, both techniques limit in the type of the material that can be deposited and compromise on surface roughness.[23] Due to small dimensions, nanotubes possess relatively simple domain patterns induced due to the modified exchange interaction and shape of the tubular geometry. Conversely, self-assembly rolling technology based on strain engineering produces open cylindrical tubes restricted to diameters in the micron range but promises high surface quality through established physical vapor deposition processes and is applicable to practically all magnetic materials. Due to the large diameter and thus small curvature the exchange-driven modifications in these tubes are not significant. However, the domain pattern of soft ferromagnetic rolled tubes is influenced by the strain (if the material possesses non-zero magnetostriction and the film is positioned away from the neutral plane) and magnetostatic interaction between the side edges of the rolled membrane. The contribution of these two factors to the resultant anisotropy has yet to be fully understood.

The characterization of mesoscale 3D curved structures presents an extra difficulty since the 3D curved surfaces hide considerable portions of their structure. X-ray tomography using X-ray magnetic circular dichroism is the only imaging technique employed to produce the 3D magnetization pattern (XMCD). Despite the need for synchrotron facilities and the intricacy of the measuring technique, quantified information on magnetic properties is still lacking. In this regard, electrical (AMR) measurements where a current passes through a sample are well suited for probing the entire 3D structure and determining the preferred magnetization direction and switching fields from a global measurement.

Second, there is a need for imaging methods based on tabletop techniques to track the DW's oscillating trajectory and amplitude with nanoscale spatial resolution. Most cutting-edge direct imaging techniques capable of resolving nanoscale spatial resolution, such as time-resolved X-ray and Lorentz imaging, necessitate sophisticated measurement processes and specialized sample preparation.

In addition to contributing to the aforementioned applications, resolving these two challenges will provide a deeper understanding of micromagnetic processes [5–7] and their relationship to extrinsic and intrinsic material properties.

1.2. OBJECTIVE AND STRUCTURE OF DISSERTATION

This dissertation aims to advance methods for characterizing microscale planar and curved ferromagnetic structures and to obtain a deeper knowledge of tubular geometry-induced modifications in the domain configuration and DW dynamics. The strain contribution to static magnetic domain orientation is separated from the magnetostatic interaction and tuned to achieve the desired induced anisotropy. Analyzing the magnetization reversal by simultaneous anisotropic magnetoresistance measurements and magnetooptical imaging allowed for the establishment of a thorough understanding of the AMR signal on curved surfaces along with quantification of azimuthal anisotropy, hence eliminating the need for optical imaging techniques. Time-averaged MFM and Kerr imaging are developed to investigate the DW oscillation's trajectory and amplitude. The modifications in DW oscillation caused by the structure's size and curvature are shown, and comprehension is gained with the use of micromagnetic simulations. The dissertation is structured into eight chapters and organized as follows.

The second chapter (scientific background and state of the art) introduces the fundamentals of magnetism and state-of-the-art characterization techniques for DW oscillations. A brief introduction to tubular geometries and the recent progress in their fabrication and characterization techniques are reported.

The third and fourth chapter provides a detailed overview of the fabrication and characterization techniques used in this dissertation.

The fifth chapter presents the first experimental studies of rolling a polymeric platform with micron-sized soft ferromagnetic structures of arbitrary shape, either rolled upwards or downwards to different rolling diameters. The use of a small structure's width along the circumferential direction allows disentangling strain contributions from magnetostatic interaction on the resulting magnetic anisotropy. Improved state-of-the-art magnetoresistance measurements together with micromagnetic simulations are used to quantify the rolling-induced azimuthal magnetic anisotropy.

The sixth chapter demonstrates a new approach for quantitatively assessing the oscillatory movement of ac-excited domain walls with nanoscale resolution utilizing widespread and easy-to-use characterization techniques (MFM and Kerr microscopy). This approach is further used to study the DW oscillation dependency on the excitation strength, frequency, structure's lateral size, and film thickness.

The seventh chapter combines the knowledge acquired from chapters 4 and 5 and presents the DW oscillation studies in curved magnetic structures. It discusses the influence of curvature/strain-induced anisotropy on the DW motion.

The eighth chapter summarizes the most relevant developments and outlines the current and future topics in view of potential applications.

Chapter 2 SCIENTIFIC BACKGROUND

This chapter discusses the fascinating static and dynamic magnetic characteristics of ferromagnetic materials. Tubular structures and the modifications associated with their curved geometries are addressed in detail. In addition, an overview of the approaches used to examine the DW oscillations and magnetization of tubular geometries is presented.

2.1. MAGNETISM AND MAGNETIC ENERGY DENSITIES

Magnetism is the observable physical phenomenon associated with the vector quantity known as the magnetic moment, which is generated by the spin and orbital motion of elementary particles. However, the net magnetic moment of an atom is primarily due to electrons and neglects the much smaller moment of the nucleus due to its greater mass. It is estimated by a vector sum of all its electronic moments. A vector sum with zero net moment per atom results in diamagnetism, whereas a vector sum with a positive net moment per atom result in para-, ferro-, antiferro-, or ferrimagnetism. In the case of an atom sitting in a lattice, the electron's orbit is subjected to crystal fields produced by the surrounding atoms or ions, in contrast to the case of an isolated atom. Thus, the atomic orbitals of electrons in a lattice are strongly coupled to the crystal fields. Due to additional, spin-orbit coupling, also the atomic magnetic moment can be coupled to the lattice. Strong coupling prevents the orbit and orbital moment of an electron from rotating freely and aligning with the field and constitutes a source of anisotropy (magnetocrystalline anisotropy). In case of weak spin-orbit coupling, however, spins are free to rotate and are consequently the only contributors to the net magnetic moment. This phenomenon is known as orbital moment quenching.[27] Because electrons in the empty shells contribute to the net magnetic moment in transition metal ions, their orbital moments are largely quenched; however in rare earth elements, they are shielded by electrons in the outer shells, therefore, their orbital moments are not quenched. The quantum-mechanical exchange forces between neighboring spins are the source of physical origin of ordered electron spins in the case of ferro-, ferri-, and antiferro-ordering (as illustrated in Figure **2.1**a). The exchange energy E_{ex} between two nearby spins, i and j, with spin angular momentum $\boldsymbol{S}_i \cdot h/2\pi$ and $\boldsymbol{S}_j \cdot h/2\pi$, respectively, is represented as follows:

$$E_{\mathrm{ex}} = -2J_{\mathrm{ex}}\boldsymbol{S}_i \cdot \boldsymbol{S}_j = -2J_{\mathrm{ex}}\boldsymbol{S}_i\boldsymbol{S}_j\cos(\theta) \tag{2.1}$$

where, J_{ex} is the exchange integral, and θ is the angle between the spins. For positive J_{ex}, E_{ex} is minimum when spins are parallel (i.e., ferromagnetic ordering). Exchange interaction between surrounding spins can also be thought of as spin-spin coupling, which is very strong and determines the orientation of neighboring spins.

According to Eq (2.1), for positive J_{ex}, all spins should be aligned in a single direction (referred to as a domain), minimizing the system's exchange energy. Such single-domain state configurations exist in nanoscale ferromagnetic structures (diameters of a few tens of nanometers) at the expense of demagnetizing energy due to the presence of surface magnetic charges in regions where magnetization is normal to the surface. When a single-domain particle size is reduced below a threshold diameter, it transforms into a superparamagnetic state.[28,29] Such particles exhibit zero coercivity due to the fact that their thermal fluctuations are sufficient to cause spontaneous demagnetization. Figure **2.1**b illustrates the particle coercivity as a function of particle size. Coercivity, measured by the width of the magnetic hysteresis, indicates how well the particle can resist an external magnetic field without getting demagnetized. Thus, zero coercivity of a superparamagnetic particle (i.e., with radius below r_{sp}) corresponds to zero net magnetization in the absence of magnetic field. In contrast, as the nanostructures surpass an upper size threshold (r_{c}), they enter a multidomain area, where the domains attempt a flux-closure arrangement, decreasing the magnetostatic energy at the cost of exchange energy at domain walls. Figure **2.1**c depicts the effect of reducing magnetostatic (stray-field) energy by forming multi-domain and eventually flux-closure states. The critical lateral dimensions for the respective domain states and coercivity regions depend on the material's magnetic properties, such as the strength of exchange interaction, intrinsic anisotropy, and saturation magnetization.

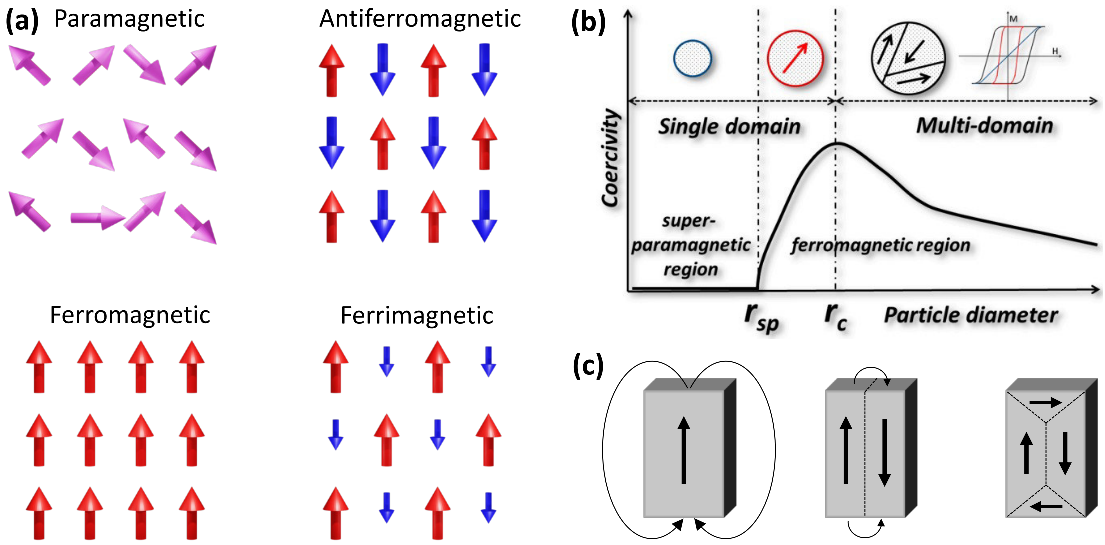

Figure 2.1: Magnetization configuration: (a) Magnetic moment orientations in paramagnets, ferromagnets, antiferromagnets, and ferrimagnets with distinct exchange coupling. **(b)** Effect of size on the magnetic characteristics, especially coercivity of a ferromagnetic material (taken from[29]). **(c)** Minimization of magnetostatic energy through domain splitting and formation of a flux-closure state (adapted from[30]).

In the ferromagnetic multi-domain region, the width of the domain wall Δw, i.e., the region where individual magnetic moments gradually reorient and separate one domain from another, is determined by the equilibrium between cost of exchange and anisotropy energy, and is expressed as $\Delta w \propto \sqrt{A/K}$. As the exchange energy with energy constant A favors the smallest angles between neighboring spins, resulting in a wide DW width. In contrast, any sort of anisotropy with anisotropic constant K prefers magnetic moments along an easy axis, as within the domains, and favors a narrow domain wall. Due to negligible magnetocrystalline anisotropy, the exchange energy and shape anisotropy determine the DW width in soft ferromagnetic thin films, such as permalloy.[31] Different types of DWs may exist according to the geometry, dimensions and properties of the material being used in patterned magnetic elements. In the absence of additional anisotropies, magnetization stays in the film plane and one observes five typical DW configurations. In permalloy nanowires/nanostripes (one-dimensional systems), transverse and vortex walls are commonly reported. In the case of the transverse wall, a V-shaped wall, i.e., a wall with asymmetric width along the width of the stripe, minimizes the exchange energy and demagnetizing energy associated with the magnetic charges inside the DW (Figure **2.2**a). On increasing the thickness/width of the stripe, the spins of the DW form flux closure spin configuration by curling around a spin pointing out of the plane, known as vortex DW (Figure **2.2**b); such a spin configuration has lower demagnetizing energy but higher exchange energy.[32]

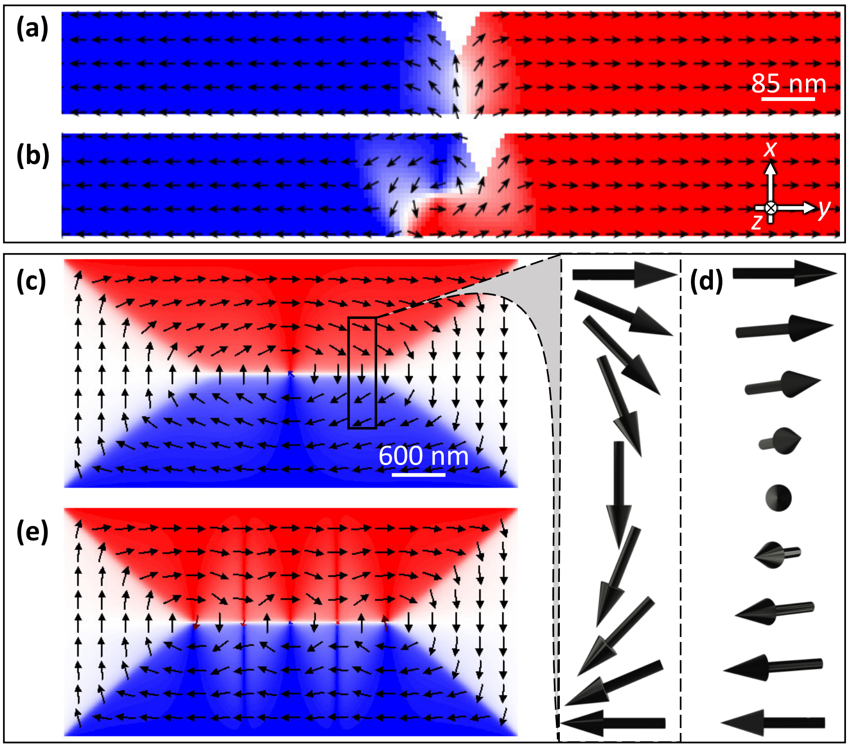

Figure 2.2: Rotation of spin vectors from one to another neighboring domain in permalloy structures. **(a)** Transverse and **(b)** vortex domain walls in nanostripes of thicknesses 5 nm and 20 nm, respectively. **(c)** Flux-closure Landau domain configuration in 20 nm thick rectangle. The magnified view shows the spin structure for the Neel type (in-plane rotation) DW present in the 180-degree domain wall. **(d)** The spin structure of the Block-type (out-of-plane rotation) DW is present in thick film having thicknesses above 90 nm. **(e)** Landau domain configuration with cross-tie walls in a 50 nm thick rectangle. Figure 2.2c is further discussed in section 4.3.

In extended thin films (two-dimensional structures), the DW can be further categorized based on the spin texture into; (i) Néel walls and (ii) Bloch walls.[31] As shown in Figure **2.2**c, the magnetization in Néel type DW rotates in the plane of magnetization and perpendicular to the plane of the DW, and is common in very thin films (up to 20 nm). In the Bloch DW (Figure **2.2**d), the rotation is out of the film plane and in the plane of the DW, and is preferred in thick films (above 90 nm). In thicknesses between 30 nm and 90 nm, energy can be gained by replacing a 180-degree Néel wall with a complicated composite wall, the cross-tie wall (Figure **2.2**e). In conclusion, magnetic texture formation is geometry and material property dependent and occurs at the equilibrium of exchange, magnetostatic, and anisotropy energy density, minimizing the system's net magnetic energy density.

Above discussed anisotropy terms can be of several origins[33]:

2.1.1. MAGNETOCRYSTALLINE ANISOTROPY

Due to the coupling of spin to the orbital motion of the electron, known as spin-orbit coupling, alignment of the spin magnetic moment is connected to the preferred orientation of electrical orbits within the electrical field of the neighboring atoms, the so-called crystal electric field. As a result, the energy required to overcome this crystal electric field energy is known as magnetocrystalline anisotropy energy. This demonstrates that the orbital motion of the electron determines the easy axis direction of magnetocrystalline anisotropy.

In the case of single crystals with one dominating symmetry axis (i.e., hexagonal or tetragonal crystals) the combination of the crystal electric field and spin-orbit coupling often leads to a uniaxial magnetic anisotropy (anisotropy constant, K_1), which can be described in the simplest form with the following anisotropy energy ansatz for the magnetization pointing at an angle θ away from the easy axis,

$$E_{\mathrm{ani}} = K_1 Sin^2\theta \tag{2.2}$$

The field applied perpendicualr to the easy axis that rotates and saturates the magnetization entirely perpendicular to the easy axis by overcoming the anisotropy is called the anisotropy field,

$$H_{\mathrm{ani}} = 2K_1/\mu_0 M_s \tag{2.3}$$

In a polycrystalline film, randomly oriented single crystals in the form of film grains are expected to exhibit magnetocrystalline anisotropy and contribute to the coercivity and local spin textures.

2.1.2. DEMAGNETIZING ENERGY

When a ferromagnetic body is put in a homogeneous magnetic field strength $\mathbf{H}_0$, the field $\mathbf{H}$ inside the ferromagnet that magnetizes the body is different in magnitude from the applied field and varies with direction in a complex manner.

The difference between the applied ($\mathbf{H}_0$) and magnetizing field ($\mathbf{H}$) is the demagnetizing field ($\mathbf{H}_\mathrm{d}$), and is connected to the magnetization $\mathbf{M}$ inside the magnet via:

$$\mathbf{H}_\mathrm{d} = -N\mathbf{M} \tag{2.4}$$

where N is a geometry-dependent constant called demagnetizing factors, and ratios of the axes determine it. The minus sign in Eq (2.4) indicates that the demagnetizing field points opposite to the magnetization vector. The sum of demagnetizing factors along three orthogonal directions for a trivial shape is a constant,

$$N_x + N_y + N_z = 1 \tag{2.5}$$

The origin of $\mathbf{H}_\mathrm{d}$ can be understood using the following Maxwell equation, for the magnetic flux density,

$$\mathbf{B} = \mu_0(\mathbf{H} + \mathbf{M}) \tag{2.6}$$

Maxwell's equation, div $\mathbf{B} = 0$, yields:

$$\mathrm{div}\,\mathbf{H} = -\mathrm{div}\,\mathbf{M} \tag{2.7}$$

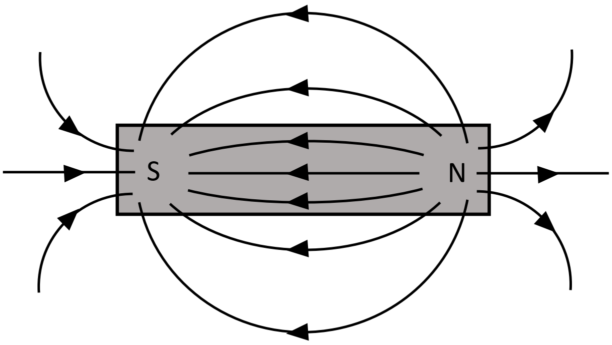

Figure 2.3: Demagnetizing field ($\mathbf{H}_\mathrm{d}$) of the bar magnet.(Adapted from[33]).

That means that any divergence of $\mathbf{M}$ generates a magnetic field. In the absence of an external field ($\mathbf{H} = \mathbf{H}_\mathrm{d}$), the generated field is called the demagnetizing field (Figure **2.3**a). Thus,

$$\operatorname{div}\mathbf{H}_\mathrm{d} = -\operatorname{div}\mathbf{M} \qquad (2.8)$$

Hence, the magnetic field **H** in Eq (2.6) is the net magnetic field existing from other sources as well as the demagnetizing field. Outside the magnetic body, the demagnetizing field is also known as stray fields. As the name implies, the field within the magnetic body acts to demagnetize it and hence is antiparallel to the magnetization that creates them, as expressed already in Eq (2.4).

The demagnetizing field energy is connected with the field generated by the magnetic body, i.e., the demagnetizing field. It can be expressed as,

$$\begin{aligned} E_\mathrm{ms} &= ({}^{1}/_{2})\mu_0 N M^2 \\ &= ({}^{1}/_{2})\mu_0 N M_s^2 \boldsymbol{m}^2 \\ &= K_\mathrm{d} N \boldsymbol{m}^2 \end{aligned} \qquad (2.10)$$

where $\boldsymbol{m}$ is the normalized magnetic moment, and $K_\mathrm{d} = ({}^{1}/_{2})\mu_0 M_s^2$ (in J/m^3) measures the maximum demagnetizing energy density connected to a ferromagnetic material.

2.1.3. PHYSICAL ORIGIN OF SHAPE ANISOTROPY

When there is no magnetocrystalline anisotropy present in a polycrystalline sample, the field required to saturate the magnetization in either direction is the same if the sample were spherical. However, with non-spherical shapes, it is easier to magnetize the structure along the long axis than along the short axis. This asymmetry occurs because the demagnetizing factors along the short axis are larger in magnitude than those along the long axis. As a result, in order to produce the same magnetizing field (**H**) inside the magnetic body, the applied field along the long axis can be smaller than the one along the short axis.

The magnitude of magnetostatic energy for an ellipsoid with a semi-major axis z and two equal length semi-minor axes along x and y with a magnetization vector making an angle θ from the axis z is,

$$E_\mathrm{ms} = ({}^{1}/_{2})\mu_0 N_z M_s^2 \boldsymbol{m}^2 + ({}^{1}/_{2})\mu_0 (N_x - N_z) M_s^2 \boldsymbol{m}^2 Sin^2\theta \qquad (2.11)$$

The angle-dependent term in Eq (2.11) favors the magnetization to point along the long axis of the ellipsoid and is termed shape anisotropy. Thus, the shape anisotropy constant K_s for a fully magnetized sample is,

$$K_s = (1/2)\mu_0(N_x - N_z)M_s^2 \tag{2.12}$$

2.1.4. MAGNETOSTRICTION

Magnetostriction is a magnetic material characteristic, primarily generated by spin-orbit coupling, that alters the shape or dimensions of the material during the magnetization processes. Figure **2.4** illustrates the role of strong spin-orbit coupling in the mechanism of magnetostriction. Below the Curie temperature T_c, spontaneous magnetization rotates the spins, and electron cloud in the direction determined by the anisotropy of the crystal. This causes the nuclei, for example, to move apart, resulting in magnetostriction, $\Delta L'/L'$. The application of a strong vertical field rotates the spins and electron cloud by 90 degrees, allowing the nuclei to approach each other and producing a strain of $\Delta L/L$.

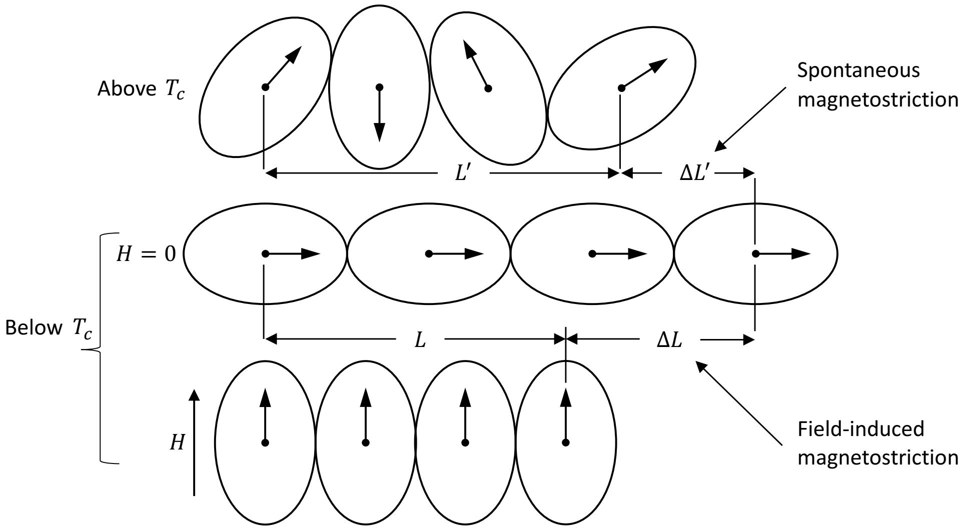

Figure 2.4*:* Schematic view of the mechanism of magnetostriction: A lattice of atoms (net electron spin of an atom using an arrow at the center and an elliptical electron cloud). (Adapted from[33]).

Figure **2.4** illustrates enormous strains as a result of extremely strong spin-orbit coupling and complete rotation of the electron cloud on a rotating spin orientation. In reality, however, magnetostrictive strains are on the order of 10^{-5}, suggesting electron cloud reorientation occurs to a much lower degree because orbital moments are almost completely quenched in transition metal alloys.

2.1.5. MAGNETOELASTIC EFFECT

Mechanical stress applied to magnetostrictive materials – alters the preferred orientation of magnetization and therefore acts as a source for tailoring domain orientation or inducing magnetic anisotropy as shown in Figure **2.5**. The magnitude and direction of induced magnetic anisotropy depend on the magnitude and sign of both, magnetostriction of the material (λ) and stress applied to the material (σ). This effect is called inverse magnetostriction or magnetoelastic effect. The induced anisotropy can substantially affect low-field magnetic properties such as permeability (a measure of magnetization that a material obtains in the presence of a magnetic field), remanence, and coercivity. For isotropic magnetostrictive material, magnetoelastic energy amounts as follows,

$$E_{\mathrm{me}} = K_{\mathrm{u}}\, Sin^2\theta \tag{2.13}$$

$K_{\mathrm{u}} = ({}^{3}/_{2})\sigma\lambda$ is the magnetoelastic energy constant, and θ is the angle between the applied stress and saturation magnetization direction. Applied stress can be written in terms of strain in magnetic material, $\sigma = \varepsilon Y$, where ε is elastic strain, and Y is the Youngs modulus of the material. Figure **2.5**a and b illustrate the reorientation of magnetic domains in a square-shaped magnetic element with positive magnetostriction when subjected to tensile and compressive stresses, respectively.

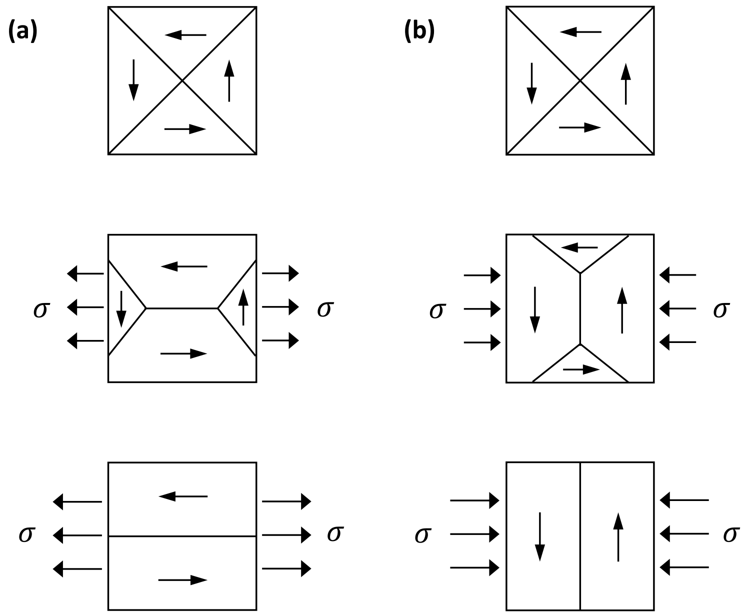

Figure 2.5: Schematic view of in-plane domain configuration of a magnetic element with positive magnetostriction under (a) tensile and **(b)** compressive stress.((a), (b) Adapted from[33]).

2.1.6. PERMEABILITY

Magnetic permeability, $\mu = \mathbf{B}/\mathbf{H}$, is the measure of magnetization that a material obtains due to both magnetization rotation and domain wall displacement in response to an applied magnetic field.[34] The initial permeability due to rotation magnetization, i.e., with applied field perpendicular to an easy axis, is expressed as,

$$\mu_{\mathrm{rot}} = {M_s^2}/{3K_{\mathrm{u}}\mu_0} \tag{2.14}$$

where, K_{u} denotes the uniaxial anisotropy present, and can have for example the above-mentioned different origins: magnetocrystalline anisotropy, magnetostrictive anisotropy, or magnetostatic, i.e., shape anisotropy. The magnetization rotation contributes a small portion and provides the lower limit for the actual initial permeability. Large permeabilities (of the order of 10000, for permalloy) reported by Bozorth[35] can be more or less explained by reversible domain wall displacement mechanism. Bozorth interpreted the high permeability realized at 79 % Ni-Fe (Figure **2.6**a) to be due to the combined effect of a low crystal anisotropy (zero at 76 % Ni-Fe) and a low magnetostriction (zero at 81 % Ni-Fe, Figure **2.6**b) around this composition.

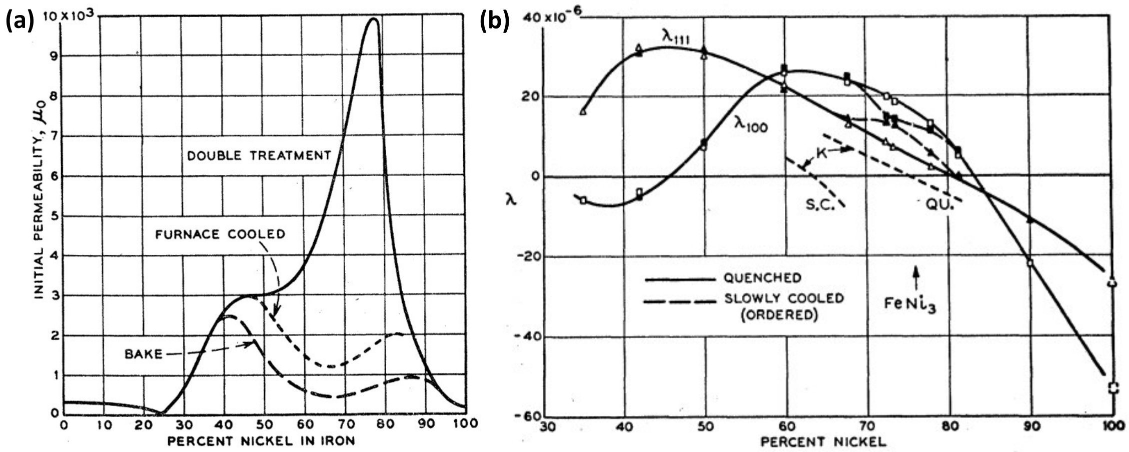

Figure 2.6: Magnetic properties of permalloy: (a) Initial permeability and **(b)** Magnetostriction of NiFe alloy at different compositions. ((a), (b) Taken from[35])

2.2. MAGNETIZATION DYNAMICS

2.2.1. LANDAU-LIFSHITZ-GILBERT EQUATION

A single magnetic moment **M** placed in a magnetic field **H** precesses around the field axis at a rate proportional to the field torque according to the Eq (2.15), due to the association of magnetic moment with angular moment,

$$\partial \mathbf{M}/\partial t = -\gamma \mathbf{M} \times \mathbf{H} \tag{2.15}$$

where γ is the gyromagnetic ratio. When modifying Eq (2.15) to explain the dynamics of the magnetization M within a ferromagnet, H is considered to be an effective field, i.e. the sum of external magnetic field, demagnetizing field, anisotropy fields and other field equivalent energy terms. In addition, a damping component must be added to describe the magnetization relaxation along the effective field axis. It gives,

$$\partial \mathbf{M}/\partial t = -\gamma \mathbf{M} \times \mathbf{H} + (\alpha/M_s)\mathbf{M} \times (\partial \mathbf{M}/\partial t) \tag{2.16}$$

where α is the Gilbert damping constant and is small in most magnetic material (for example, $\alpha \approx 0.05$ in permalloy). Eq (2.16) is known as the Landau-Lifshitz-Gilbert (LLG) equation and is a variant of originally proposed Landau-Lifshitz equation,

$$\partial \mathbf{M}/\partial t = -\gamma \mathbf{M} \times \mathbf{H} + (\alpha\gamma/M_s)\mathbf{M} \times (\mathbf{M} \times \mathbf{H}) \tag{2.17}$$

Thus, the magnetization can be approximated phenomenologically as a physical vector in a viscous medium.

2.2.2. DOMAIN WALL DYNAMICS IN PLANAR STRUCTURES

The experimental results of very high domain wall velocity in soft ferromagnetic nanowires with a width of hundreds of nm revealed three distinct regions with respect to velocity as a function of the external field (Figure **2.7**a).[36–38] For low magnetic fields, the DW velocity increases linearly with the field strength until a critical field (known as Walker field) is reached. In the linear regime, the first term of the LLG Eq (2.16) governs the motion of DW. Considering one-dimensional wall approximation (Figure **2.7**b),[20] a field $\mathbf{H}$ along the x-axis applies a torque that tilts the domain wall moments out of the plane by an angle ψ, creating a demagnetizing field $\mathbf{H}_\mathrm{d}$. The demagnetizing torque, $\gamma_0\mathbf{M} \times \mathbf{H}_\mathrm{d}$, tilts the moments toward the external field, driving the domain wall forward. The velocity v of the domain wall thus depends on the demagnetizing field $\mathbf{H}_\mathrm{d}$ and only indirectly on the applied field $\mathbf{H}$. The demagnetizing field has a finite limit, and reaches a maximum value at $\psi = \frac{\pi}{4}$, therefore the torque due to the demagnetizing field and thus also the velocity v peaks. Here, DW velocity is given by a linear relation $v_1 = \mu_\mathrm{m}\mathbf{H}$, where μ_m represents the mobility of the DW. If the torque on the moments due to applied field $\mathbf{H}$ drives ψ more than $\frac{\pi}{4}$, (i.e., above walker field, denoted with H_w in the inset of Figure **2.7**a) the wall plane becomes unstable. It starts precessing, causing the demagnetizing torque and instantaneous velocity to change direction with each quarter-period, with a time average approaching zero: this scenario is known as Walker breakdown[39]. On further increasing field $\mathbf{H}$, ψ rotation becomes faster, leading to a small net damping torque $\alpha\mathbf{M} \times \frac{\partial\mathbf{M}(t)}{\partial t}$ that tilts the domain wall moments toward the applied field, driving forward motion. Thus, at a high field, the damping torque provides the dominant net contribution to the velocity.

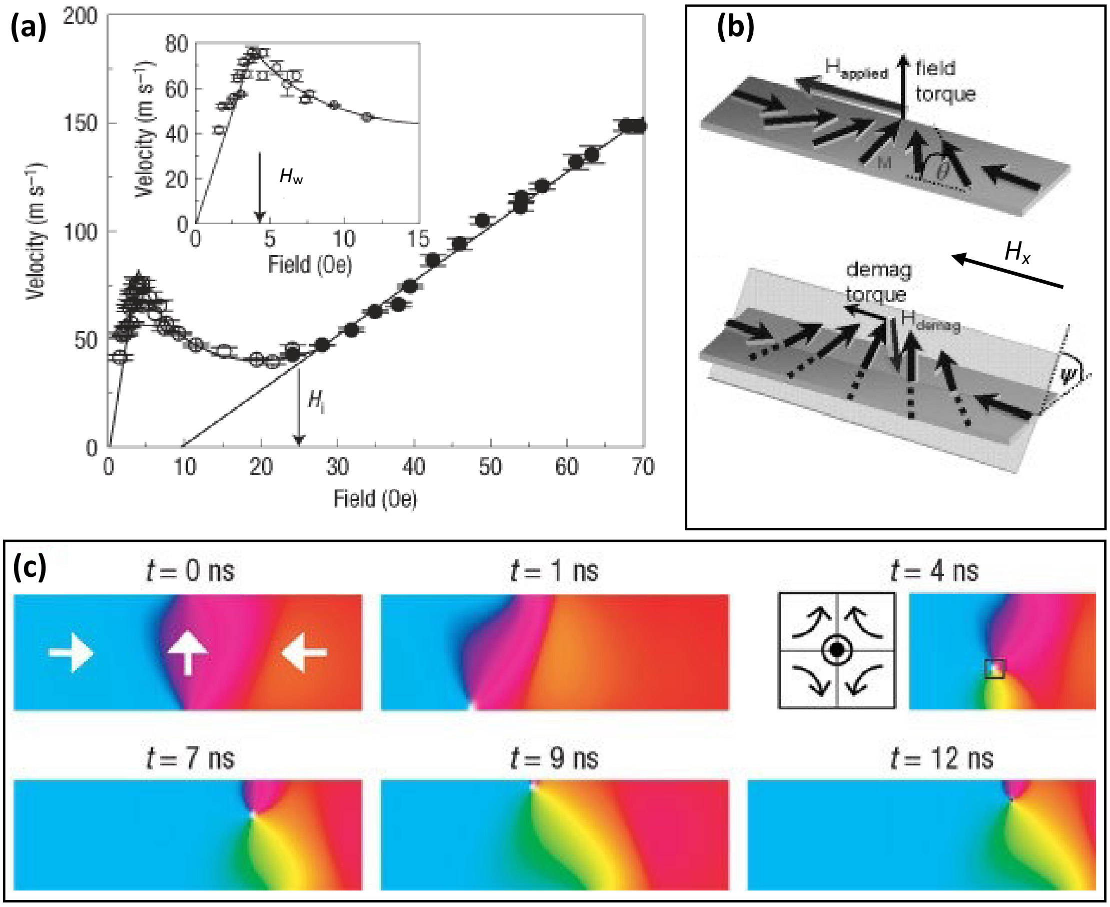

Figure 2.7: DW dynamics in magnetic nanowires: **(a)** Walker breakdown is shown by the experimental results of field-driven domain wall dynamics on a nanostripe (adapted from[36]). Inset depicts low-field region of figure **2.7**a. **(b)** Schematic illustration of a 1D domain wall spins and the torque responsible for its motion (taken from[20]). **(c)** Micromagnetic simulation of DW dynamics in a permalloy nanowire, time-resolved images of antivortex nucleation from the nanowire side, its motion and annihilation at different times of the moving DW at 20 Oe, the field above walker breakdown (taken from[37]).

In contrast to the one-dimensional model, the Walker breakdown in a planar nanostripe with transverse DW is caused by antivortex nucleation on the stripe's edge, as shown in Figure **2.7**c.[37] Nucleation of an antivortex slows down the DW propagation as it absorbs most of the torque provided by the effective field. The nucleated antivortex travels along the stripe width towards the other edge, where it disappears while the DW moves along the stripe. Once the antivortex disappears, DW returns to the similar spin configuration as previously, with the reversed transverse moment. Nucleation and disappearance of the antivortex make the DW velocity fluctuate, resulting in lower average velocity.

2.2.3. TECHNIQUES TO INVESTIGATE DOMAIN WALL OSCILLATIONS

Investigating the dynamics of a magnetic domain wall and a vortex in the presence of high frequency (>MHz) ac-excitations was accomplished by using time-resolved imaging employing various microscopies.[40–47] One such measurement using ultrafast Lorentz microscopy (Figure **2.8**a) was used to track the trajectory of a continuous (Figure **2.8**b) and damped (Figure **2.8**c) vortex oscillations of frequency 101.5 MHz in a 2.1×2.1 μm^2 large and 26 nm thick polycrystalline permalloy square.[44] The magnetic vortex configuration consisted of four domains creating a flux closure state with in-plane magnetization oriented along the structure's edges and a perpendicularly magnetized center with a diameter of around 10 nm. The vortex oscillations were imaged utilizing a fixed and growing time gap between synchronized, high-quality electron pulses and the RF excitation. This research utilized electron pulses with a repetition rate of 500 kHz, generated by a Ti:sapphire laser with a central wavelength of 400 nm and a pulse duration of 2.2 picoseconds. The temporal resolution of such imaging was determined by the electrical synchronization quality and duration of the electron pulses. It offered a high spatial resolution of 2 nm.

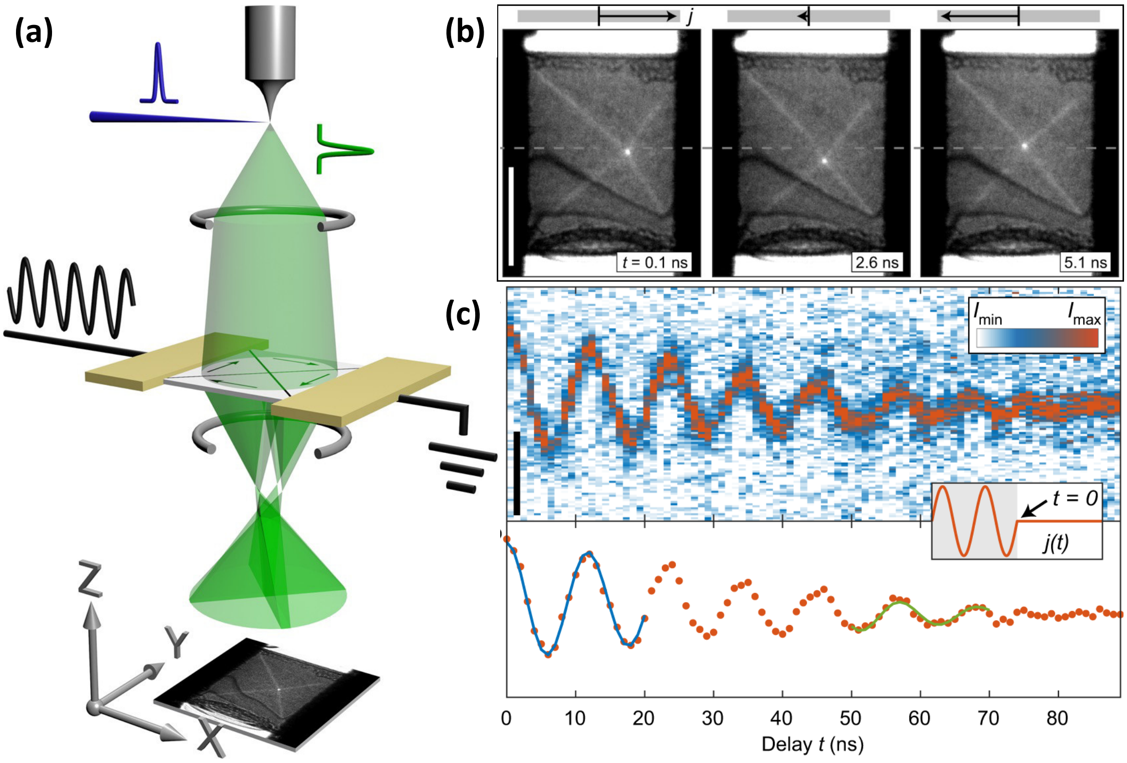

Figure 2.8: Ultrafast Lorentz imaging of vortex dynamics: (a) Schematic of time-resolved Lorentz microscopy with synchronized radio frequency (RF) sample excitation. Time-resolved imaging of **(b)** vortex dynamics with continuous excitation at a frequency of 101.5 MHz and a current density of 1.7×10^{11} A.m^2 (scale bar = 1 µm) and **(c)** vortex movements after switching off the excitation (f_{ex} = 101.5 MHz, $j = 2.9 \times 10^{11}$ A.m^{-2}). ((a)-(c) Taken from[44] under the terms of CC BY license).

Similarly, time-resolved observations utilizing X-ray-based magnetic imaging were used to investigate the ac-current excited domain wall and vortex dynamics with nanoscale spatial resolution.[40,43] However, applying time-resolved imaging with the aforementioned two microscopies is a challenging task. In addition, these microscopies rely on X-ray or electron-beam transparent substrates, requiring special sample preparation. In contrast, time-resolved imaging using Kerr microscopy[45–47] is relatively simpler and requires no special sample preparation but is limited by its moderate resolution in the sub-micrometer range. Kerr microscopy can be used to gain useful information on ac-excited periodic or quasi-periodic domain wall oscillations by regular difference-image processing[47,48] as well, which is robust, simple, and quick to operate. Such difference image technique was used to study the frequency dependence of domain wall oscillations in nanocrystalline ribbon ($Fe_{73}Cu_1Nb_3Si_{16}B_7$, thickness 20 µm) as demonstrated in Figure **2.9**. The static domain state (Figure **2.9**a) was subtracted as a background and the oscillating domain walls were recorded with long exposure periods at different frequencies (Figures **2.9**b and c). The black and white contrast in Figures **2.9**b and c provide information on the amplitude of wall motion, which decreases with increasing frequency.

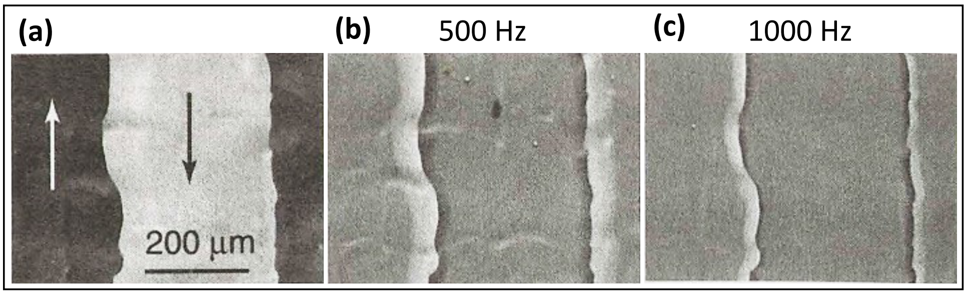

Figure 2.9: Imaging of periodic wall oscillation processes in a nanocrystalline ribbon ($Fe_{73}Cu_1Nb_3Si_{16}B_7$, thickness, 20 µm): The domain state **(a)** is subtracted from images captured with a sinusoidal field of 500 Hz **(b),** and 1000 Hz **(c),** and fixed amplitude applied along the domain direction. ((a)-(c) Taken from[48]).

In addition to methods employing direct imaging, indirect methods such as measurements of the ac-susceptibility[49–51] and ac-permeability[52–55] (an averaged property of the sample) also allows studying ac-field driven domain wall dynamics using the MOKE susceptometry and magnetoimpedance measurements, respectively. In the MOKE susceptometer measurements[50] (Figure **2.10**), the dynamic Kerr signal is proportional to the susceptibility [$V_{\mathrm{Kerr}} = (X+iY) \sim \chi H$] and therefore contains all spectral signatures of domain wall processes. To analyze the oscillatory domain wall dynamics in cobalt wires (Figure **2.10**a), real (X), and imaginary (Y), Kerr signals were recorded at a constant magnetic field amplitude, H, and at varying frequency from high (10 kHz) to low (1 kHz) and plotted as a Cole-Cole plot in Figure **2.10**b. On reducing the driving frequency, the slide motion of domain walls, and consequently the imaginary Kerr signal (Y), increases. As soon as the wall moves approximately half the domain width away from its zero-field equilibrium point, the domains coalesce and the magnetization of the wire saturates. A further decrease in the driving frequency leads to full magnetic switching, indicated by vertical to a quarter-circle segment in Cole-Cole plot, Figure **2.10**b. Apart from qualitative understanding of ac-field driven magnetization processes, recorded Kerr signal allows for quantitative analysis and extract the depinning field for slide motion and domain wall mobility. However, the accuracy of this method depends on the regularity of the stripe pattern and the average distance between the domain walls, making it well-suited to detecting the global properties of large structure sizes (of several hundreds of microns).

When it comes to resolving nanoscale domain features, magnetic force microscopy (MFM)[57] has been proven to be a very powerful technique, but is largely unexplored concerning imaging of time-dependent domain processes. Few reports include early measurements of write head fields in the MHz regime[58–60] and the more recent development of side-band MFM[61]. In both cases, MFM is used for successfully mapping temporal field dynamics but not for imaging oscillatory DW dynamics in space.

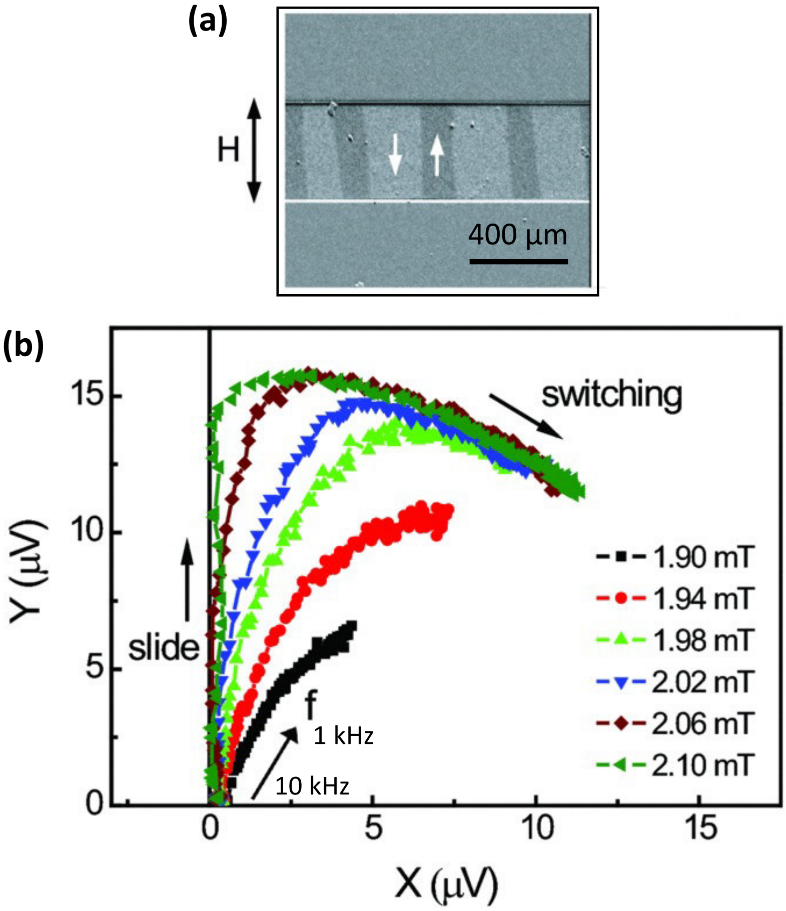

Figure 2.10: Magneto-optical Kerr effect susceptometry measurements: **(a)** Kerr image of demagnetized domain configuration of cobalt wire with thickness 40 nm. **(b)** Cole-Cole plot constructed using the real and imaginary Kerr signals at constant field amplitudes. (The arrow denotes the frequency direction (high to low). ((a), (b) Taken from[56]).

2.3. CURVATURE-INDUCED MAGNETISM

Numerous analytical and experimental investigations have examined the effect of curvature on static and dynamic magnetic characteristics.[62–67] These studies have demonstrated intriguing magnetochiral effects driven by curvature and topologically stable magnetization patterns, also confirmed by micromagnetic simulation. On the basis of a micromagnetic framework of curvilinear magnetism, curvilinear geometry-induced effects on magnetism are described. It accounts for both local and nonlocal (magnetostatic) magnetic interactions and describes the energy of a uniaxial ferromagnet as follows:

$$E = E_{\mathrm{nonlocal}} + E_{\mathrm{local}} \tag{2.18}$$

Local interactions include anisotropy, exchange and intrinsic Dzyaloshinskii–Moriya interaction (DMI). Thus,

$$E_{\mathrm{local}} = E_{\mathrm{ani}} + E_{\mathrm{ex}} + E_{\mathrm{DMI}} \tag{2.19}$$

Because of the geometry broken local spatial symmetry, reconstructing exchange energy expression in the local curvilinear basis $\boldsymbol{e}_{\alpha}$, E_{ex} written in cartesian coordinates as $E_{\mathrm{ex}} = (\nabla m_i)^2$, splits up into three contributions:[68]

$$E_{\mathrm{ex}} = E_{\mathrm{ex}}^{0} + E_{\mathrm{ex}}^{\mathrm{A}} + E_{\mathrm{ex}}^{\mathrm{D}} \tag{2.20}$$

E_{ex}^{0} represents the expression of the isotropic exchange, similar to the form of the Heisenberg exchange, Eq (2.1). Curvature also results in two additional magnetic interactions: geometry-governed exchanged-driven anisotropy and the DMI (extrinsic to crystal structure DMI and can be manipulated by the object geometry). In addition, the transformation of a nonlocal energy component in a curvilinear frame and the derivation of an expression for magnetostatic interaction in a curved geometry offer additional energy terms arising from geometric curvature that are lacking in flat films.

Thus the, the curvature-driven local and nonlocal interactions are the source of curvature driven magnetism when the curvature radius is comparable to intrinsic length scales such as magnetic exchange length, domain wall width, or magnon wavelength.[69] Experimental evidence of curvature-induced DMI has been reported rarely.[70] The emergence of such a vector exchange interaction in curved magnetic surfaces has several implications for theoretical and experimental studies and potential applications in magnetic logic[71] and storage devices[19]. For instance, it gives a possible explanation of the theoretically predicted magnetochiral effects[72,73] in cylindrical geometries. Furthermore, it offers a new perspective to fabricate magnetic shift registers[74] and spintronics devices[75] with a 3D non-planar shape and an enlarged domain wall velocity[21].

2.3.1. CYLINDRICAL NANOTUBES

Magnetic cylindrical nanotubes possess peculiar 3D surfaces with structural uniaxial symmetry in addition to the absence of the core, unlike magnetic rods or cylindrical wires.[65] The advantage of nanotubes over cylindrical nanowires is that the absence of the magnetic material around the symmetry axis eliminates magnetic singularities (or Bloch points) associated with vortex state and vortex-like DW. Theoretical calculations based solely on the interplay between dipole and exchange energies, neglecting any magnetocrystalline anisotropy, give a magnetic phase diagram for ferromagnetic hollow cylinders, as shown in Figure **2.11**a.[76,77] Experimental nanotubes of different sizes reported by different groups support the theoretical predictions.[78–80] Depending on the size of the nanotube, the axial state is formed by lowering the exchange energy, whereas the vortex (flux-closure) state is formed by lowering the magnetostatic energy. The mixed state minimizes both by possessing axial magnetization at the center and the vortex state at the end of the tube. As reported studies show, thin (small diameter/large curvature) and long tubes exhibit uniform magnetization pointing along the tube axis. The mixed state has the lower energy for slightly larger R, and the global vortex state prevails for even larger *R*. Salinas[81] reported the influence of varying exchange (J_{ex}) and dipolar interaction (D) energies, defined as $\gamma = {}^{D}/_{J_{\mathrm{ex}}}$, while keeping the geometry dimensions (radius, length) fixed (Figure **2.11**b). The order parameter used to obtain the phase diagram is vorticity (a measure of circularity of the moments around the tube), ρ^{z}.

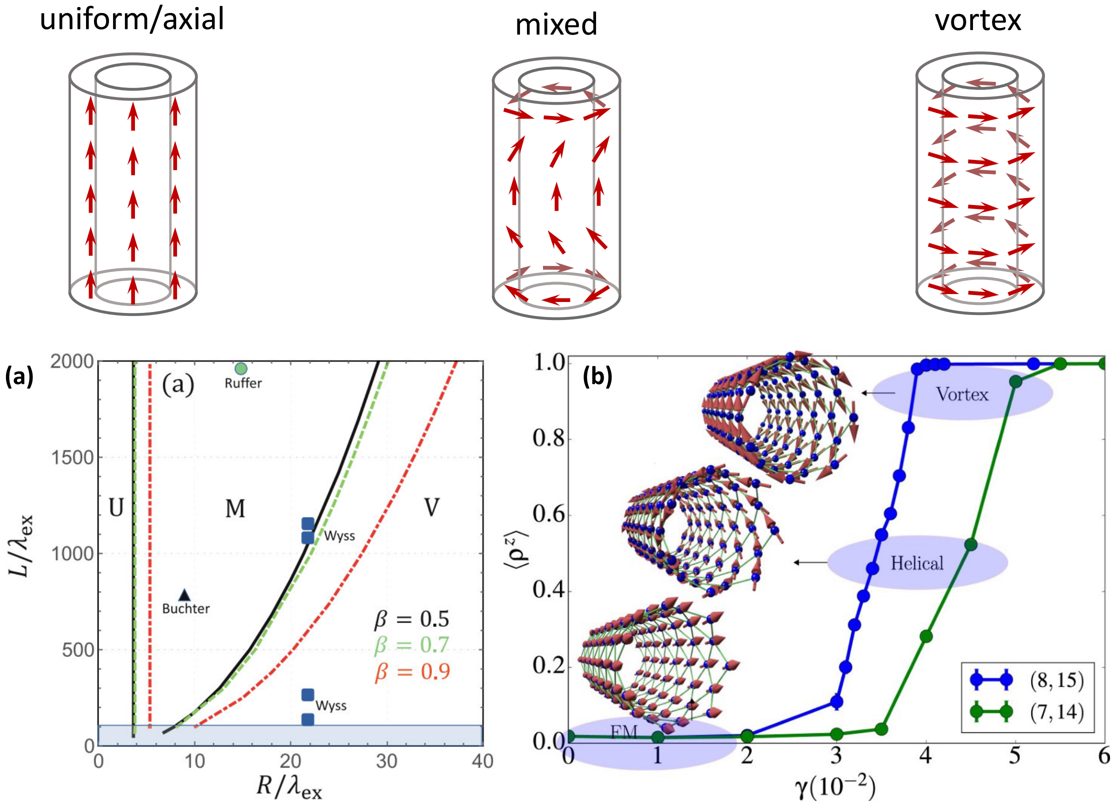

Figure 2.11: Phase diagrams for magnetic nanotubes: **(a)** Based on the tube size (x- and y-axis represent, radius and length of the tube normalized by exchange length l_x). (Taken from[82]) **(b)** Based on the strength of exchange and dipolar interaction for a particular tube dimension (taken from[81] under the terms of CC BY license). Magnetization configuration sketches are adapted from[83].

In addition to static magnetic properties, the dynamics of DWs in magnetic nanotubes exhibit peculiar curvature-induced effects.[21,73,84] The DW configurations in nanotubes differ slightly compared to the flat stripes as they adapt to the tubular geometry (Figure **2.12**a). Thus, like two possible orientations of transverse DW in flat nanostrips, DW in nanotubes display two vorticities, which are energetically degenerate but exhibit different dynamic properties due to the influence of curvature on the DW configuration. Due to the tubular geometry, spins in the DW region possess a non-zero radial component (Figures **2.12**b and c) to reduce the magnetostatic volume charges. The combination of the DW vorticity and the field direction is used to define the chirality of the system and reduce the four possible combinations of vorticity and field vector to two chirality: left-handed (LH) and right-handed (RH).[84] The external magnetic field pointing along the axis of the tube applies torque in the radial direction on the DW spins. Depending on the vorticity, the applied field either increases or decreases the existing radial component of the LH (red line) and RH (blue line) case, respectively (Figure **2.12**d). This special feature of the DW structure, leads to the break in left and right symmetry of the DW propagation and as a result chirality dependent velocity and stability of the DWs (Figures **2.12**e and f). In nanotubes, the walker breakdown, i.e., the collapsing DW structure above a critical DW speed, can be completely suppressed for a specific DW chirality (as shown in Figure **2.12**f for right-handed chirality), beneficial for memory devices and logic gates based on fast and controlled DW motion. In the case of another chirality, the left-handed one in the Figure **2.12**f for field of 8 mT, above a critical velocity, a vortex–antivortex nucleation takes place and travels to the opposite direction of the nanotube. This process is similar as in flat stripe (Figure **2.7**c), but in the case of a nanotube, the nucleation of the single vortex (antivortex) is prohibited due to the lack of lateral edges. A pair of vortex and antivortex annihilate when they meet on the opposite side of the tube, thereby transforming the DW's chirality from left-handed to right-handed with increased velocity. The right-handed chirality DW can achieve a velocity higher than the minimum phase velocity of the spin waves; therefore, the DW emits spin waves. This effect is called the spin-Cherenkov effect.[21] In conclusion, eliminating the lateral boundaries in nanotubes has significant consequences on the stability and velocity of the DW[85,86].

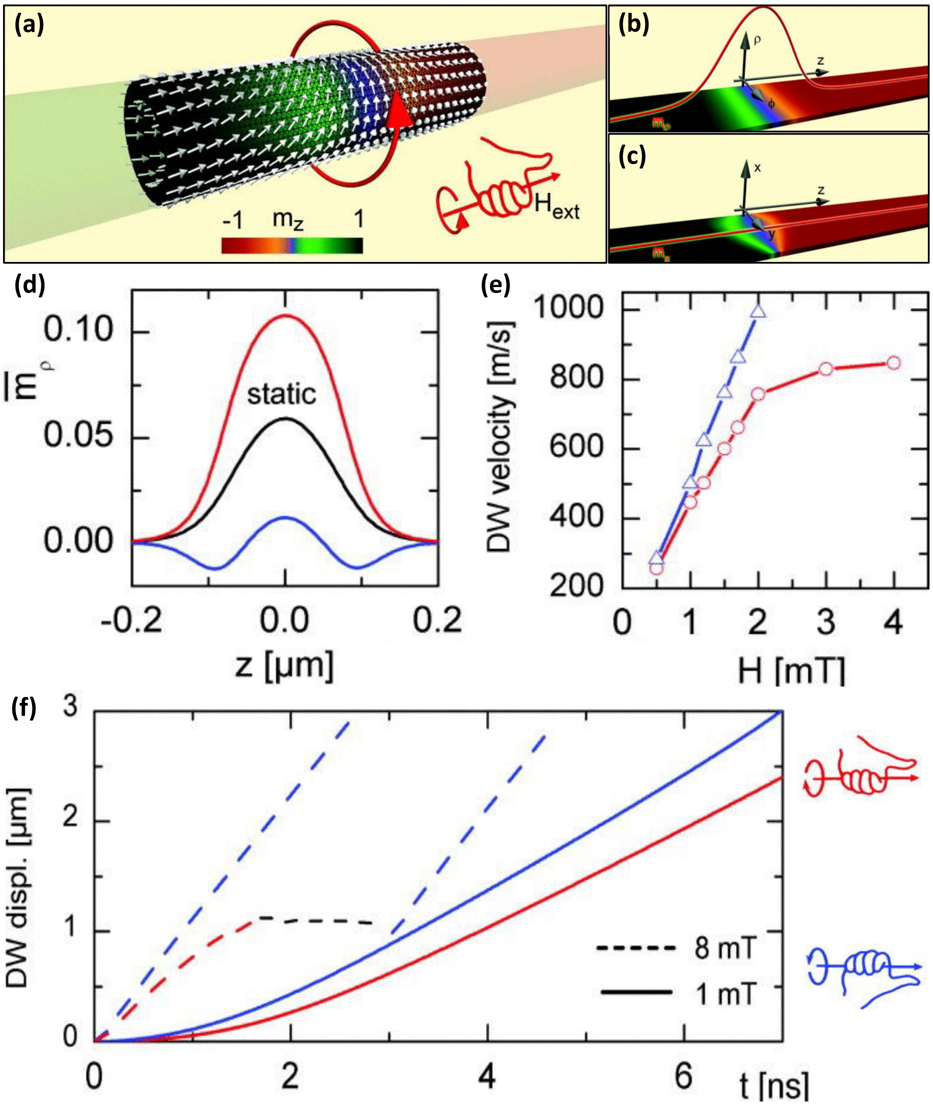

Figure 2.12: DW dynamics in nanotube: (a) Simulated magnetic configuration of a head-to-head vortex-like DW in a nanotube with LH chirality (visible when the field direction and DW vorticity are combined). **(b)** The unrolled tube with similar domain wand domain wall configuration as in the rolled state. **(c)** To compare, a transverse domain wall in a flat stripe. The red line shows the radial component of the moments averaged over each cross-section. Comparison between the static and moving DW with both chirality, LH (red) and the RH (blue) **(d)** the average radial component (DW moving at 1mT field) along the tube-axis, **(e)** DW velocity in the low-field region and the definition of its chirality by combining field vector and vorticity. **(f)** DW displacement (driven by two different fields) as a function of time. ((a)-(f) Taken from[84]).

Effects of chiral symmetry breaking have also been predicted[73,87] and more recently observed in magnonics[88] (Figure **2.13**a and b). Spin-wave (SW) magnetic excitations that hold the potential to play a crucial role in achieving low-power consumption and fast operative rates in information processing - acquire a peculiar asymmetric dispersion (regarding the sign of the wave vector, as shown in Figure **2.13**b) in magnetic nanotubes with azimuthal magnetic domains (Figure **2.13**a). Because the rotating magnetization and the propagation direction define a handedness, this phenomenon implies a chiral symmetry breaking. The origin of this symmetry breaking in the nanotube is the non-local dipole-dipole interaction induced purely due to curvature. In conventional thin films, such an effect is seen only in the presence of an intrinsic DMI. Thus, the origin of both the chiral DW motion and the asymmetry in the spin-wave propagation in nanotubes is the 'dipole-induced Dzyalonshiinsky-Moria-like' effect. Experimental realizations of fast DW dynamics and spin-wave propagation in cylindrical (circular cross-section) tubular geometries are yet to be achieved.

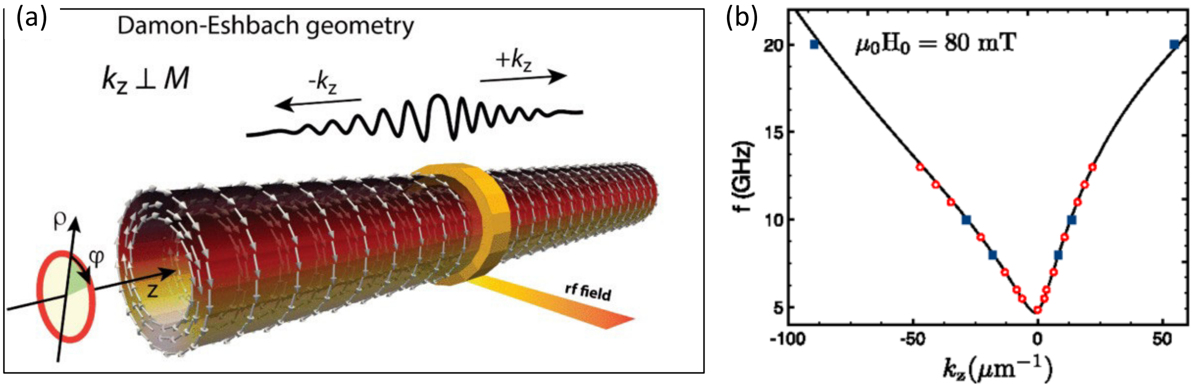

Figure 2.13: Spin waves in nanotube: (a) Schematic representation of a nanotube (outer radius = 30 nm, wall thickness = 10 nm, and length = 4 µm) in azimuthal domain state. Spin waves are excited by a radial RF field in the middle and move towards the tube end perpendicular to the magnetization. **(b)** Spin wave dispersion relation for nanotubes for circular fields of 80 mT obtained by analytical calculation (solid line) and by micromagnetic simulations (red and blue dots). ((a), (b) Taken from[73]).

2.3.2. CYLINDRICAL MICROTUBULAR ARCHITECTURES

Experimental tubular geometries prepared from rolling an initially planar membrane possess diameters in the range of tens of micrometers and form a multi-winding open tube, unlike a closed cylinder.[89,90] The resulting magnetic domain configuration in such tubes obtained using Fe-rich permalloy and nickel thin film membranes, revealed axial (Figure **2.14**a), helical (Figure **2.14**b) and azimuthal (Figure **2.14**c) domain state and is understood from the competition between the strain-induced anisotropy, magnetostatic interaction, and the shape of the film before rolling. Because of the small curvature, the curvature- and shape-driven exchange interactions that are controlled by the curvature gradient were no longer significant.

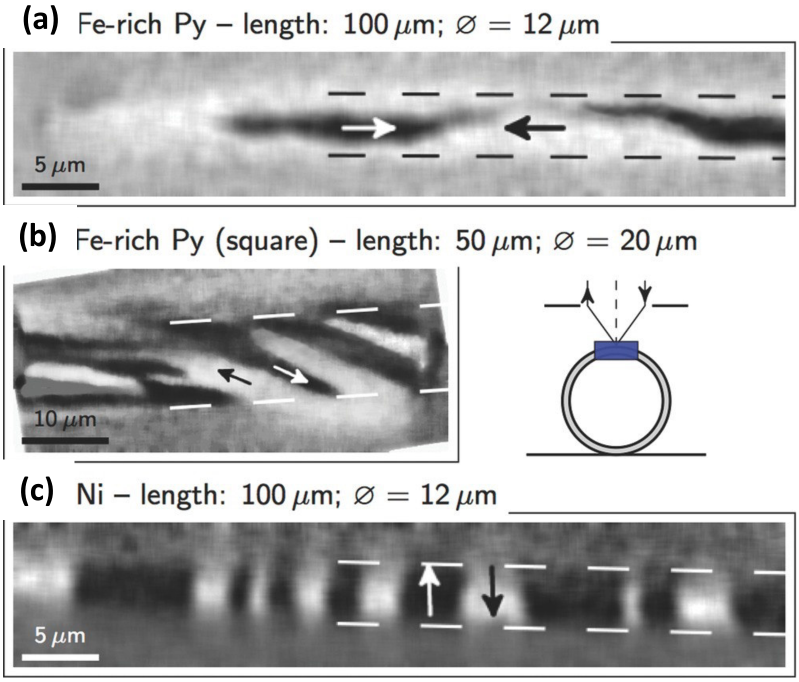
(a) Fe-rich Py – length: 100 μm; ∅ = 12 μm
5 μm
(b) Fe-rich Py (square) – length: 50 μm; ∅ = 20 μm
10 μm
(c) Ni – length: 100 μm; ∅ = 12 μm
5 μm

Figure 2.14: Magnetic domain configuration of micro-tubes: (a) Axial state. **(b)** Helical state. **(c)** Azimuthal state. ((a)-(c) Taken from[89]).

The influence of tubular geometry on the high-frequency ac-current-induced dynamic magnetization processes was seen in the form of an increased giant magneto-impedance (GMI) by almost two orders of magnitudes (Figure **2.15**c).[1] The increase in GMI was attributed to the higher stability of azimuthal domains (Figure **2.15**b) in 100 nm thin rolled-up $Ni_{81}Fe_{19}$ membranes (compared to their planar counterparts, Figure **2.15**a). A flux-closure configuration was produced by the geometrical transformation of the initially planar membranes, and it was understood from the combination of magnetoelastic anisotropy originating from non-zero negative magnetostriction of the film and compressive strain, and modified magnetostatic interaction between the membrane edges.

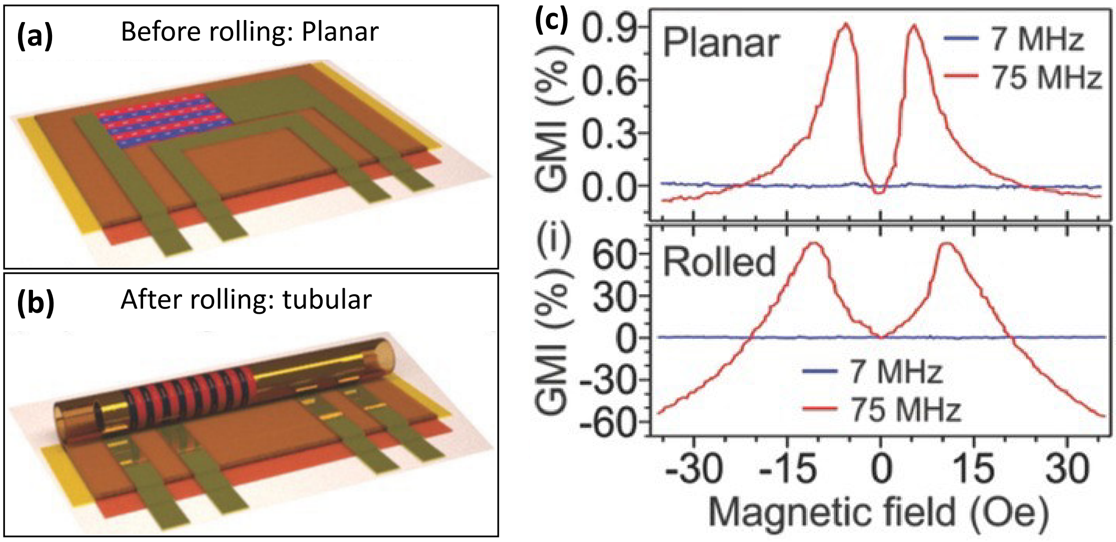

Figure 2.15: Giant magnetoimpedance in tubular structures: Schematics illustration of GMI device **(a)** before and **(b)** after rolling. **(c)** GMI response with magnetic field measured at 7 MHz and 75 MHz of planar and self-assembled structure. (Taken from[1])

2.3.3. FABRICATION OF CYLINDRICAL TUBULAR GEOMETRIES

The preparation of magnetic nano- and micro-tubular architectures of a high surface quality with acceptable surface roughness is of particular interest for exploring the magnetic textures and physical phenomena predicted by micromagnetic simulations and analytical calculations. The conventional deposition techniques to fabricate the nanotubes require non-magnetic templates to grow on, such as a porous alumina template for the electrodeposition process [91,92] and a round solid cylindrical template for atomic layer deposition[79,80] (Figures **2.16**a–d). However, these chemistry-based techniques are restricted in the type of material that can be deposited and compromise with surface roughness. The most appropriate way to synthesize nanotubes of high surface quality is still an ongoing investigation.

In contrast, micron-sized tubes can be prepared by a combination of physical vapor deposition and self-assembled rolling. Realized systems are based on strained mono[89,93] (Figures **2.16**g–i) or bilayer[94–97] (Figures **2.16**e and f) metallic thin films, e.g., by hetero-epitaxy, which self-assembled into a tubular “Swiss-roll” architecture with a diameter of few microns, once the layers were released from the substrate. With the functional layer being part of the strain architecture, one is, however, restricted in the choice of magnetic film thickness and size. It is not possible to homogeneously strain patterned micron-sized magnetic elements.

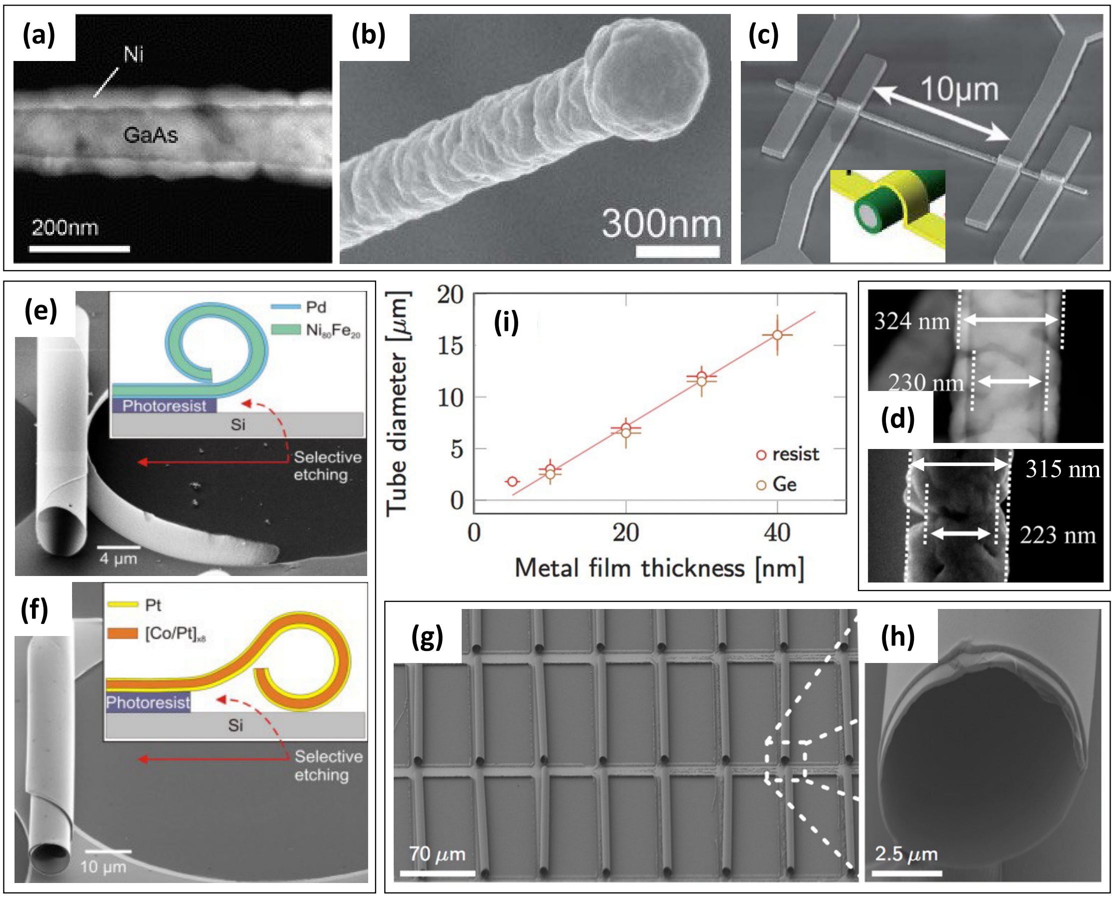
(a)
Ni
GaAs
200nm
(b)
300nm
(c)
10µm
(e)
Pd
$Ni_{80}Fe_{20}$
Photoresist
Si
Selective etching
4 µm
(f)
Pt
$[Co/Pt]_{x8}$
Photoresist
Si
Selective etching
10 µm
(i)
Tube diameter [µm]
20
15
10
5
0
0
20
40
Metal film thickness [nm]
resist
Ge
(d)
324 nm
230 nm
315 nm
223 nm
(g)
70 µm
(h)
2.5 µm

Figure 2.16: Fabrication of nano- and micro-tubes: (a) HAADF STEM image and **(b)** and **(c)** SEM image of Ni nanotube deposited on GaAs core using atomic layer deposition (taken from[79]). **(d)** TEM (top) and SEM (bottom) images of a single Ni nanotube showing inner and outer diameter (taken from[80]). SEM images (and sketch in the inset) of **(e)** Roll-up and **(f)** roll-down ferromagnetic microtubes (taken from[97]). **(g)** Fabrication of rolled-up single-layer ferromagnetic nanomembranes with negligible spacing between windings (see the magnified view in **(h)**) **(i)** The diameter of the rolled-up nanomembrane is determined by the film thickness (taken from[89]).

A remedy to that is using a polymeric platform – a versatile technology pioneered by D. Karnaushenko and D. D. Karnaushenko at the Institute for Integrative Nanosciences at the Leibniz IFW Dresden.[98] Here, a structured polymer layer architecture consists of a sacrificial layer (SL), hydrogel (HG) as a swellable layer, and a stiff polyimide (PI) layer. After selective removal of the SL, the HG/PI bilayer self-assembles into a multi-winding tube, the so-called 'Swiss-roll' architecture and provides the curved and strained template for an arbitrary magnetic structure on top of it (Figure **2.17**a). Key achievements of this material system are the robustness of the SL, the excellent adhesion between the HG and PI, a high yield during patterning and self-assembly, and the compatibility with standard, high-throughput, and high-resolution manufacturing techniques, including photopatterning of the polymer layers. The deterministic roll-up process results in tubes with diameters ranging from 30 µm to 1 mm (Figure **2.17**b). The layer thicknesses and the pH of the rolling solution determine the final tube diameter. This platform enables parallel fabrication on a wafer scale (Figure **2.17**c). It has led to the development of a diverse array of electronic devices (Figures **2.17**c – f), which profit from the geometry transformation in different ways. Rolled-up structures with many windings have a drastically reduced footprint compared to their planar equivalents, which improves the energy storage density of batteries and capacitors.[99,100] Magnetic encoders (Figures. **2.17**c and d)[101], helical micro-antennas (Figures **2.17**e and f)[98], and transformers were realized through the reshaping and reorienting capability of the shapeable polymer stack.

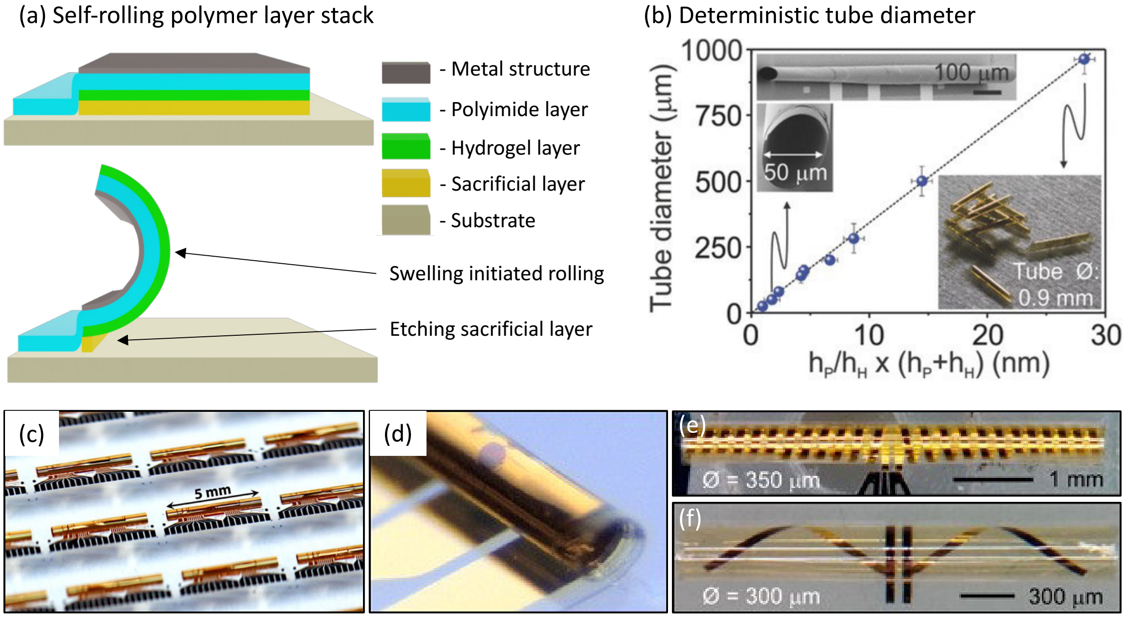
(a) Self-rolling polymer layer stack
- Metal structure
- Polyimide layer
- Hydrogel layer
- Sacrificial layer
- Substrate
Swelling initiated rolling
Etching sacrificial layer
(b) Deterministic tube diameter
Tube diameter (µm)
1000
750
500
250
0
0
10
20
30
h_P/h_H x (h_P+h_H) (nm)
100 µm
50 µm
Tube Ø: 0.9 mm
(c)
5 mm
(d)
(e)
Ø = 350 µm
1 mm
(f)
Ø = 300 µm
300 µm

Figure 2.17: Self-rolled micro-tubes based on the shapeable polymer stack: (a) The PI/HG bi-layer self-rolls when the SL is removed. **(b)** Rolled-up polymer tubes have a deterministic diameter defined by the layer thicknesses (taken from[102]). **(c)** An array of giant magnetoresistance angular encoders. **(d)** A rolled-up polymer tube with electrodes and a spin valve magnetic sensor ((c), (d) taken from[101] under the terms of license CC BY-NC). **(e), (f)** Helical antennas with different diameters ((e), (f) taken from[98] under the terms of CC BY license).

2.3.4. CHARACTERIZATION OF TUBULAR GEOMETRIES

One of the central challenges in studying the static and dynamic magnetic properties of 3D tubular geometries is obtaining a direct image of the 3D arrangement of magnetization texture. To investigate the magnetic domain configuration of curved surfaces having large diameters (tens of micrometers), wide-field Kerr microscopy[103,104] has been used extensively for ferromagnetic microwires[82,105] and rolled-up microtubes[1,89,90].(Figures **2.18**a – c) It is a non-invasive technique that allows observing domain configuration and magnetization reversal processes. Observing the domains in the planar state and following their change upon rolling allows for a deeper understanding of the origins of the rolling-induced domain patterns and tuning the system. The disadvantage of using Kerr microscopy is that the accessible area of a wire or rolled-up tube is limited to only a narrow region along the length of the tube axis for which the reflected light reaches the objective lens.

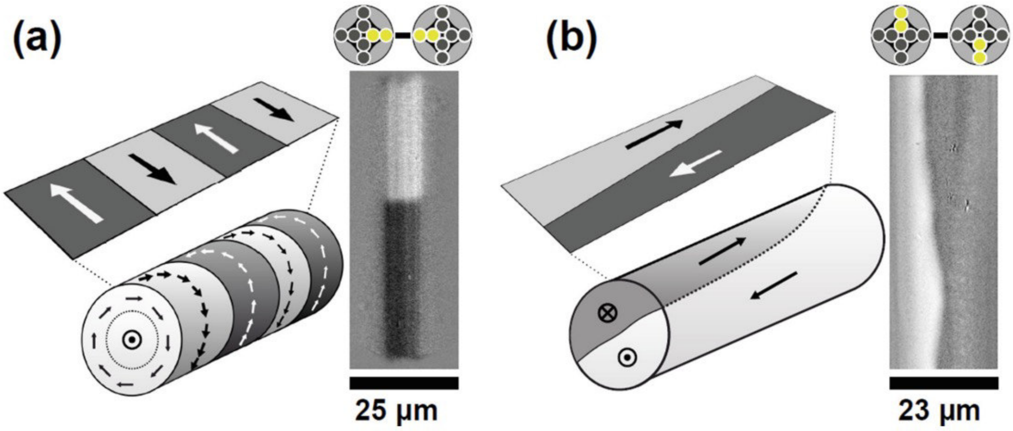

Figure 2.18: Kerr imaging of 3D structures: **(a)** Azimuthal domains on a $Co_{71}Fe_5B_{11}Si_{10}Cr_3$ wire and **(b)** axial domains on a $Fe_{74}B_{13}Si_{10}C_2$ wire imaged in longitudinal Kerr sensitivity. ((a), (b) Taken from[82]).

Imaging nanotubes with Kerr microscopy can become difficult due to the large curvature of the tube as well as due to the need for higher resolution. Therefore, a clever way to increase the spatial resolution is using X-rays for imaging[62,66,106,107] instead of visible light. Owing to the shorter wavelength, in the range of sub-nanometer depending on the

X-ray energies (soft/hard X-rays), magneto-optical imaging with X-ray can provide access to the nanoscale or even to the atomic scale of the material.

Magnetic imaging with polarized X-rays was started in the 1990s utilizing X-ray magnetic circular dichroism (XMCD) effects as a magnetic contrast mechanism to study ferromagnetic, ferrimagnetic materials, respectively. Its resolution over the years has been improved by two orders of magnitude from 1 μm to 10 nm. To characterize 3D magnetic geometries, there are two primary imaging methods based on X-ray microscopy, X-ray photoemission electron microscopy (X-PEEM), detecting secondary electrons that can escape the surface of a specimen, and magnetic full-field transmission X-ray microscopy (MTXM), which can directly detect the X-rays that have transmitted the sample.

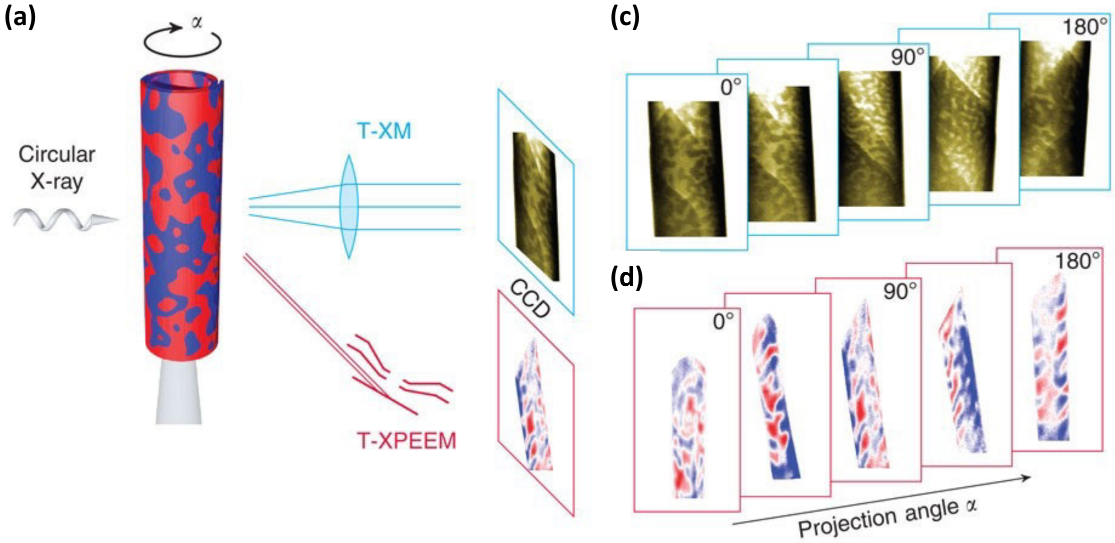

Figure 2.19: Schematics of magnetic nanotomography with MTXM and X-PEEM. (Taken from[108] under terms of CC BY license).

In multi-walled tubes made of rolled-up nano-sheets, Shadow-XMCD-PEEM was used to identify the domain pattern and to track the magnetization reversal in each winding as a function of the applied magnetic field.[109] First attempts to reconstruct three-dimensional vector fields with the help of 3D-Shadow-XMCD-PEEM by measuring projections at various azimuthal angles have already been made (Figure **2.19**).[108] For this purpose, a hollow microtube was attached at almost normal to the substrate surface using nanomanipulation. This tomographic geometry allows projections to be measured at all angles by Shadow-XMCD-PEEM. This aligns with recent efforts to model and quantitatively analyze the shadow X-PEEM contrast by micromagnetic simulations. Like, shadow-XMCD-PEEM, MTXM also allows recording an angular series and reconstructing the 3D vector field.

Magnetotransport measurements are an indirect but easier and versatile method of accessing the magnetic states[110], applicable for all dimensions of structures but limited to qualitative studies.[79,111–114] Electrical measurement, together with micromagnetic simulations, provide an idea of the global magnetization state of any geometry.

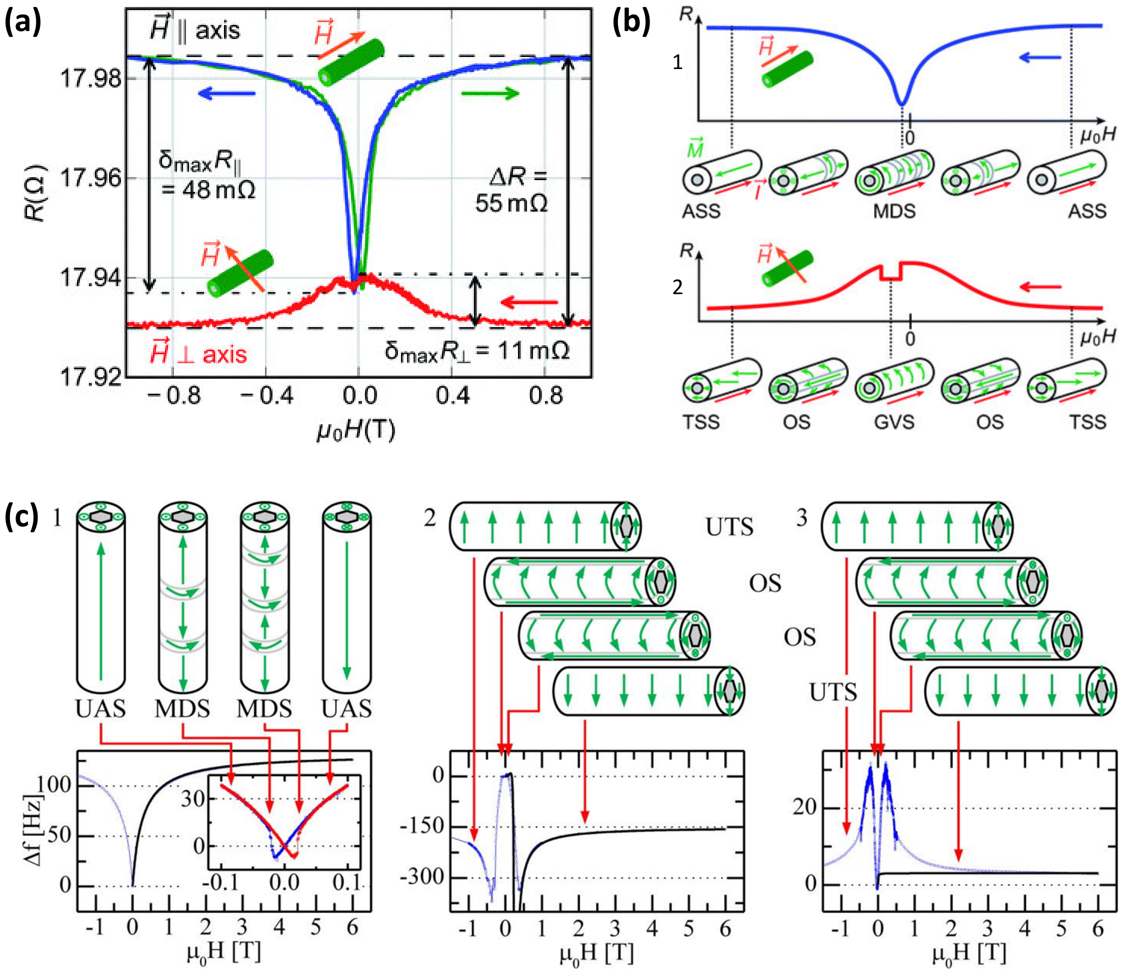

Figure 2.20: Global characterization of nanotubes: (a) Anisotropic Magnetoresistance (AMR) of a Ni nanotube for field *H* sweeping parallel to the long axis (upper curves) and perpendicular to the long axis. **(b)** Different magnetic domain states are linked to characteristic resistance values in a parallel and perpendicular field. ((a), (b) Taken from[79]). **(c)** Cantilever magnetometry revealed stable and metastable magnetic states in nanotubes ($\varnothing_{in} \approx 200$ nm, $\varnothing_{out} \approx 300$ nm). The three curves plot the response along three orthogonal axes. Red arrows refer to the fields corresponding to the specified magnetic state. (Taken from[80]).

Figure **2.20**a and b show experimental and simulated AMR measurements, respectively, performed on a single Ni nanotube for field pointing along and perpendicular to the tube axis. Experimental measurements supported by micromagnetic simulations indicate the azimuthal anisotropy in the nanotube. Another indirect method is cantilever magnetometry.[114] It is applicable to nanoscale geometries only but can estimate the anisotropy magnitude in the nanotube.[78,80] Figure **2.20**c shows the frequency shift as a function of external magnetic fields applied along the three major orientations of a nickel nanotube. The magnetic states are identified by correlating the simulated frequency shift of the most likely states with the experimental data, which provides means to study the magnetization reversal process. However, the indirect access to the magnetization offers only a rough classification without particular insight into the spatial distribution and is thus limited to simple magnetic states.

State-of-the-art techniques relying on integral measurement techniques, such as magnetometry work well for nanotube geometries in characterizing qualitative and quantitative magnetic properties, however it fails for microscale structures. Electrical measurements can work independent of the dimension of the structure but have only been performed for qualitative understanding. With the direct imaging techniques, the analysis of 2D projections of magnetization patterns recorded with X-ray microscopy may serve to investigate the domain pattern but do not provide magnitude of induced anisotropies. In contrast, Kerr microscopy that is capable of imaging the domain pattern and characterizing the anisotropy by magnetic hysteresis measurement is only applicable to structures atop the dome.

As a result, further development of electrical (AMR) measurements that are both universally applicable and reasonably easy is necessary for quantitative analysis.

Chapter 3 FABRICATION METHODS

This chapter provides an in-depth overview of the methods employed and of the magnetic structures prepared as part of this dissertation. Magnetic planar structures are deposited directly onto a silicon substrate, or a polymeric platform prepared on a glass substrate. By self-assembly rolling the polymeric platform upwards or downwards, deposited structures are transformed into curved magnetic structures.

3.1. FABRICATION OF PLANAR STRUCTURES

Throughout this dissertation, additive and subtractive manufacturing techniques were utilized to fabricate self-assembling ferromagnetic structures. This section briefly introduces the techniques of coating and patterning resist or polymeric film and depositing metallic layers. Device fabrication was performed at the Institute for Integrative Nanosciences (Leibniz IFW Dresden).

3.1.1. DEPOSITION TECHNIQUES

Polymeric layers were deposited using the spin-coating technique, whereas magnetic and gold contact layers were deposited through dc magnetron sputtering.

Spin-coating is a method of preparing a thin, homogeneous polymer film onto a flat substrate using a rotating disc. Typically, the polymer material is applied to the substrate's center when it is at rest. The substrate is then rotated at a speed of up to 8,000 revolutions per minute so that centrifugal force evenly distributes the viscous material across the whole substrate.

Sputter deposition is a versatile technique for depositing thin layers of diverse materials by bombarding the material to be deposited with energetic ions and directing the ejected atoms onto a substrate, where they form a thin layer. Using a pressure control system, the overall pressure of an inert sputter gas is typically controlled in the microbar range. A gas plasma is triggered by applying a high voltage between the cathode, which is situated behind the target, and the anode, which is electrically grounded to the chamber. Negatively charged electrons are accelerated away from the cathode by high negative cathode voltage. Acceleration of electrons induces collisions with neighboring atoms of sputtering gas, knocking electrons off the sputtering gas atoms, which results in ionization and thus the production of a plasma. Positively charged gas atoms (ions) are propelled toward the target and strike it, ejecting atoms from the target's surface. Atoms with enough kinetic energy are ejected and move through the recipient environment to the substrate's surface, where they are incorporated into the growing film.

In the case of magnetron sputtering, a large magnet is employed to trap electrons in the plasma near the target, allowing for higher plasma density and faster deposition rates. Different types of depositing materials necessitate a distinct power delivery. DC power is a cost-effective and efficient option for the deposition of conductive materials. DC magnetrons can be constructed with magnets specifically selected for creating plasma within a strong magnetic field for magnetic materials such as Fe, Ni, or Co. In contrast, insulating target materials require RF fields.

3.1.2. LITHOGRAPHY PROCESSES

Photolithography is a commonl y utilized top-down technology in the scientific and industrial sectors for the fabrication of micron-scale devices. It is a patterning technique that exploits photochemical interactions between light and photosensitive materials. The solubility of a photoresist or photosensitive polymer can be altered by selectively exposing it to the light of appropriate wavelengths and intensities. This photochemical procedure allows the photoresist to be selectively dissolved, resulting in functional structures or masking layers. Figure **3.1** depicts a typical fabrication workflow, which includes the following steps:

The first step is to spin-coat a light-sensitive layer (AZ5214E) termed photoresist onto a clean, moisture-free substrate or the entire film, which is commonly Si/SiO$_2$, glass, or glass with a polymeric platform on top. The photoresist-coated substrate spins at a fast pace (usually 3000 rpm) for approximately 30 seconds. In this manner, a thin (hundreds of nanometers) homogenous coating of resist is applied to the substrate, which is then baked on a hot plate (5 minutes at 90 degrees) to smooth out any defects. On the resist layer, lithography creates detailed patterns determined by the employed mask. Mask ensures that some portions of the photoresist (depending on the structures to pattern) remain protected and are thus unaffected by the exposed light, typically UV light, whereas the exposed portions of the photoresist react to the light when the substrate is exposed to the light source. Mask aligner devices such as the SÜSS MicroTec MA6 expose a complete sample at once, allowing for high-throughput, quick manufacturing. Mask-less aligners, such as the Heidelberg Instruments MLA 100, does not rely on physical masks. Instead, a digital image file is projected sequentially and piecewise onto the sample using a micro-mirror matrix. The used photoresist AZ5214E is an image reversal resist that can be processed in both positive and negative modes. In the negative mode, the unexposed portion of the resist is easily removed after development, while the exposed area stays, whereas in the positive mode, the opposite occurs. To utilize the photoresist AZ5214E in negative mode, there are two extra processing steps, after exposing the resist to a light source, image reversal baking at 120° C for 2 minutes and flood exposure for 35 seconds are required. Finally, the resist is developed for 35 seconds in MIF developer to dissolve the previously unexposed portions and then rinsed for 20 seconds in DI water. Electron-beam lithography can have a similar exposure effect but produces sharper features due to the well-collimated, highly intense (100 kV) electron beam. In this thesis, e^--beam is used to expose the electron beam sensitive positive polymethyl methacrylate (PMMA) resist. Patterning nanostructures in both lithographies (optical and e-beam) can be accomplished through the lift-off or etching of thin films.

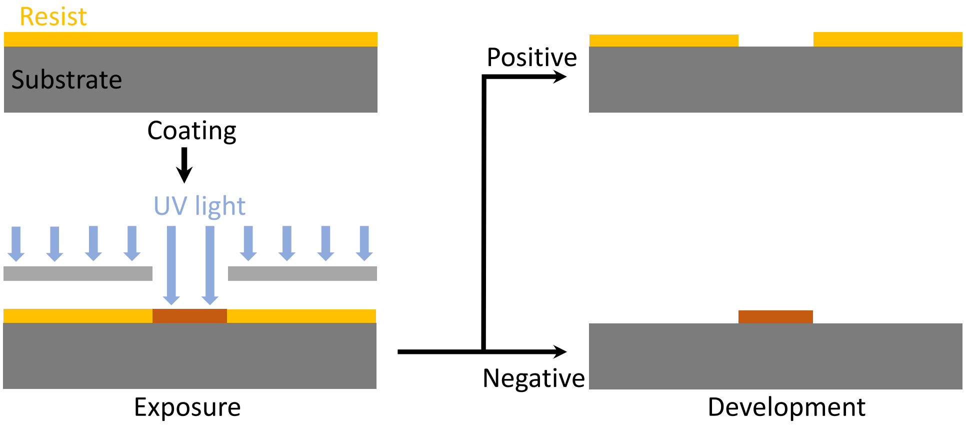

Figure 3.1: Lithography processing of microstructures: Selective exposure of a resist layer to UV light alters the solubility of the layer in a developer, either making it more soluble (positive resist) or less soluble (negative resist).

In the **lift-off technique**, first, a patterned resist structure is prepared on a smooth substrate by spin-coating and subsequent lithography. Then the target layer is deposited on top, and the resist structure is removed wet-chemically. This lifts off the target layer on top of the resist structure, while it stays on the directly deposited areas (Figure **3.2**a).

Etching is another micro-structuring process. It is a process in which uncovered portions of a metal layer are removed from the surface of a substrate by chemical reaction or physical impact. In this dissertation, the permalloy coating prepared on top of the polymeric platform is selectively removed using ion beam (a beam of inert Argon gas ions) etching. Figure **3.2**b depicts the typical workflow of the etching procedure.

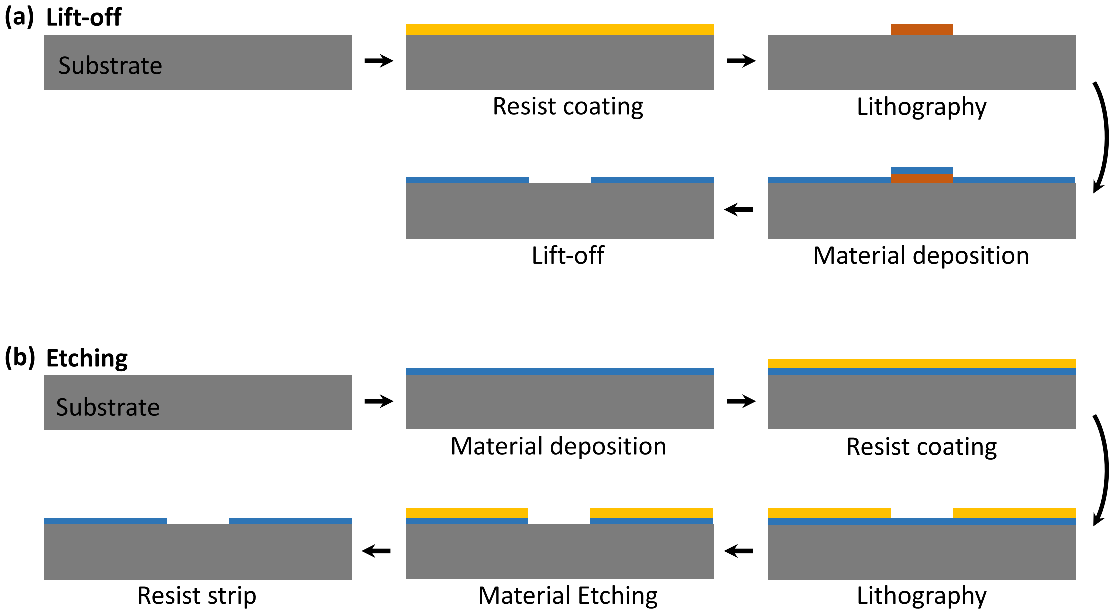
(a) Lift-off
Substrate
Resist coating
Lithography
Lift-off
Material deposition
(b) Etching
Substrate
Material deposition
Resist coating
Resist strip
Material Etching
Lithography

Figure 3.2: Micro-structuring process: (a) To design thin films using a lift-off method, an inverse photoresist pattern is prepared on the substrate, followed by the deposition of the metal layer and the lift-off of the resist material. **(b)** To pattern a layer by etching, a masking resist layer is patterned on top of the material and then removed following the etching process.

In this dissertation, optical and electron-beam lithography is employed to fabricate structures with lateral dimensions of 50 µm (and above) and 30 µm, respectively.

Moreover, permalloy structures with thicknesses of 50 nm (and above) and 20 nm are created using the lift-off and etching process, respectively. Prepared 20 nm thick permalloy rectangles of different sizes and different orientations on top of the silicon substrate and on top of the polymeric platform using the aforementioned techniques are depicted in Figures **3.3**a, b, and d, respectively.

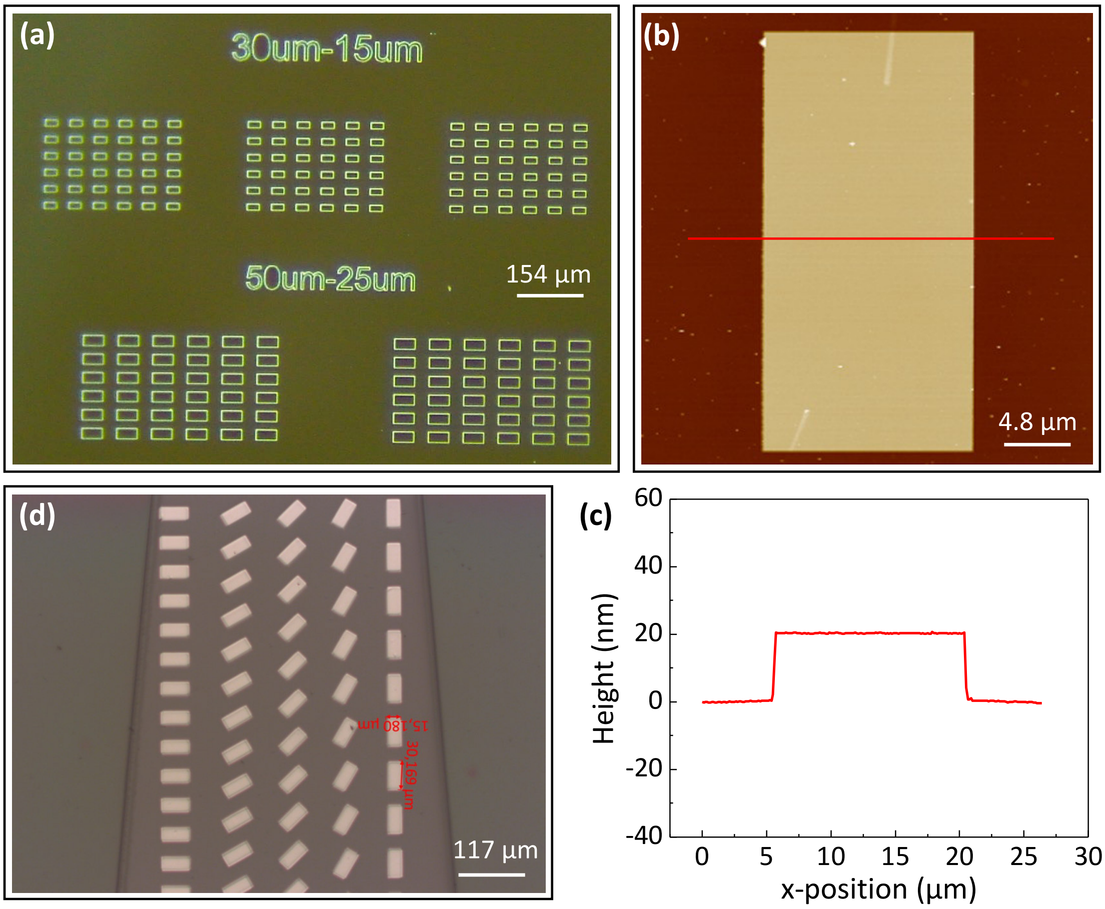

Figure 3.3: Microscale magnetic rectangles: (a) An optical and **(b)** an AFM topography image of permalloy rectangles on a silicon substrate. **(c)** The line profile of the structure in b reveals the structure's thickness. **(d)** Optical image of permalloy rectangles deposited atop a polymeric platform on a glass substrate.

3.2. PREPARATION OF CURVED SURFACES

Rolled-up technology[115,116] is a versatile approach to fabricating rolled-up 3D membranes with cylindrical geometry from a planar thin film by strain engineering. Rolling a membrane deposited by conventional thin film deposition techniques ensured the high-quality surface of the rolled membrane.[117–119] The rolling technology applied in this dissertation is based on polymeric films and was developed by Dr. Daniil Karnaushenko and Dr. Dmitriy D. Karnaushenko at the Institute of Integrative Nanosciences, Leibniz-IFW Dresden.[98,120] This technology relies on a shapable polymeric layer stack containing three polymer layers; a sacrificial layer (SL), a strained bilayer consisting of hydrogel (HG) as a swellable layer and polyimide (PI) as a stiff layer (Figures **3.4**a and c),

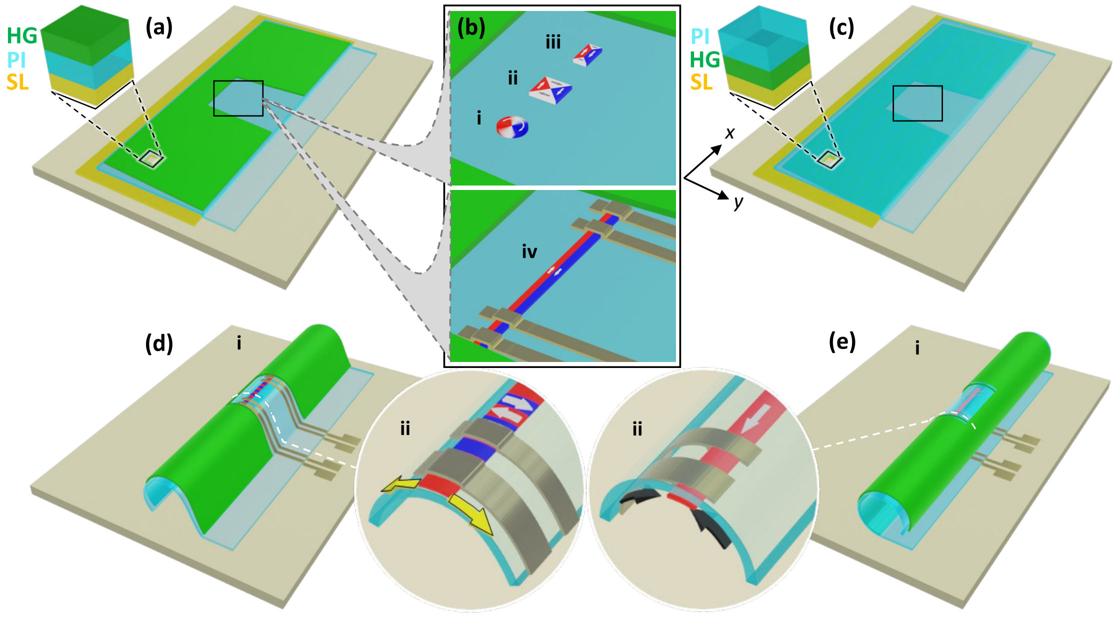

Figure 3.4: Fabrication of rolled-down and rolled-up magnetic structures with a curved shape: **(a)** Polymeric platform (PP) layer stack [sacrificial layer (SL), polyimide/stiff layer (PI), and hydrogel/swellable layer (HG)] before rolling for a rolled-down and **(c)** rolled-up fabrication. **(b)** Schematic images of magnetic domains in **i** disc, **ii** square, **iii** rectangle, and **iv** stripe in the planar state. Schematic image of the polymeric platform (with magnetic stripe and contact wires) after etching the sacrificial layer (SL) and **(d-i)** rolling down and **(e-i)** rolling up. **(d-ii, e-ii)** Magnified view of magnetic structures and polyimide layer after rolling showing the tensile and compressive strain, respectively.

which is photo-patternable, thermally stable at temperatures up to 300°C and are inert in common organic nonpolar, polar, protic, and aprotic solvents, as well as in moderate bases and acids, allowing for several steps of lithography processing. The metal-organic sacrificial layer used throughout the dissertation is prepared using acrylic acid and hydrated $LaCl_3$. It can be applied on organic or inorganic substrates. In this dissertation, the polymeric platform was fabricated on top of a glass substrate that was cleaned and silanized to prevent contamination and facilitate the polymeric layers' adhesion. UV light exposed polymeric layer parts stay, whereas unexposed parts are easily removed during development. Thus, polymeric layers act as a negative resist. After completing the fabrication of polymeric layers and metal structures on top of the platform, the bilayer (HG and PI) can be delaminated from the support and simultaneously actuated in a water-based solution of Na^+-EDTA (sodium ethylenediaminetetraacetic acid). During this process, the underlying sacrificial layer etches selectively, and simultaneously the hydrogel layer swells, actuating the stack. The stiff polyimide reinforcement constrains the lateral dimensions of the hydrogel surface during the swelling process. In the case of a polymeric platform for rolling down, the hydrogel swells from the top side in the water solution generating a differential mechanical stress that results in the bending of an entire architecture downwards as shown in Figure **3.4**d. In the case of a platform for rolling upwards, the hydrogel layer swells from the bottom and the architecture bends upwards (Figure **3.4**e). Ultimately, the initial planar polymeric platform together with the magnetic devices placed on top of it (Figures **3.5**a and b) are transformed into a compact Swiss-roll-like architecture with one or several windings (Figures **3.5**d and e). The platform allows the realization of arrays (Figure **3.5**c) consisting of mechanically active architectures that possess the self-assembly capability and therefore the template to curve and strains an arbitrary magnetic structure deposited on top of it.

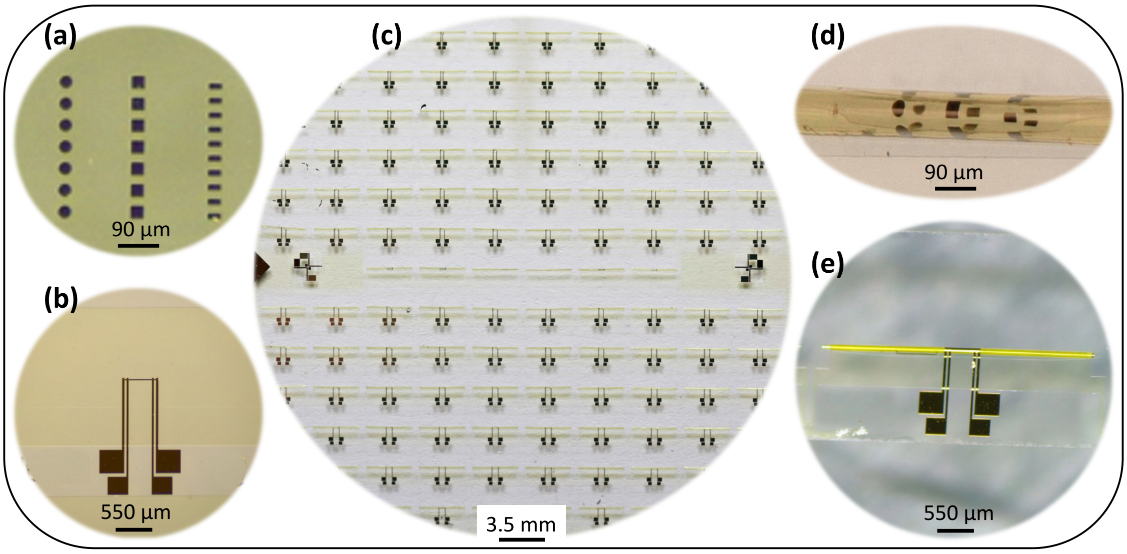

Figure 3.5: Fabrication of arrays consisting of self-assembled rolled-down structures: (a) Magnetic structures and **(b)** contacted AMR stripe, before rolling. **(c)** Array of self-assembled rolled tubular geometries consisting of structures shown in

Figures **a** and **b.** **(d)** and **(e)** shows magnified views of **c** with structures shown in **a** and **b** after rolling.

The use of two polymer stacks (SL/PI/HG and SL/HG/PI) allow the rolling of the polymer platform down- and up-wards. A rolled-down tubular geometry avoids burying the permalloy structure under the thick micron-size polymer, making Kerr microscopy measurements easier. During rolling downwards, polymeric layers might experience slight friction when touching the substrate. However, due to the sufficient stiffness and thickness (in thousands of nanometers) of PI, slight friction does not restrain the self-assembly and the polymeric platform still rolls into a tubular geometry. Different rolling directions, namely rolling downwards and upwards, create tensile and compressive strain states in magnetic elements.

3.2.1. POLYMER FABRICATION PROCESS

The stack of the three polymeric layers was spin-coated onto a 50×50 mm^2 glass substrate. Using optical lithography, arrays of the polymer stacks in rectangles with a typical size of 3.5×3.2 mm^2 were designed. Thin HG layers of usually 300 nm were patterned on top of SLs to achieve roll-up tubular geometries and on top of PIs (thickness of PIs 1000 nm, keeping HG/PI thickness ratio 1:3) to achieve roll-down tubular geometries. During the selective removal of the underlying SL in an aqueous solution containing EDTA (ethylenediaminetetraacetic acid, 7.0 – 10.0 pH) for several hours, HG absorbs water that is attracted by its polar carbolic acid groups. HG swelling is pH sensitive, since its water uptake capacity increases in more basic solutions where its acid groups have higher polarity due to deprotonation. Consequently, the curvature of HG/PI or PI/HG bilayers was controlled through pH variations, with higher pH leading to greater HG swelling, stronger curvature, and smaller diameter in Swiss-roll tube devices. An important point to notice is the shape of the hydrogel layer. Because placing the thin film of metal on top of hydrogel would normally break the metal layer, a hydrogel absence in the shape of a trapezoid was created so that the magnetic structures could be placed atop the stiff layer in the case of rolled-down polymeric platform. For consistency, the identical hydrogel structure was also used in case of the rolled-up platform. The diameter of the rolling can also be tuned with the thickness of polymeric bilayer, where a larger thickness results in a larger rolling diameter. After etching and rolling, the sample was washed in deionization (DI) water and dried under ambient conditions. This technology allowed to process up to 126 functional polymer layer stacks over the entire 50×50 mm^2 substrate in a single fabrication run with a 90-95 % yield (Figure **3.5**c). On top of the predetermined areas in the polymer layer stack, a lift-off photoresist mask was prepared to define the permalloy elements by depositing a film using magnetron sputtering at room temperature as shown in Figure **3.4**(b). Therefore, permalloy deposited on the polymeric platform did not meet high temperatures during the deposition process. The step-by-step fabrication process for roll-down and roll-up geometries is shown in Figure **3.6** and Figure **3.7**, respectively.

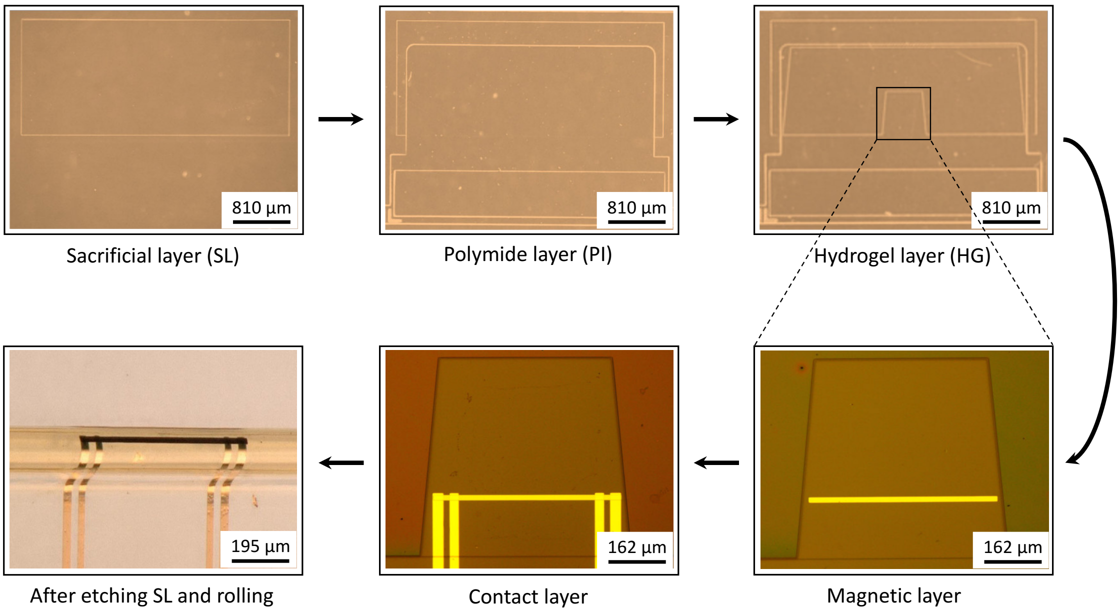
810 µm
Sacrificial layer (SL)
810 µm
Polymide layer (PI)
810 µm
Hydrogel layer (HG)
162 µm
Magnetic layer
162 µm
Contact layer
195 µm
After etching SL and rolling

Figure 3.6: Fabrication steps for rolling polymeric platform (with AMR device) downwards.

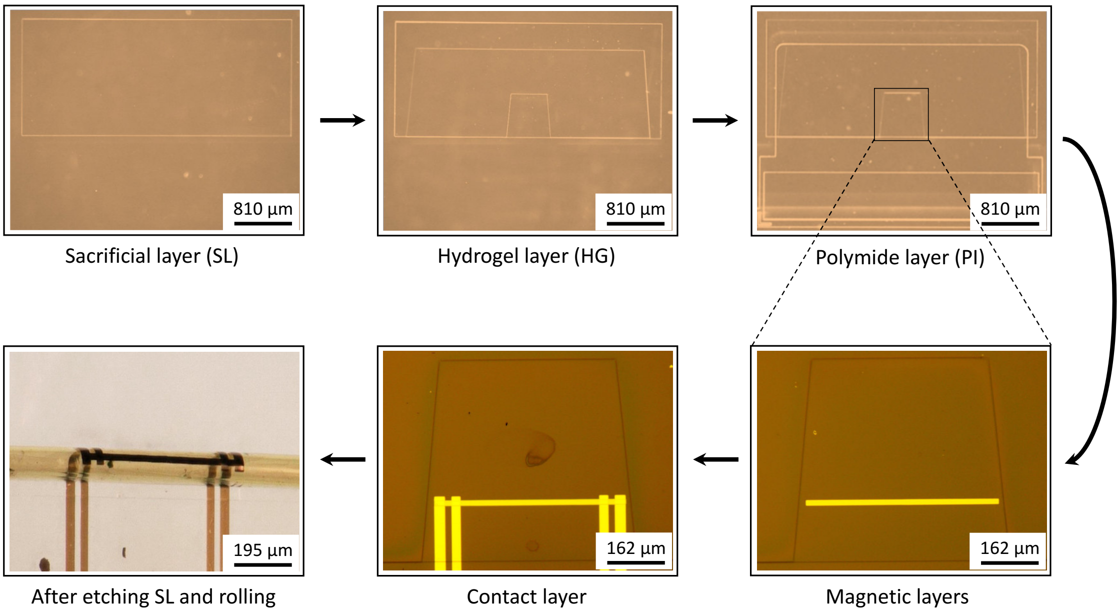
810 µm
Sacrificial layer (SL)
810 µm
Hydrogel layer (HG)
810 µm
Polymide layer (PI)
195 µm
After etching SL and rolling
162 µm
Contact layer
162 µm
Magnetic layers

Figure 3.7: Fabrication steps for rolling polymeric platform (with AMR device) upwards.

Chapter 4 CHARACTERIZATION METHODS

This chapter provides a brief introduction to numerical and characterization techniques and specific information on the procedures utilized in the dissertation for magnetic imaging, electrical characterization, and micromagnetic modeling.

4.1. MAGNETIC FORCE MICROSCOPY

Magnetic force microscopy (MFM), which was first demonstrated in 1987,[121,122] is a well-established and widely utilized technique in a wide range of applications where the visualization of locally distributed stray fields of thin film materials is of primary importance. Using a magnetic tip, MFM is a non-contact variation of atomic force microscopy (AFM) that involves two scans (or "passes"). The first scan uses tapping mode AFM, which is sensitive to the van der Walls interaction between the tip and the sample surface, to record the topography. A second scan is performed by lifting the probe away from the sample surface and repeating the first topography profile at a constant height. As a result, in the second scan, the tip is sensitive to long-range interactions including magnetic and electrostatic interactions while avoiding van der Walls interactions. Therefore, in the second scan, the interaction between the tip's magnetization and the sample's stray field causes a shift in phase ($\Delta\phi$), frequency ($\Delta\omega$), and amplitude (ΔA) between the excitation (i.e., initially driven parameters, i.e., ϕ_0, ω_0, and A_0, respectively), and the measured oscillation of the cantilever. These parameters are proportional to the strength of the magnetostatic force gradient and are recorded. MFM is the most popular technique for observing magnetic domain wall structures (Figure **4.1**a) due to its high spatial resolution (~10 nm),[123] sensitivity (~10 pN),[124] relative ease in sample preparation, capability to apply in situ magnetic fields to study magnetization processes,[125] and ability to operate in various environments.[57]

An extension of conventional magnetic force microscopy, a high-frequency magnetic force microscopy (HF-MFM) technique was used in 2007 by Koblischka et al.[58,60] to visualize the high-frequency stray fields (temporal dynamics) emerging from a hard-disk writer pole. A so-called dual vibrational technique,[126] where the cantilever was driven not only by the piezoelectric element but additionally by the amplitude-modulated, high-frequency stray field of the hard disk writer pole, was used to get the optimum magnetic contrast. Despite these few approaches to measure dynamical processes, direct observation of the magnetic domain wall dynamics with a nanoscale resolution has not been tackled so far.

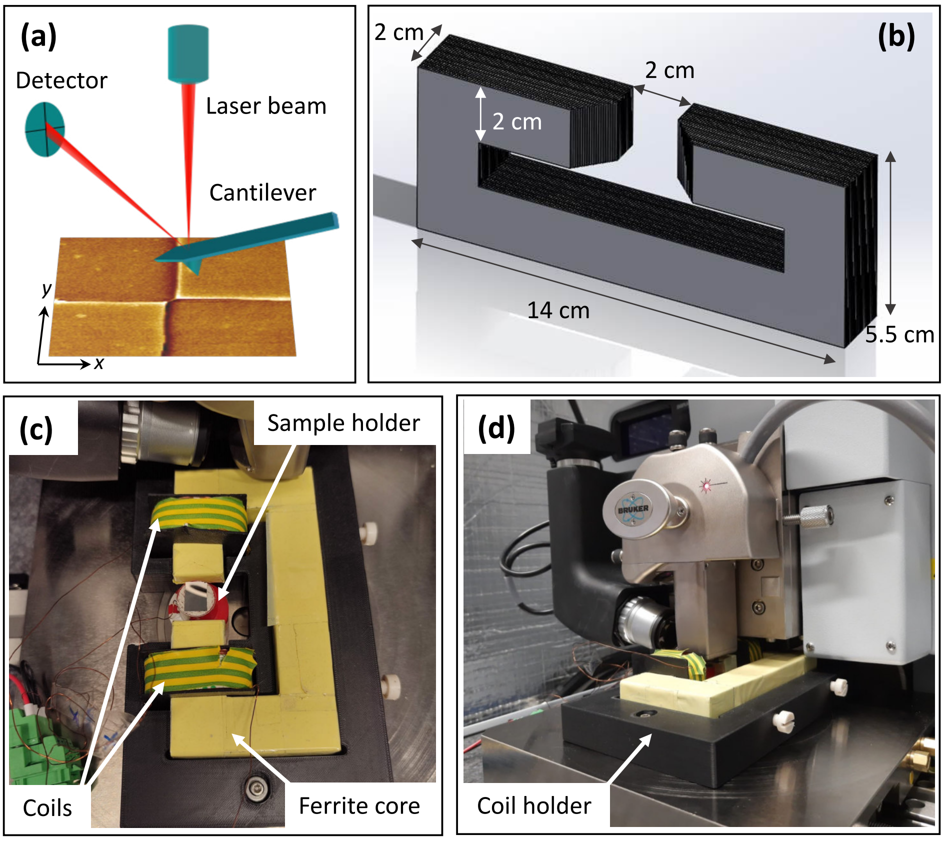

Figure 4.1: Magnetic force microscopy setup: (a) MFM image with a schematic of MFM setup. **(b)** Rotated view of ferrite core used in electromagnetic coil (EM). **(c)** Top view of the EM coil. **(d)** MFM setup with the installed homemade EM coil. Image (c) and (d) were taken at Institute for Integrative Nanosciences, Leibniz-IFW Dresden

In this dissertation, a novel approach based on time-averaged imaging is developed to capture the sinusoidally oscillating DW. In the current experimental setup with an electromagnetic coil (Figures **4.1**b and c), the frequency of the exciting field is limited to frequencies of up to 1 kHz due to an increase in coil's inductance and connected reduction in field amplitude at higher frequencies. The developed time averaged MFM contrast mechanism is expected to work at much higher frequencies, but will have limitations when the DW frequency f_{DW} becomes closer to the resonance frequency f_0 of the cantilever. Nevertheless, for MFM cantilevers with higher resonance frequencies, time averaged MFM imaging of domain wall oscillations up to several ten kHz ($f_{\mathrm{DW}} < 0.1\, f_0$) is expected to work.

(a) Slow-scan axis – enabled

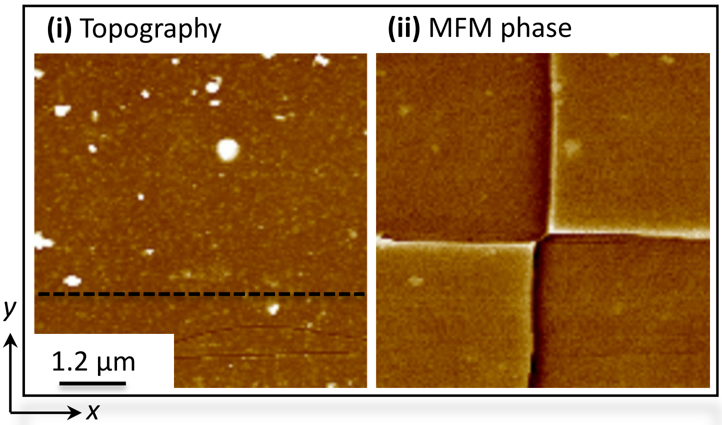

(b) Slow-scan axis – disabled

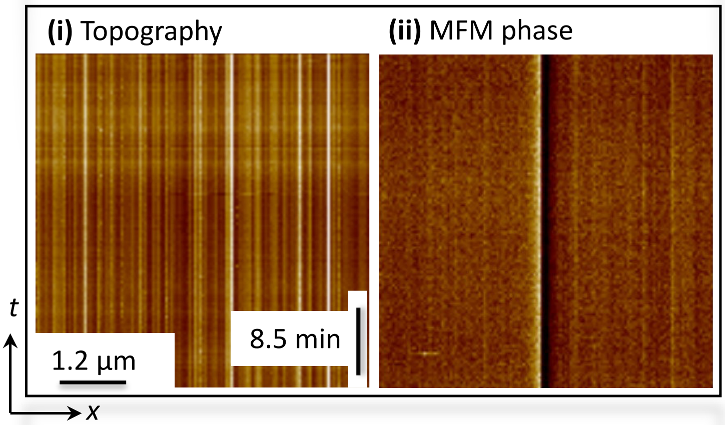

Figure 4.2: Topography and magnetic contrast of a permalloy thin-film structure: (a) Imaged in the 'slow-scan axis' enabled mode, the MFM tip scans along the *x*- (fast-scan) and *y*- (slow-scan) dimension of the structure. **(b)** Imaged in 'slow scan axis' disabled mode, MFM scans repetitively along the *x*-axis along the dashed line shown in Figure **4.2**a. Note that the vertical axis in Figures **a** to **b** changes from space to time.

MFM imaging is performed using an Icon Nanoscope AFM device (Figure **4.1**d) and commercial Team Nanotec high-resolution MFM tips (team-nanotec, MFM-ML1-225-C2.8), with Co-alloy hard magnetic coating of thickness 20 nm, tip radius 15 nm, stiffness 3 N/m, and resonance frequency 75 kHz. Time-averaged MFM imaging is performed at a lift height of 30 nm, in 'slow-scan axis' disabled mode. In contrast to normal MFM imaging (Figure **4.2**a), disabling the slow-scan axis disables the movement of the cantilever along the y-direction, and the cantilever performs a repetitive scan along a single line (Figure **4.2**b). The translational symmetry of the 180-degree DW (of Landau pattern) along the y-axis allows disabling the y-axis scan without losing information. In this mode, the image's y-axis corresponds to a time-axis clocked by the scan rate of the cantilever. The DW is driven by an in-plane field generated by a home-built electromagnetic coil with a ferrite core that can be mounted on the MFM stage. Using a 10-volt AC power supply, it can generate an in-plane magnetic field with a maximum magnitude of 0.25 mT and a frequency of 1 kHz.

4.2. KERR MICROSCOPY

Kerr microscopy,[103] which is based on the magneto-optical Kerr effect (MOKE), can be used to visualize the surface magnetization of a magnetic sample. Depending on the orientation of the magnetization, when linearly polarized light is reflected from a magnetic surface, the polarization angle is rotated by a small angle either clockwise or counterclockwise. The Kerr rotation is proportional to the sample's magnetization component along the direction of the reflected light beam. It is defined as the (small) angle between the normally reflected light and that portion of the light that has experienced the rotation of the polarization plane. There are three types of the Kerr effect, determined by the orientation of the magnetization relative to the incidence plane. The longitudinal Kerr effect is observed if the magnetization at the sample surface is in-plane and aligned along the plane of incidence. Figure **4.3**a depicts the schematics of the longitudinal Kerr effect, in which linearly polarized light, polarized along the plane of incidence, falling on a magnetic sample under the angle of incidence θ, undergoes a rotation of angle ϕ_K and - ϕ_K upon reflection from the sample surface with antiparallel magnetization orientation. The rotation is detected using an analyzer oriented at an angle other than zero with respect to the polarizer direction.

The transverse and polar Kerr effects occur when the magnetization is perpendicular to the plane of incidence (but still in plane) and parallel to the surface normal, respectively (not shown here). The longitudinal Kerr effect, in which the magnetic field and the plane of incidence are aligned, was used throughout the dissertation. Sweeping an external field then allows for the recording of the hysteresis curve and the determination of the magnetization reversal process. The references[31,127] include information regarding Kerr imaging and the Magneto optical Kerr effect.

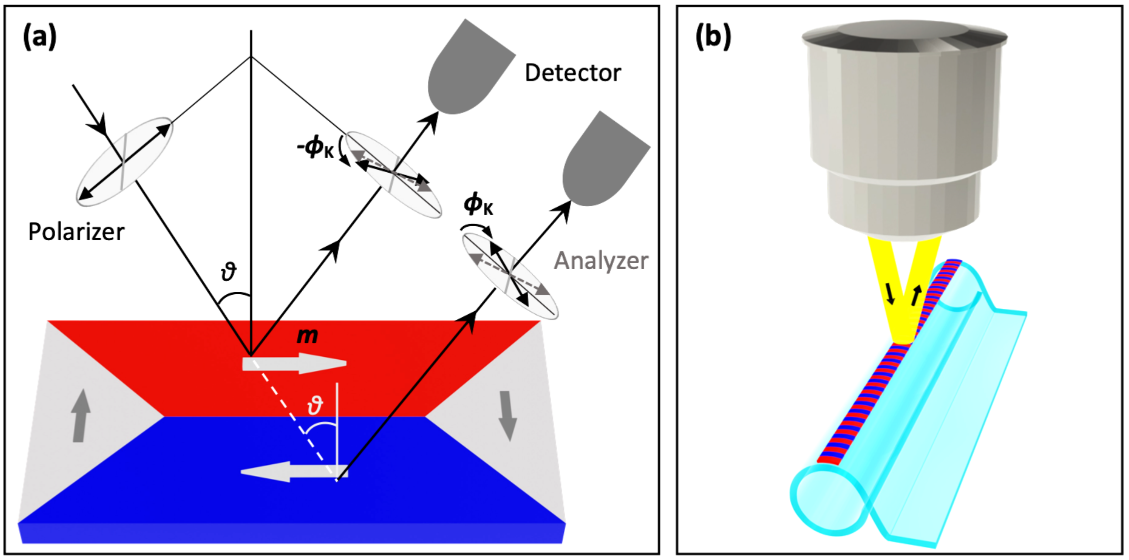

Figure 4.3: Kerr imaging: (a) Schematic of longitudinal Kerr effect. **(b)** Imaging curved structures using reflection techniques, such as Kerr microscopy. Magnetization in cylindrical objects with a diameter of 60-100 µm can only be visualized in an approximately 15-20 µm narrow strip on the structure's dome.

The setup of Kerr microscopy together with electromagnetic coil is shown in Figures **4.4**a and b. LED lamps together with a polarizer are used in microscopy to emit polarized light that travels through the objective to the sample surface, where it is reflected and undergoes Kerr rotation. After reflection, the light is collected by the objective and sent through a second polarizer (called the analyzer) before reaching the digital camera sensor. The use of visible light has several implications, such as the spatial resolution of about 120 nm and a penetration depth of 20 nm for transition metals. Kerr microscopy captures magnetic domains, as shown in Figure **4.4**c, the images c-i and c-ii presents the magnetic domains of permalloy film, imaged in longitudinal sensitivity with light incidence from the *x*- and *y*-axis, respectively.

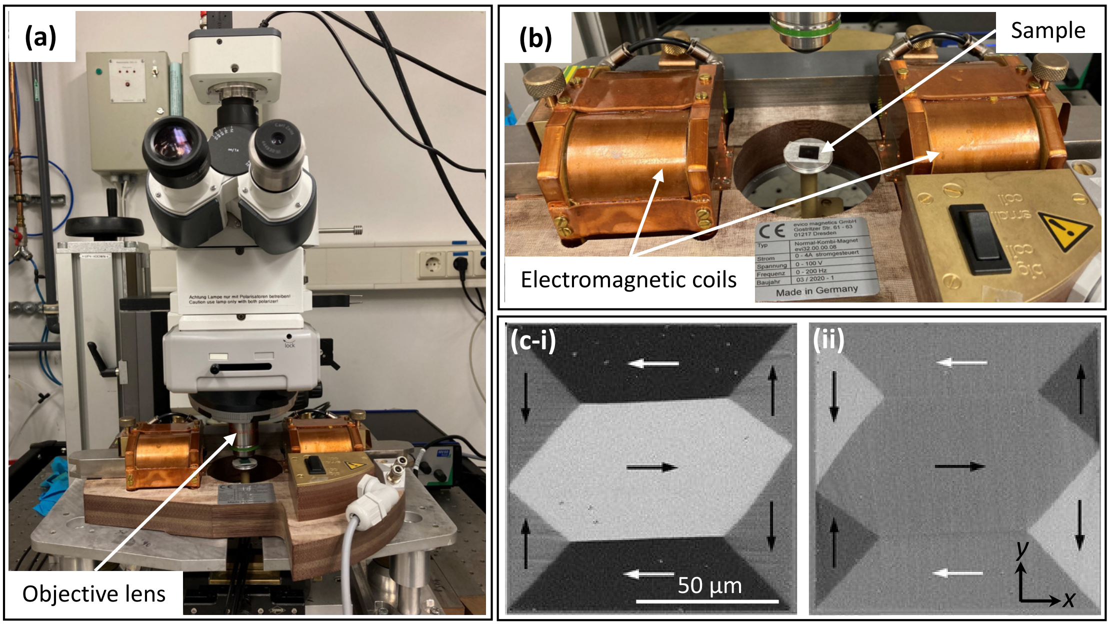

Figure 4.4: Kerr microscopy setup and imaging: (a) Kerr microscopy setup with an electromagnetic coil can generate in-plane dc- and ac-field at the sample location. **(b)** Top view of the electromagnetic coil. Kerr microscopy images are taken from the lab of Prof. Rudolf Schäfer (Institute for Integrative Nanosciences, Leibniz-IFW Dresden) **(c)** Magnetic domains of permalloy patterned film element, thickness 240 nm (taken from[103]).

Slow domain dynamics (low frequency) can be observed visually as fast as the eye can follow. For faster dynamics (or higher frequency), valuable information can be obtained by regular difference-image processing (time-averaged imaging) or stroboscopic imaging. However, the difference-image processing is more robust, as it is easy and fast to perform. Difference-image processing does not reveal the dynamic processes by themselves because in case of continuous ac-excitation, they are smeared out by the averaging procedure. In this dissertation, continuous ac-excitations are employed to study DW dynamics and a mathematical model was developed to analyze the smeared signal. The developed fitting function can provide details about the DW motion's linearity and trajectory together with the exact value of DW oscillation amplitude.

Two additional aspects must be considered when dealing with curved magnetic architectures, a limited probe area and a significant loss of intensity due to large diffuse scattering from the curved surface. The experiment limitation using a magnetic cylindrical object is that the magnetic contrast can be visualized only of a narrow stripe

(20-30 µm-wide at the very top), as shown in Figure **4.3**(b). Thus, although an essential tool for pre-characterization, Kerr microscopy cannot be applied to determine magnetic domain patterns of curved structures sitting at the bottom or inner regions.

4.3. MICROMAGNETIC SIMULATIONS

To understand and support experimental findings, micromagnetic simulations were performed using the Object Oriented MicoMagnetic Framework (OOMMF) from the National Institute of Standard and Technology (NIST). OOMMF is based on the solution of the Landau-Lifshitz-Gilbert (LLG) equation applied to finite elements into which the material is to be subdivided. OOMMF discretizes the sample using a grid of cubic cells with a chosen side and considers a uniform magnetization inside each cell. The simulation implements the LLG Eq (2.16), with the effective magnetic field, defined by $H = \frac{\partial E}{\partial M}$. Here, E is the energy density and consists of all energy terms $E = E_{\text{ex}} + E_{\text{demag}} + E_{\text{zeeman}} + E_{\text{anisotropy}}$. Simulation parameters for permalloy material[128] were considered as follows:

Table 4.1: Material parameters for permalloy used in micromagnetic simulations.

Parameter's name	Symbols	Values
Saturation magnetization	M_s	$8 \times 10^5\ A[m]^{-1}$
Exchange constant	A	$1.3 \times 10^{-11}\ J[m]^{-1}$
Magnetocrystalline anisotropy energy constant	K	$0\ J[m]^{-3}$
Damping constant	α	0.05

In all simulations, the average cell size is chosen to be in the order of exchange length, l_x ($= \sqrt{2A/\mu_0 M_s^2} = 5$ nm for permalloy) or smaller. The magnetization vector should barely vary from one cell to another to fulfill the assumptions of micromagnetics. This approach is generally valid for reproducing both static and dynamic behavior seen in experiment or predicted by theory.

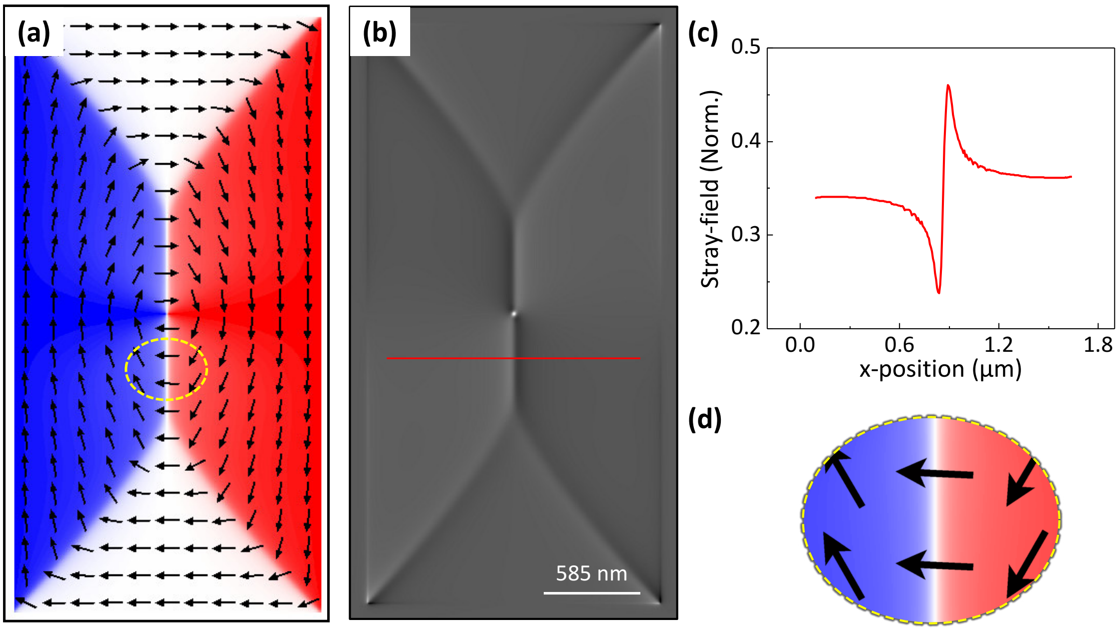

Figure 4.5: Micromagnetic OOMMF simulations: (a) Magnetic domain pattern of a permalloy rectangle of thickness 20 nm. **(b)** *z*-component of stray-field at the height of 4 nm above the rectangle surface showing an MFM-like image of the Landau domain configuration. **(c)** Intensity profile of the *z*-component of DW stray-field across the 180-degree DW. **(d)** Magnified image of the spin configuration at the 180-degree DW in Landau domain configuration.

An example for a permalloy rectangle with Landau domain configuration is seen in Figure **4.5**. Panel (a) displays the domain pattern after relaxation of the magnetization from the two-domain state (both same size and oriented antiparallel to the long edge). The Néel character of the central 180-degree DW is emphasized in panel (d). To estimate the expected MFM contrast, the z-component of the stray field above the rectangle surface at the height of 4 nm is shown in panel (b). It leads to a characteristic profile across the DW (see Figure.**4.5**c).

For hysteresis purposes, the simulation was started with a field large enough to align magnetization with the external field. The magnetic field was then gradually reduced. At each field step, the magnetization has been relaxed with the torque minimization process.

For quasistatic DW dynamics in permalloy rectangles, simulations are performed in two following steps.

1. Initial magnetization was set to two domain states (both same size). Within these two domains, magnetization was oriented parallel and antiparallel to the long axis of the

rectangle. Then, the ground state (Landau structure) of permalloy rectangles was achieved by torque minimization process in the absence of an external magnetic field.

2. In the presence of a gradual increase (step size of 0.1 mT) in magnetic field $\mu_0 H_y$, at each field step, the displaced DW equilibrium position is achieved by torque minimization process.

Due to the static magnetic field, DW gets displaced in the x-axis. To extract the displaced DW position, m_y component of magnetization profile across the 180-degree DW is analyzed, and for the Neel type DW, the x-position with the lowest m_y value, is named as DW position.

4.4. ELECTRICAL CHARACTERIZATION & MAGNETO-TRANSPORT

The electrical resistance R is determined by applying a known electrical current I between two outermost electrical contacts and measuring the voltage drop V between two inner contacts attached to an elongated material stripe. In this four-probe configuration, the cable and contact resistance is excluded. In magneto-transport experiments, change in resistance as a function of the external field $\mu_0\mathbf{H}_{\mathrm{ext}}$ is determined. Typically, the measurements are initialized by a high magnetic field to saturate the sample and obtain a defined magnetic state. Subsequently, the field is lowered in steps. After every change to the field setpoint, the magnetization arrangement reorients itself to accommodate the new torque.

4.4.1. ANISOTROPIC MAGNETORESISTANCE (AMR)

The AMR effect, discovered by Lord Kelvin over 150 years ago, occurs in magnetic materials due to the spin-orbit interaction.[129] It causes the resistance to depend on the relative angle between magnetization and electrical current.

$$AMR \propto Cos^2\theta \tag{4.1}$$

Where θ = $(\mathbf{m},\hat{\boldsymbol{J}})$ is the angle between the magnetization $\mathbf{m}(\mathbf{H})$ and the electric current flowing along the stripe's long axis.

The AMR response connects the electrical transport to the magnetization orientation leading to a configuration dependent resistance according to the Eq (4.1).[31] It, therefore, can be used as a fingerprint of well-defined magnetization orientation, which is the result of effective magnetic anisotropy, and to study the magnetization reversal processes. The magnetic field range in which the AMR effect can be observed depends on the field needed to change the magnetization direction.

In the experimental AMR setup, the current I is controlled, and voltage V is measured by a Keithley 2400 source meter. The current (1 mA) is applied along the permalloy stripe. All the AMR hysteresis presented are results of single scan measurements.

4.4.2. MICROSCOPIC CALCULATION OF AMR

Due to the formation of domains, the magnetization $\mathbf{m}(\mathbf{H})$ is a local quantity and the AMR needs to be calculated via a discretized model based on simulated magnetization configurations.

First, the resistivity parallel and perpendicular to $\boldsymbol{J}$ are defined as $\rho_{\parallel}$ and $\rho_{\perp}$, respectively. Then, the calculations of the AMR of the simulated magnetic stripes were performed in the following steps.

1. Partitioning the stripe in many slides (as shown in Figure **4.6**) with thickness Δx (5 nm): Since the current is flowing transversely in each slide, the resistance associated with this section can resemble as a bunch of resistances connected in parallel, each resistance per cubic cell (side, 5 nm) around the point (y,z) belonging to the slide.

2. Considering the slides as a bunch of resistances connected in series: The total resistance will be obtained by adding all the resistances associated with each slide.

Resistivity (ρ) for a stripe, with current flowing along x-axis is given by,

$$\rho[x, y, z] = \rho_{\perp} + (\rho_{\parallel} + \rho_{\perp}) m_x[x, y, z]^2$$

Resistance after performing the mathematical calculations for the above two steps,

$$R[L, W, t] = \sum_{n=1}^{n_x} (\sum_{m=1}^{n_y} (\sum_{p=1}^{n_z} \frac{\Delta x . \Delta z}{\rho[x_n, y_m, z_p] . \Delta y})^{-1})^{-1}$$

AMR ratio in percentage,

$$AMR[\%] = \frac{R[t, W, L] - R_{\perp}}{R_{\perp}} \times 100$$

where $n_{x,}\, n_{y,}\, n_z$ are the numbers of cells along the length (x-axis), width (y-axis), and thickness (z-axis) of the stripe, and $R_{\perp} = \frac{\rho_{\perp} L}{tW}$ is the resistance when the stripe is magnetized transversely to its axis.

The values $\rho_{\perp}$ (24.075 × 10^{-8} Ω.m) and $\rho_{\parallel}$ (24.793 × 10^{-8} Ω.m) were taken from the experimentally determined resistance values when the permalloy stripe (L = 550 µm, W = 15 µm and d = 100 nm, used in this dissertation) is saturated transverse and along the stripe axis, respectively.

Microscopic AMR was formulated by Prof. Dr. Jorge A. Otálora (Universidad Católica del Norte, Chile).

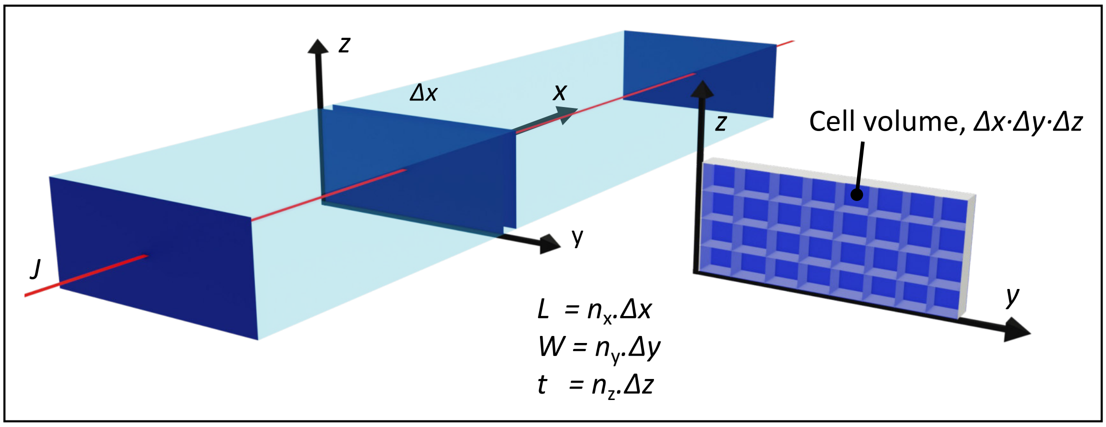

Figure 4.6: Illustration of subdivision of stripe into cells for the AMR calculations: The figure on the right side shows a magnified view of one slide of stripe to illustrate the cell divisions. Each slide along the x-axis is considered similarly.

Chapter 5 INDUCED ANISOTROPIES IN CURVED MAGNETIC MEMBRANES

This chapter investigates the impact of rolling on the static magnetic characteristics of micron-sized soft ferromagnetic thin-film elements. Self-assembly rolling of magnetic elements deposited on top of an initially planar polymeric platform creates curved structures with a curvature radius in the tens of micrometers. Fabricating micron-sized curved structures with small dimensions along the circumference allows to exclusively probe the influence of strain and to disregard the possible changes in the magnetostatic interactions that originate from curving the magnetic membrane. By varying the polymeric platform architecture, the rolling direction and the rolling diameter are tuned to tailor the surface strain of the magnetic structure. The resulting strain and curvature on the magnetic ground state is thoroughly studied by magnetic microscopy, and micromagnetic simulations, and the anisotropy is quantified using electrical measurements. Data provided in this chapter were previously published in the scientific journal npj Flexible Electronics listed below[130] and are reprinted here under the terms of license CC BY 4.0:

“B. Singh, J. A. Otálora, T. H. Kang, I. Soldatov, D. D. Karanushenko, C. Becker, R. Schäfer, D. Karnaushenko, V. Neu and O. G. Schmidt, Self-assembly as a tool to study microscale curvature and strain-dependent magnetic properties. *npj Flex Electron* 6, 76 (2022).”

5.1. ROLLED-DOWN AND ROLLED-UP MICROELEMENTS

The functional ferromagnetic elements were deposited on a transformable polymeric platform (PP) comprised of a bilayer of hydrogel (HG) and polyimide (PI) to enable self-assembly rolling. To achieve bending with positive and negative curvature, the order of the HG and PI layers in the polymeric platform must be switched (explained in detail in the fabrication chapter). Due to the considerable stiffness (Young's modulus, Y_{PI} = 3.2 GPa)[102] and thickness of the PI layer, the strain state is hardly influenced by the functional magnetic layer, and the full layer stack can be rolled down (Figure **5.1**a) or rolled up (Figure **5.1**b) into tightly rolled tubes with diameters adjustable by the thicknesses of the PI and HG layers, and the pH of the rolling solution. Consequently, both the sign and magnitude of the curvature and strain state in the functional layer are tunable by the rolling direction (up or down) and rolling diameter, respectively. Figure **5.1**a displays schematics for tensile strain in rolled-down structures, while Figure **5.1**b depicts schematics for compressive strain in rolled-up structures. In this example, a ferromagnetic $Ni_{78}Fe_{22}$ stripe was prepared on top of the PP prior to the rolling. As the strain was created in a post-growth stage, no surface or curvature-related alterations were possible during the creation of the functional layer, isolating the effect of strain. This offers a macroscopic strain stage on the scale of the self-assembled tubular structure, with diameters as small as 20 μm.

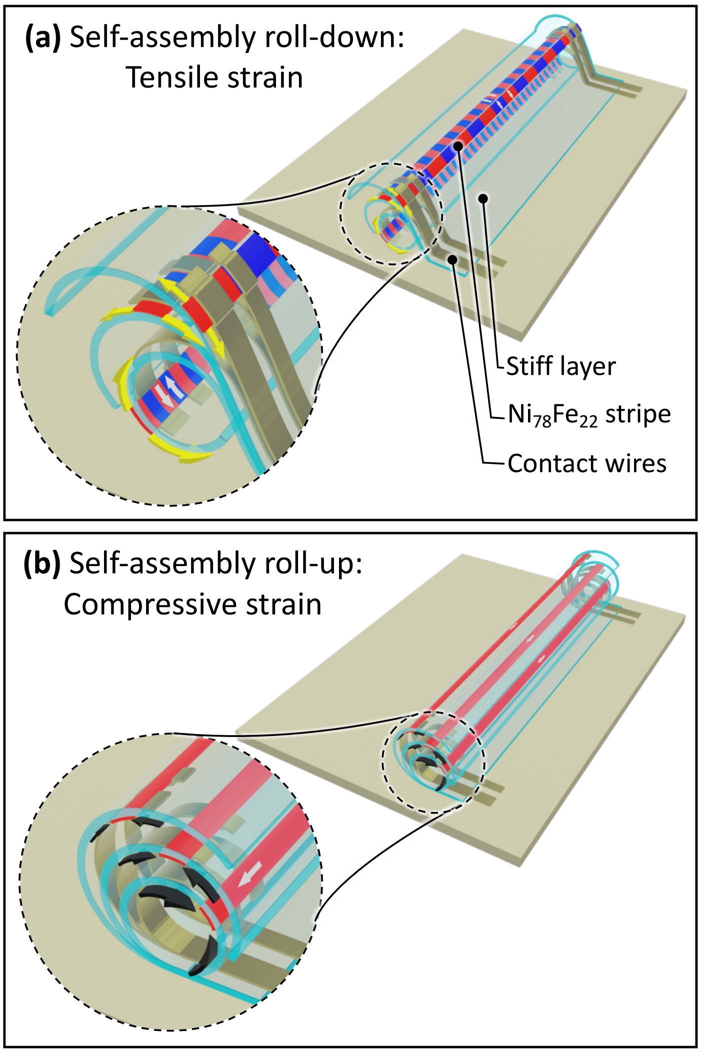
(a) Self-assembly roll-down:
Tensile strain
Stiff layer
Ni78Fe22 stripe
Contact wires
(b) Self-assembly roll-up:
Compressive strain

Figure 5.1: Schematics of **(a)** roll-down and **(b)** roll-up self-assembly approaches. Yellow and Black arrows indicate the magnetic strip's tensile and compressive stress direction, respectively.

5.1.1. MAGNETIC DOMAINS

Magneto-optical Kerr microscopy immediately reveals the influence of strain on the domain structure of 100 nm-thick, micron-sized $Ni_{78}Fe_{22}$ elements. In the unrolled state, patterns with an aspect ratio of 1:1 (discs and squares) adopt a point-symmetric flux closure configuration in accordance with the van den Berg's principle[31], as observed in the Kerr images (Figure **5.2**a), with no magnetization direction being favored. Elongated structures (rectangles and long stripes) lower their magnetostatic energy by prioritizing domains along the long axis of the patterns (Figure **5.2**a).[127]

After self-assembled roll-down, Kerr images with sensitivity along the vertical axis in the image attest a distinct preference for magnetization orientation transverse to the stripe's long axis, namely in the tube’s azimuthal direction (Figure **5.2**b). This is understood from the following equation;

$$K_\mathrm{u} = (3/2)\sigma\lambda \tag{5.1}$$

K_u, a positive magnetoelastic energy constant in the orientation of the uniaxial strain, is the result of the positive magnetostriction (λ) of the $Ni_{78}Fe_{22}$ layer and the positive (tensile) stress ($\sigma > 0$) upon rolling down. In the case of a self-assembled rolled-up (Figure **5.2**c), uniaxial compressive stress ($\sigma < 0$) causes the sign of the magnetoelastic energy constant to reverse. As a result, a magnetization perpendicular to the uniaxial stress axis is preferred, resulting in fundamental domains that are now axially magnetized.

(a) Before rolling

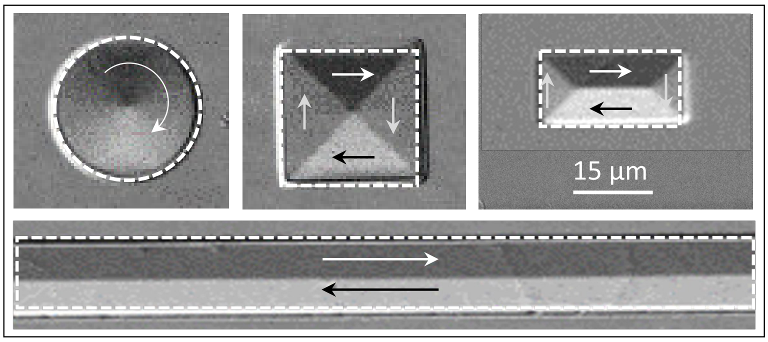

(b) After rolling-down

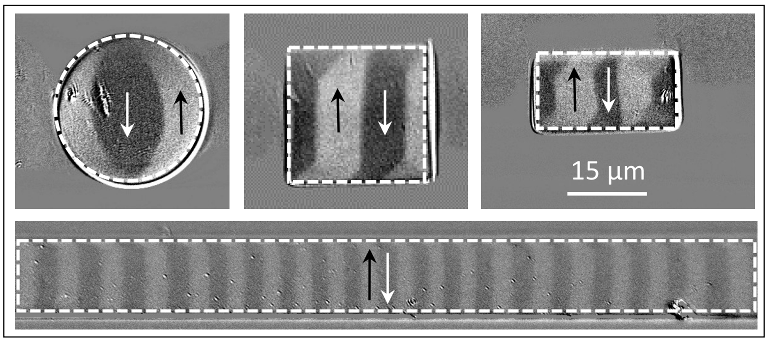

(c) After rolling-up

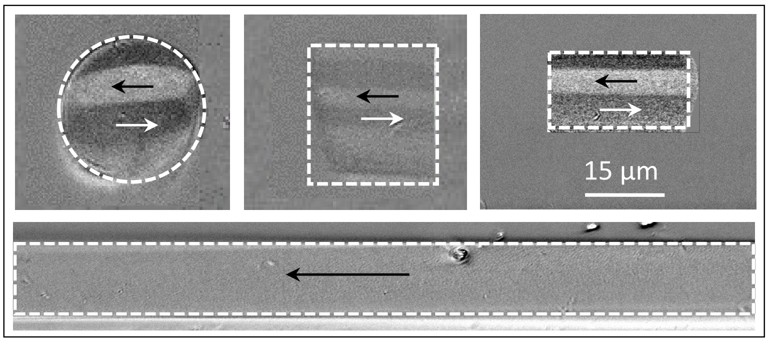

Figure 5.2: Magnetic domains before and after rolling the elements: (a) Formation of a flux-closure domain configuration before rolling. Domains in roll-down **(b)** and roll-up **(c)** elements.

5.1.2. MAGNETIZATION REVERSAL WITH AN AXIAL FIELD

Understanding the magnetization reversal of functional materials is one of magnetism's key concerns. In the case of 3D curved geometries, this effort is increased by the inaccessibility of the entire structure using direct imaging techniques. Such an analysis is only possible when the functional structure is completely within the field of view, i.e., on the dome of the self-assembled tube (Figure **5.3**a), and when the curvature of the structure is small enough to reflect light from the structure's surface to the objective of the microscope. Strategic fabrication, such as fine-tuning the magnetic element's width (small enough along the tube's circumference) and the polymeric tube's diameter, enabled magnetic elements to sit on the tube's dome, making them accessible to Kerr microscopy. To ensure a well-controlled field orientation regardless of the position of the magnetic stripe within the self-assembled tube, a field parallel to the tube axis and thus along the stripe length was chosen. MOKE hysteresis performed in the presence of an axial field in magnetic stripes before and after rolling illustrate the direction of induced anisotropies (Figure **5.3**b). In the case of planar stripes (blue line), the shape-dominated anisotropy along the stripe's long axis results in a square-shaped, easy-axis hysteresis with a sharp magnetization reversal at a field that is referred to as the nucleation field, H_n. The strain-induced anisotropy axial to the stripe axis in rolled-up tubes is visible as an increased nucleation field and a sharper magnetization reversal of the hysteresis (green line). In rolled-down tubes, however, the generated transverse anisotropy increases the saturation fielsd of the hysteresis (red line).

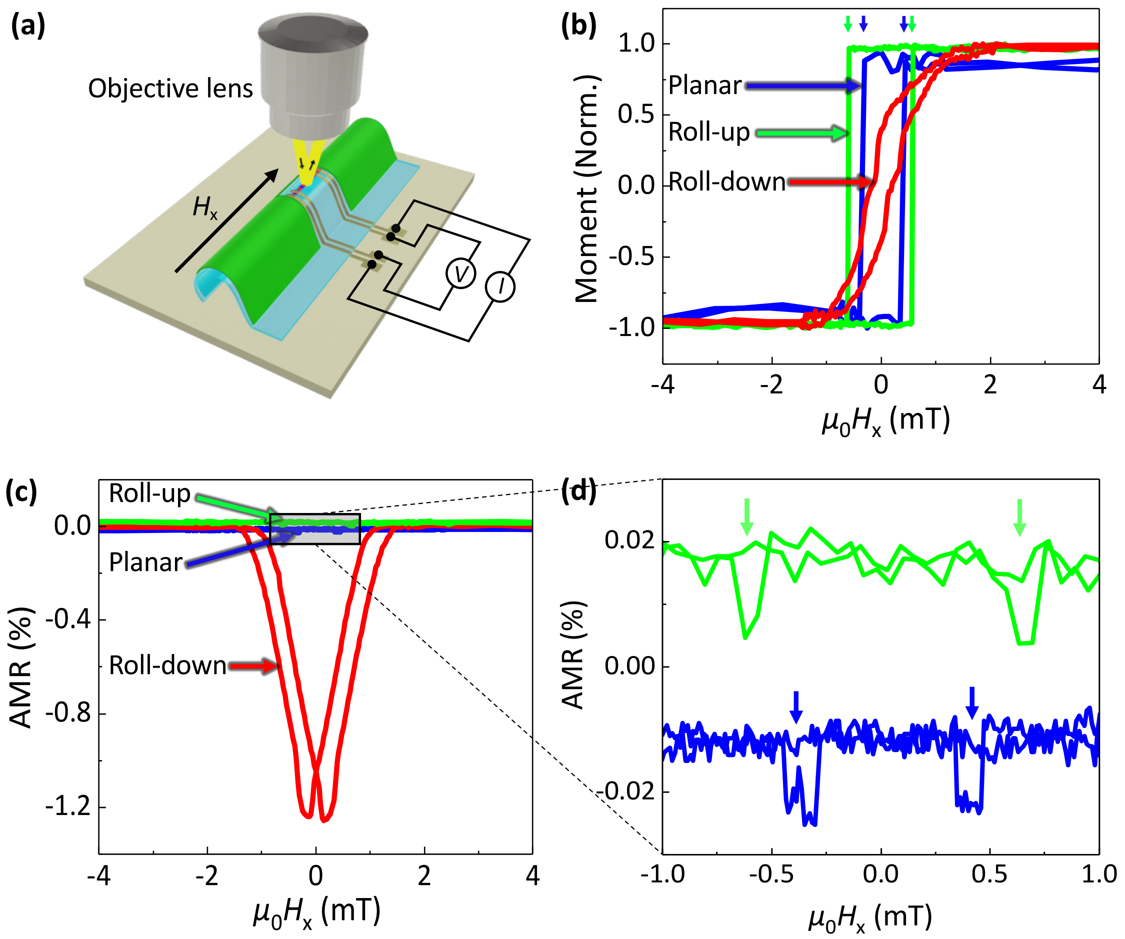

Figure 5.3: Hysteresis measurements on a permalloy stripe: (a) Schematic setup for simultaneous magneto-optical and AMR measurements of a stretched magnetic stripe resting on the polymeric tube's dome. **(b)** Magnetic hysteresis and **(c)** AMR hysteresis was recorded simultaneously on the $Ni_{78}Fe_{22}$ stripe with a field along the stripe's long axis before and after rolling. **(d)** View of the curves in Figure **5.3**c at low field.

Although magnetic hysteresis shape and saturation field give an idea of induced anisotropy direction and magnitude, respectively, the retrieval of anisotropy from the AMR response is a far more elegant method. The introduction of a magnetic field rearranges the magnetic domain state and consequently the local orientation of magnetic moments with respect to the current direction, results in a resistance that is configuration-dependent according to Eq (4.1). As the magnetization in flat stripes is predominantly oriented along the same axis as the electric current direction I_x, the AMR signal is constant except for fields around H_n, where the reversal process causes a moderate divergence of magnetization from the electric current axis (Figure **5.**3c and d).

This leads to the observed peak-like reduction in AMR signal. This behavior does not change qualitatively when compressive strain in the rolled-up condition reinforced the shape anisotropy with an extra uniaxial anisotropy along the tube axis. The higher effective anisotropy value only enhances the nucleation field, as visible in the AMR signal (Figure **5.3**c and d). For tensile strain in the rolled-down condition, however, domains reorient into an azimuthal multidomain state at zero field, leading to the steady reduction in AMR in the same field range (Figure **5.3**c).

To establish electrical (AMR) measurements as a self-sufficient characterization technique for curved geometries, it is necessary to demonstrate the correlation between the global AMR signal and the local magnetization configuration. To accomplish this, the magnetization reversal of the curved stripes was simultaneously investigated with direct Kerr imaging and electrical AMR measurements. Using a magnetic field aligned in the $+x$ direction, the magnetization of planar, rolled-up, and rolled-down stripes initially saturated in the $-x$ direction was reversed.

Figure **5.4**a shows the simultaneous observation of magnetic domains and AMR signal of rolled down stripe when magnetization reversal takes place in the presence of field sweeping along the stripe axis. All the features discussed above in Figure **5.3**c are now detailed by direct Kerr observations. A field that is large enough to align the magnetization along the stripe produces a constant resistance R_{max}. As the field strength decreases, magnetic moments start to rotate away from the stripe axis and gain m_y components due to the induced azimuthal anisotropy. On further reducing the field magnitude, azimuthal domains nucleate with alternating m_y components, and the magnetostatic energy is decreased by the creation of flux closure domains with $\mathbf{m} = m_x$, Figure **5.4**a2.iii (flux closure domains can be easier seen in simulated stripe shown in Figure **5.9**a2.iii). The non-collinear magnetic arrangement ($\mathbf{m}$ non-parallel to I_x) leads to the observed decrease in the AMR, with the absolute value depending on the fraction of closure domains and on the remaining m_x component in the azimuthal domains. At fields close to zero, the magnetic moments in the azimuthal domains are perfectly aligned in the y-direction, and the closure domain size is minimized, corresponding to the minimum in the AMR signal. When the field strength increases, magnetization processes repeat in the opposite direction, and at a saturation field, H_{sat}, the magnetization eventually saturates along the x-axis.

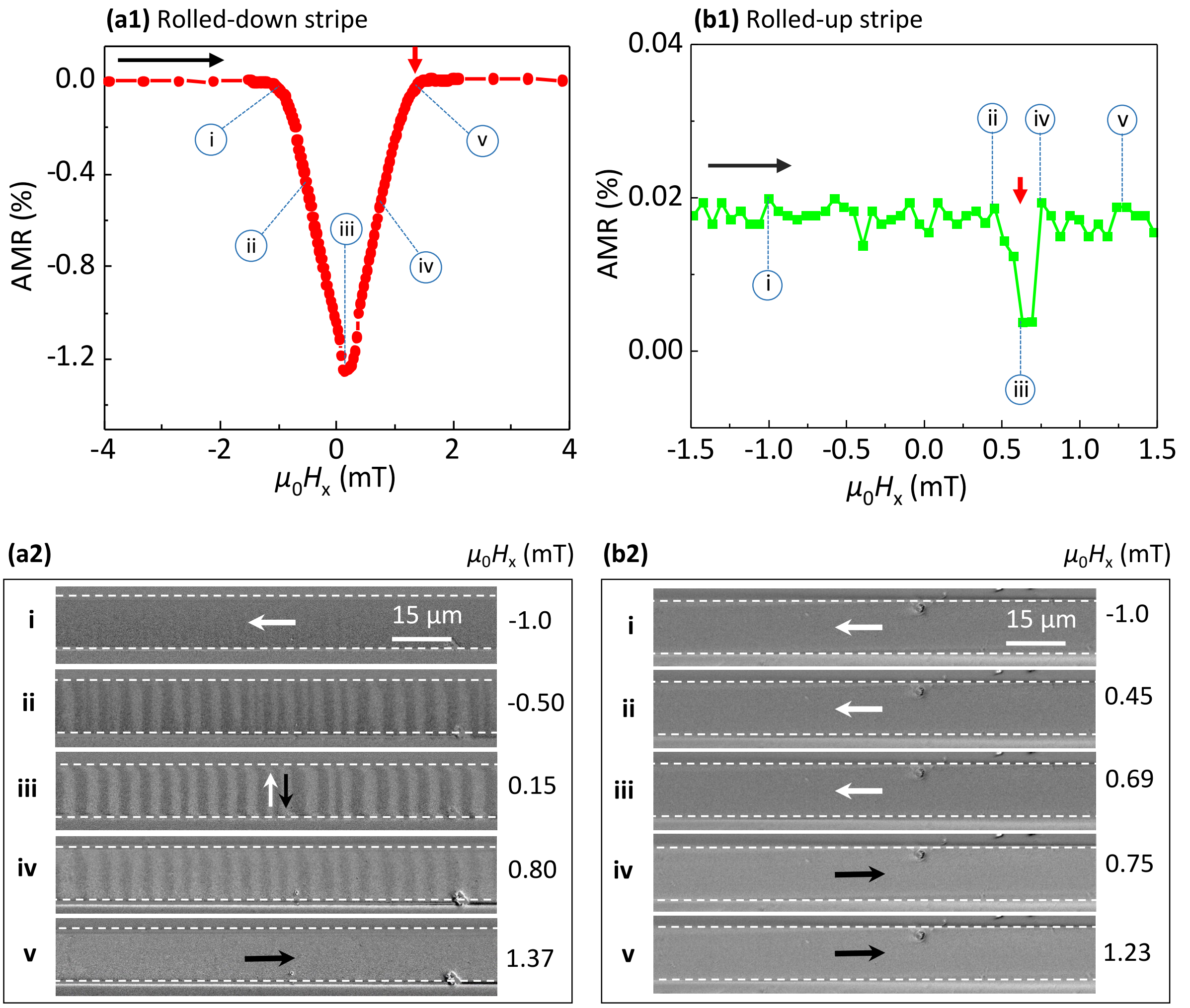

Figure 5.4: Magnetization reversal of rolled magnetic stripes (L = 550 µm, W = 15 µm, d = 100 nm) in an axial field: AMR hysteresis of the **(a1)** rolled-down and **(b1)** rolled-up stripes. The black arrow within the graph depicts the direction of the field sweep, and the red arrow indicates saturation field H_{sat} in (a1) and switching field in (b1). **(a2)** and **(b2)** magnetic domain states captured at various stages of field

Using the following three conditions, a full quantitative description of the strain-induced changes in the AMR signal was developed: (1) due to the even curvature of the rolled-down membrane, the resulting homogeneously induced anisotropy is independent of position and can be seen locally at any place on the dome of the rolled-structure that can be reached by magnetic microscopy; (2) domain observations are linked to a global electronic signal by a simultaneous magnetoresistance measurement; (3) micromagnetic simulations (presented in section 5.3) confirm the correlation between local (microscopic) and global (AMR) behavior as a general feature of an elongated AMR structure and connect the AMR signal quantitatively with the induced anisotropy.

The field $\mu_0 H_{\mathrm{sat}}$ at which both the magnetic and AMR hysteresis saturate corresponds closely to the anisotropy field.[131] This indicated that the anisotropy energy may be calculated from the AMR hysteresis. Assuming the equivalence of $\mathrm{H}_{\mathrm{sat}}$ and $\mathrm{H}_{\mathrm{ani}}$, K_{u} is given by:[132]

$$K_{\mathrm{u}} = (1/2)\mu_0 M_{\mathrm{s}} H_{\mathrm{sat}} \tag{5.2}$$

where M_{s} is the saturation magnetization of permalloy. Although the correlation of H_{sat} with the induced azimuthal anisotropy is expected, it is not trivial for magnetization processes including domain processes and competing anisotropies. Therefore, in section 5.3, micromagnetic simulations are summarized, which provide additional evidence of this approach.

For completeness, Figure **5.4**b depicts AMR signal and magnetic domain evolution of a permalloy stripe in the rolled-up state as a function of an axial field. During the field sweep, the induced anisotropy along the stripe's axis supports the shape anisotropy, resulting in a preferred magnetization along the stripe's long axis. This produces a constant AMR signal except for the narrow field range where magnetization switches its orientation from negative to the positive x-axis. The reduced AMR at the switching field occurs due to rotation of magnetization along the y-direction at the boundaries of the stripes and is thus not visible in the image obtained in the center of the stripe (Figure **5.4**b2.iii), but is visible in the simulated magnetization pattern, Figure **5.9**b2.iii. Due to the induced anisotropy, the switching field in the rolled-up state is increased compared to the planar state (as shown in Figure **5.2**d).

5.1.3. MAGNETIZATION REVERSAL WITH A TRANSVERSE FIELD

The magnetization reversal of an experimentally rolled-down permalloy stripe (Figure **5.5**a) as a function of field transverse to the stripe was investigated with simultaneous AMR (red line) and magneto-optical measurements (blue line) as shown in Figures **5.5**b and d. Magnetic hysteresis (blue line in Figure **5.5**b) and domain imaging (Figure **5.5**d) were performed at the center of the stripe in the region surrounded by the white dashed line (Figure **5.5**a).

Above the saturation field, the magnetization is completely aligned perpendicular to the current flow, resulting in the lowest value of resistance. As the field strength ramps down (approaching zero), due to the shape anisotropy, it is energetically preferable for the magnetic moments to tilt along the long axis of the stripe (*x*-axis), which causes the AMR signal to increase. Additional peculiarities observed in the AMR signal before and after attaining maximum are highlighted in Figure **5.5**c and are explained with simultaneously imaged of magnetic domain configurations (Figure **5.5**d), and micromagnetic simulations described later in section 5.3.2.

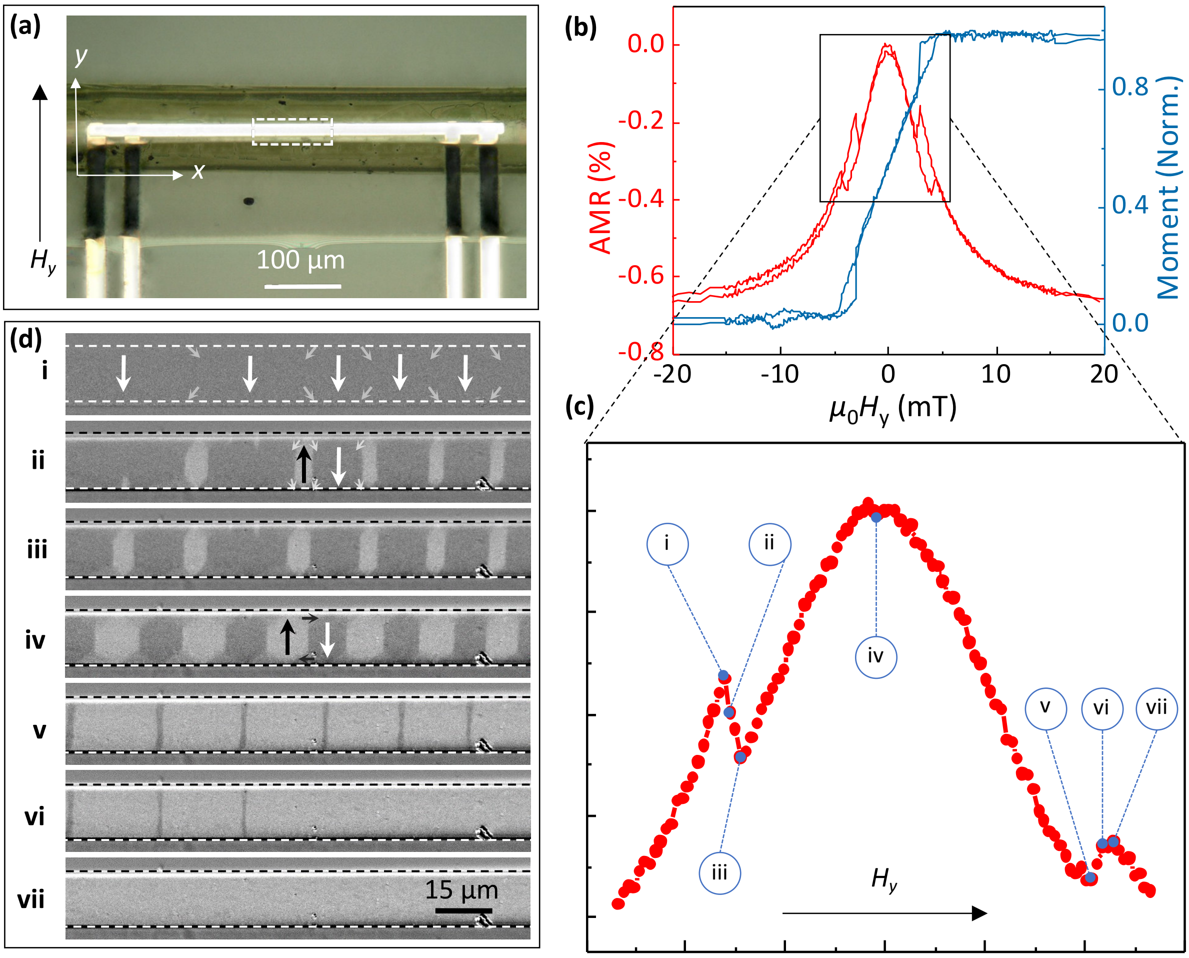

Figure 5.5: Magnetization reversal of a rolled-down stripe in a transverse field: (a) Optical image of the self-assembled rolled stripe with four contacting wires. **(b)** Simultaneous measurement of AMR and MOKE hysteresis. **(c)** Low-field view of the AMR hysteresis for field sweeping in the *y*-direction from negative to positive. **(d)** Magnetic

domains at various stages of the field sweep. The black and white arrows indicate the anticipated direction of magnetization.

In the case of magnetization reversal of domain initially saturated along $-x$-direction (Figure **5.5**c), the increase in AMR signal until point (c.i) indicates a rotation of moments towards the x-direction, which is however not identified in the Kerr contrast (d.i). On further lowering the field strength, domains perpendicular to stripe are nucleated (d.ii and d.iii) owing to induced anisotropy and thus drop in AMR signal (c.ii and c.iii). Nucleated perpendicular domains comes with flux-closure configuration i.e., magnetization at the edges oriented along the stripe length to reduce the magnetostatic energy. Approaching the field strength to zero, increases the size of flux-closure domains and thus axial magnetization component (d.iv) and therefore increase in AMR signal (c.iv). On increasing the field above zero, magnetization processes repeat in the opposite direction, and annihilation of perpendicular domains (d-vi and d-vii) gives rise to increase in AMR (c.vi and c-vii).

An increase in the AMR signal up to point (c.i) in the case of reversal of magnetization initially saturated along the $-y$-direction (Figure 5.5c) indicates a rotation of moments towards the x-direction; this rotation is not, however, identified by the Kerr contrast (d.i). Further reduction in field strength causes nucleation of domains perpendicular to the stripe (d.ii and d.iii) due to induced anisotropy, resulting in a decrease in the AMR signal (c.ii and c.iii). In order to lower the magnetostatic energy, nucleated perpendicular domains have a flux-closure configuration, i.e., magnetization at the edges aligned along the length of the stripe. When the field strength approaches zero, the size of the flux-closure domains grows, as does the axial magnetization component (d.iv) and hence the AMR signal (c.iv). When the field is raised above zero, magnetization processes repeat in the opposite direction, and annihilation of perpendicular domains (d-vi and d-vii) causes an increase in AMR (c.vi and c-vii).

With the simultaneous measurement of magnetic and AMR hysteresis, it became apparent that regions corresponding to the rotation of magnetization cannot be resolved clearly in the magnetic hysteresis. In contrast, all characteristics of the reversal process like magnetization rotation, nucleation, and the annihilation of transverse domains are easily identifiable in AMR hysteresis. This makes AMR measurements a very suitable method for studying magnetization reversal in 3D curved geometries, such as tubular geometries.

5.2. CURVATURE TUNING OF ROLLED-DOWN MAGNETIC STRUCTURES

By rolling the original planar stripe (Figure **5.6**a) into tubes of diameter 64 µm, 105 µm and 130 µm (Figure **5.6**b**,** c and d), the magnetic stripe's curvature can be adjusted. The diameter (ϕ) of the tubes seen in Figures **5.6**b, c, and d was optically determined along the tube's y-axis. Measuring the height of the two tubes (shown in Figures **5.6**c and d) along the z-axis with a profilometer (height profiles shown in Figures **5.6**e and f) and comparing it to the diameter measured along the y-axis demonstrated that the polymeric tubes had elliptical cross-section rather than the ideal circular one. Figure **5.6**e illustrates the sketch of possible elliptical cross-sections of the tubes.

Thus, the radius of curvature varies depending on the position of the stripes around the circumference of the tube. For the stripe that was sitting on the wall of the tube, as shown in the sketch of Figure **5.6**e.i, the radius of the curvature (R) along the y-direction was used in the strain estimation. While for the stripes (Figures **5.6**c and d) that are sitting on the dome (as shown in sketch Figures **5.6**e.ii and e.iii), the radius of the curvature along the z-direction was taken into consideration (i.e., half of the maximum of the height profiles shown in Figures **5.6**f and g). Consequently, for stripe shown in Figure **5.6**b, R = 32 µm and for stripes shown in Figures **5.6**c and d, R = 57.5 µm and 79.5 µm, respectively, were used to estimate the surface strain.

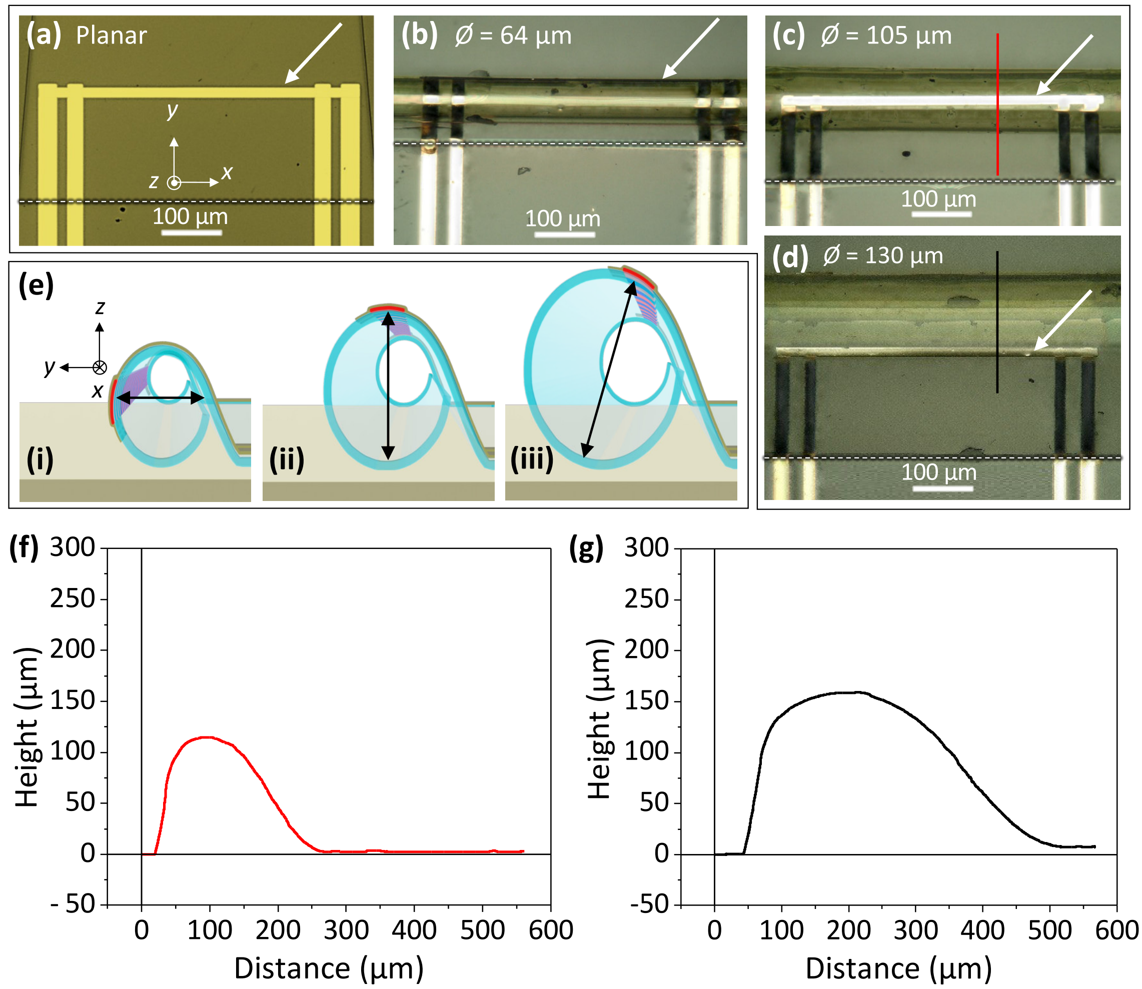

Figure 5.6: Rolled-down magnetic stripes with different curvatures: Optical pictures of **(a)** a flat stripe and **(b, c** and **d)** rolled-down stripes. **(e)** Sketch of rolled-down tube's cross-sections. **(f)** and **(g)** The height profiles of the tubes depicted in Figures **c** and **d,** respectively.

5.2.1. SURFACE STRAIN ESTIMATION

The strain experienced due to the magnetic structure depends on the properties of the involved layers, such as thickness, Youngs modulus, and the curvature of the rolled structure. The cross-section of a bilayer magnetic and polyimide film with the neutral axis is depicted in Figure **5.7**. The neutral axis is a cross-sectional axis where there is no bending strain across the bilayer. The distances d_{PI} and d_{Py} in Figure **5.7**a represent the distance from the neutral axis of the bilayer structure to the centroid of polyimide and permalloy films, respectively. Polyimide film and permalloy film thicknesses are 1000 nm and 100 nm, respectively. Therefore,

$$d_{\mathrm{PI}} + d_{\mathrm{Py}} \;=\; 550\ \mathrm{nm} \tag{5.3}$$

Stress equilibrium, that defines the neutral axis, is given as,

$$Y_{\mathrm{PI}} \cdot d_{\mathrm{PI}} \cdot A_{\mathrm{PI}} - Y_{\mathrm{Py}} \cdot d_{\mathrm{Py}} \cdot A_{\mathrm{Py}} \;=\; 0 \tag{5.4}$$

where Y_{PI} and Y_{Py} represent the Young's modulus of PI nad Py, and and $A_{\mathrm{PI}} = A_{\mathrm{Py}} = \mathrm{A}$ is the cross- sectional area. With the Eq (5.4) and the parameters Y_{PI} = 3.2 GPa and Y_{Py} = 96.4 GPa,

$$\begin{aligned} d_{\mathrm{Py}} &= h \\ &= 137 \end{aligned} \tag{5.5}$$

This means that the neutral axis sits 137 nm below the center of the Permalloy film, causing tensile and compressive strains in the rolled-down (Figure **5.7**b) and rolled-up (Figure **5.7**c) states, respectively.

The bending strain is then determined using the formula,[133]

$$\varepsilon \;=\; \pm {}^{h}/_{R} \tag{5.6}$$

where R is the tube's radius. This results in 0.43 % tensile strain and 0.27 % compressive strain for rolled-down and rolled-up structures with bending radii of 32 µm (Figure **5.6**b) and 50 µm, respectively. For two further rolled-down tubes with a radius of curvature of 57.5 µm and 79.5 µm, respectively, the tensile strains are estimated to be 0.24 % and 0.17 %.

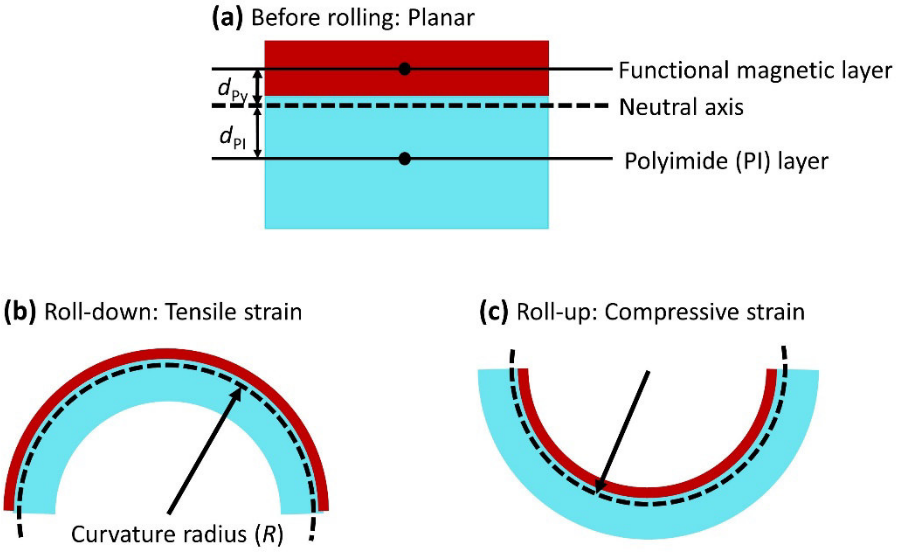
(a) Before rolling: Planar
d_{Py}
d_{PI}
Functional magnetic layer
Neutral axis
Polyimide (PI) layer
(b) Roll-down: Tensile strain
Curvature radius (R)
(c) Roll-up: Compressive strain

Figure 5.7: Schematic depiction of the neutral axis and cross-section of the functional magnetic layer deposited on top of the polyimide film: (a) before rolling. After **(b)** rolling down, and **(c)** rolling up.

5.2.2. QUANTIFICATION OF STRAIN-INDUCED ANISOTROPY

AMR measurements for three rolled-down Py membranes (Figure **5.8**a) have been analyzed for H_{sat} and the uniaxial anisotropy energy K_{u} was calculated via Eq (5.2) using the experimentally measured saturation magnetization, $M_{\mathrm{s}} = 0.69 \times 10^{6}$ A.m^{-1}.

Figure **5.8**b depicts the relationship between K_{u} and strain for three rolled-down permalloy stripes. The strain in the magnetic stripe was quantified using the Eq (5.6), where h is the distance between the center of the magnetic stripe and the neutral axis of the PI/$Ni_{78}Fe_{22}$ bilayer. The linear relationship demonstrates the expected magnetoelastic behavior given by the following equation:[33]

$$K_{\mathrm{u}} = (3/2)\lambda Y \varepsilon \tag{5.7}$$

with Young's modulus $Y = 96.4$ GPa for Permalloy.[134] The magnetostriction constant (λ) is deduced from the slope of the linear fit and amounts to $(1.41 \pm 0.02)\ 10^{-6}$, which agrees well with the direct measurement of the magnetostriction constant of the alloy $Ni_{78}Fe_{22}$.[35]

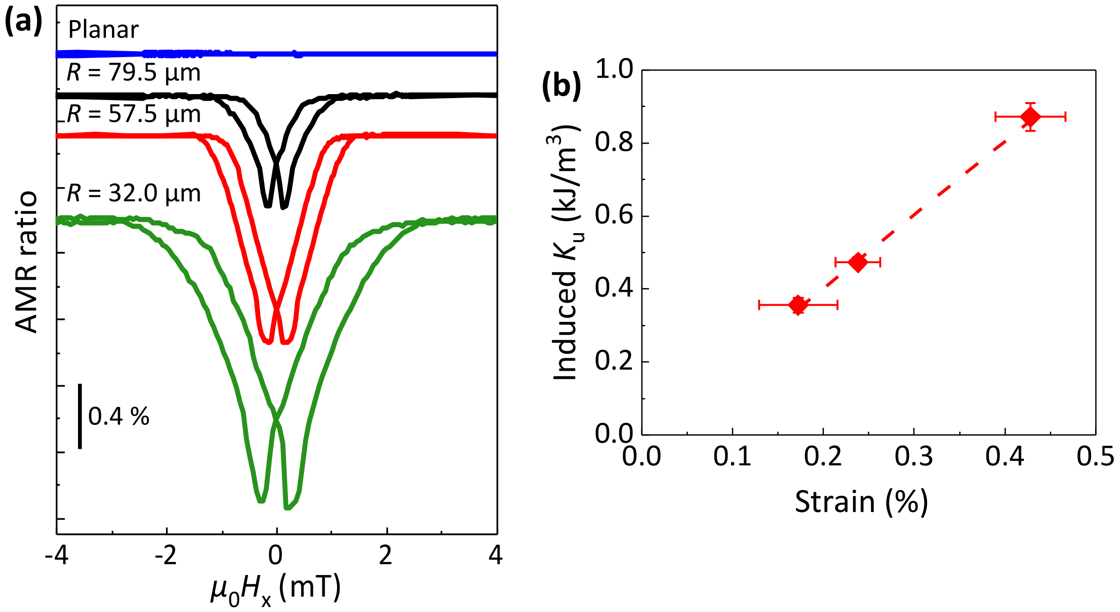

Figure 5.8: Quantification of strain-induced anisotropy: (a) AMR hysteresis of stripes rolled with different curvature. **(b)** Induced anisotropy vs. strain.

5.3. MICRO-MAGNETIC SIMULATIONS

5.3.1. MAGNETIZATION REVERSAL WITH AN AXIAL FIELD

Micromagnetic simulations were used to examine the domain evolution and AMR signals for permalloy stripes in the presence of a field along the stripe (Figures **5.9**a1, a2 and b1, b2). To model the experimentally observed rolled-down and rolled-up stripes, planar stripes were simulated with uniaxial magnetic anisotropy transverse to the stripe (Figure **5.9**a3) and along the stripe (Figure **5.9**b3). Due to limits in computational capacity, the dimensions of the simulated stripes are smaller than those of the stripes experimentally examined. However, the selected dimensions of hundreds of nanometers are large enough to match the experimentally observed magnetization patterns of domains and domain walls. As the smaller lateral dimensions (with constant film thickness) are accompanied by larger demagnetizing factors N_x and N_y in the stripe plane, a larger uniaxial magnetic anisotropy energy density (equivalent field H_k) is necessary to produce a comparable domain configuration. This is why the domain configuration of experimental (L = 550 µm, W = 15 µm, d = 100 nm) and simulated (L = 8 µm, W = 0.8 µm,

d = 100 nm) stripes is the same, even though the magnitude of uniaxial magnetic anisotropy is different by an order of magnitude.

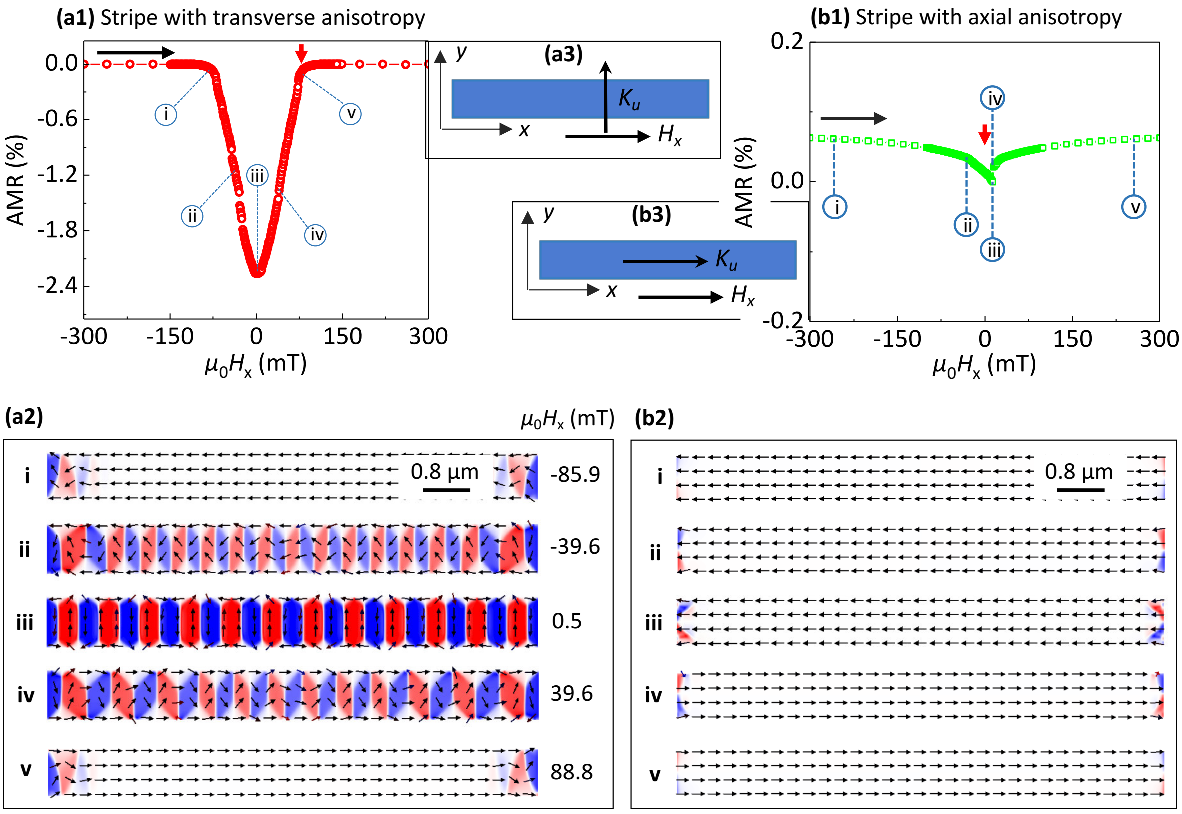

Figure 5.9: Magnetization reversal of planar permalloy stripes in an axial field [with uniaxial magnetic anisotropy magnitude, K_u = 40 kJ.m^{-3}]: AMR hysteresis of a stripe with anisotropy direction **(a1)** transverse **(b1)** to the stripe's long axis. The black arrow within the diagram indicates the direction of the field sweep, while the red arrow indicates the saturation field. **(a2)** and **(b2)** schematic images of the stripe that shows the added anisotropy and field direction. Magnetic domain states were observed at various stages of the field sweep for **(a3)** stripes with transverse anisotropy and **(b3)** stripes with axial anisotropy.

All the features found in the magnetization reversal experiments of rolled stripes were micromagnetically replicated, and the simulations assisted in understanding the experimental results.

In order to determine the relationship between the AMR signal and the induced uniaxial transverse magnetic anisotropy, a series of micromagnetic simulations were conducted for two different stripe sizes and varied transverse uniaxial anisotropies (Figures **5.10**a1 and b1). Different UMAs were introduced to replicate the different rolling diameters of the tube. In every case, the saturation field H_{sat}, which is determined at a 1% decrease in the AMR signal from $R_{\max}$ (normalized to the maximum AMR signal, $R_{\max}$), matched the introduced anisotropy field H_{ani} to within 12%. (Figures **5.10**a2 and b2). The error in the extracted K_{u} is illustrated by the deviation of the plotted data set from the diagonally oriented red line with a slope of one and zero intercept. As a result, a reliable calculation of the strain-induced uniaxial anisotropy constant K_{u} can be made for all rolled-down membranes using simple AMR response analysis and does not need to rely on optical access to the sensor stripe.

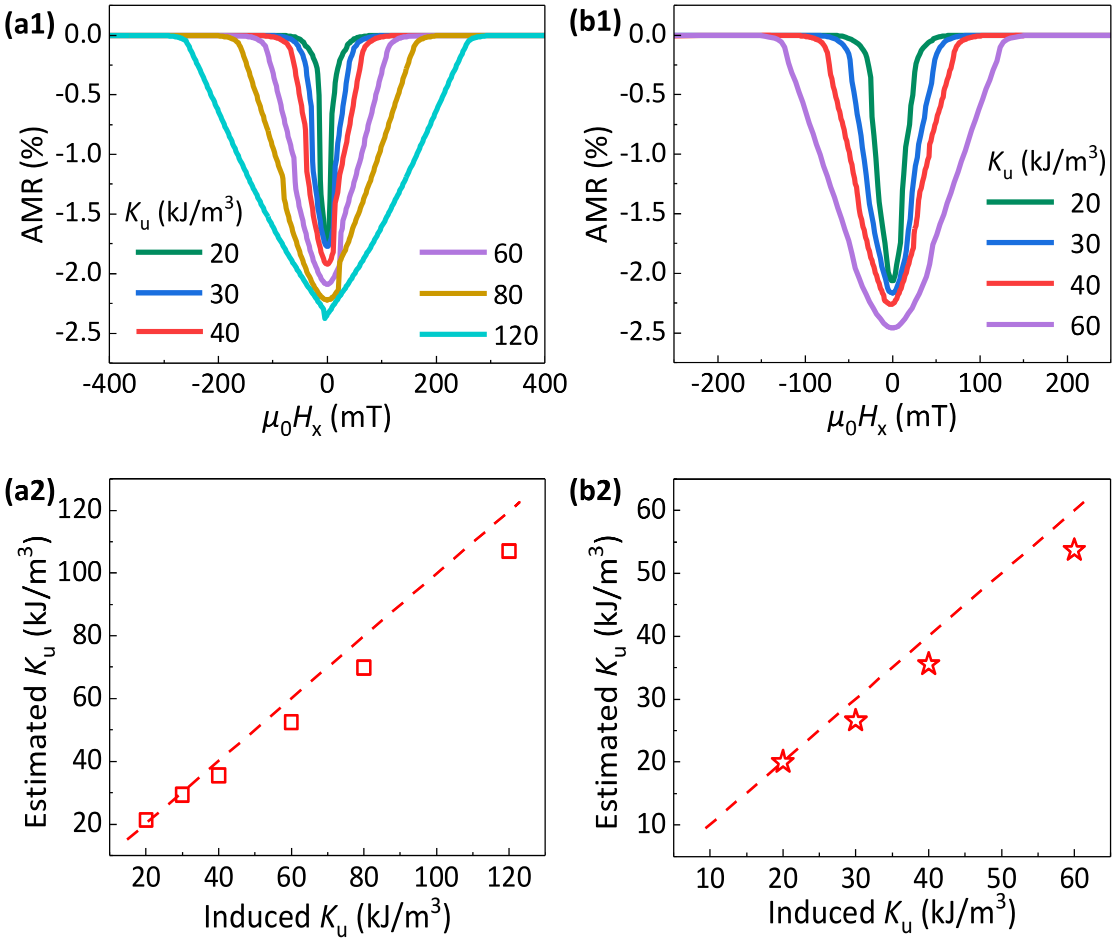

Figure 5.10: Estimation of induced uniaxial transverse magnetic anisotropy using simulated AMR hysteresis in the presence of an axial field: AMR hysteresis (field sweep from the negative to the positive *x*-axis) of permalloy stripes of sizes **(a1)** $L = 4$ µm, $W = 0.4$ µm, $d = 100$ nm, and **(b1)** $L = 8$ µm, $W = 0.8$ µm, $d = 100$ nm at different magnitudes of the introduced UMA (transverse to the stripe). Extracted UMA (K_{u})

compared to the introduced UMA value for stripes **(a2)** L = 4 µm, W = 0.4 µm, d = 100 nm and **(b2)** L = 8 µm, W = 0.8 µm, d = 100nm.

5.3.2. MAGNETIZATION REVERSAL WITH A TRANSVERSE FIELD

To complete the understanding of reversal processes, Figure **5.11** depicts the magnetization reversal of a simulated stripe with uniaxial transverse anisotropy in the presence of a transverse field. Except for the number of observed peaks, the simulated results are comparable to the experimental results presented in section 5.1.3 (Figure **5.5**). As suggested in the explanation of experimental data, the continuous increase in AMR signal with a maximum at zero field is attributed to a continuous increase in m_x (the magnetization component parallel to the long stripe axis and to the sensing current), with a maximum in m_x at zero field. In addition, peaks are observed during the nucleation and annihilation of perpendicular domains. The decrease in AMR upon nucleation of a transverse domain is attributed to the decrease of the x-component of magnetization, as additional transverse domains allow flux closure on a shorter length scale.

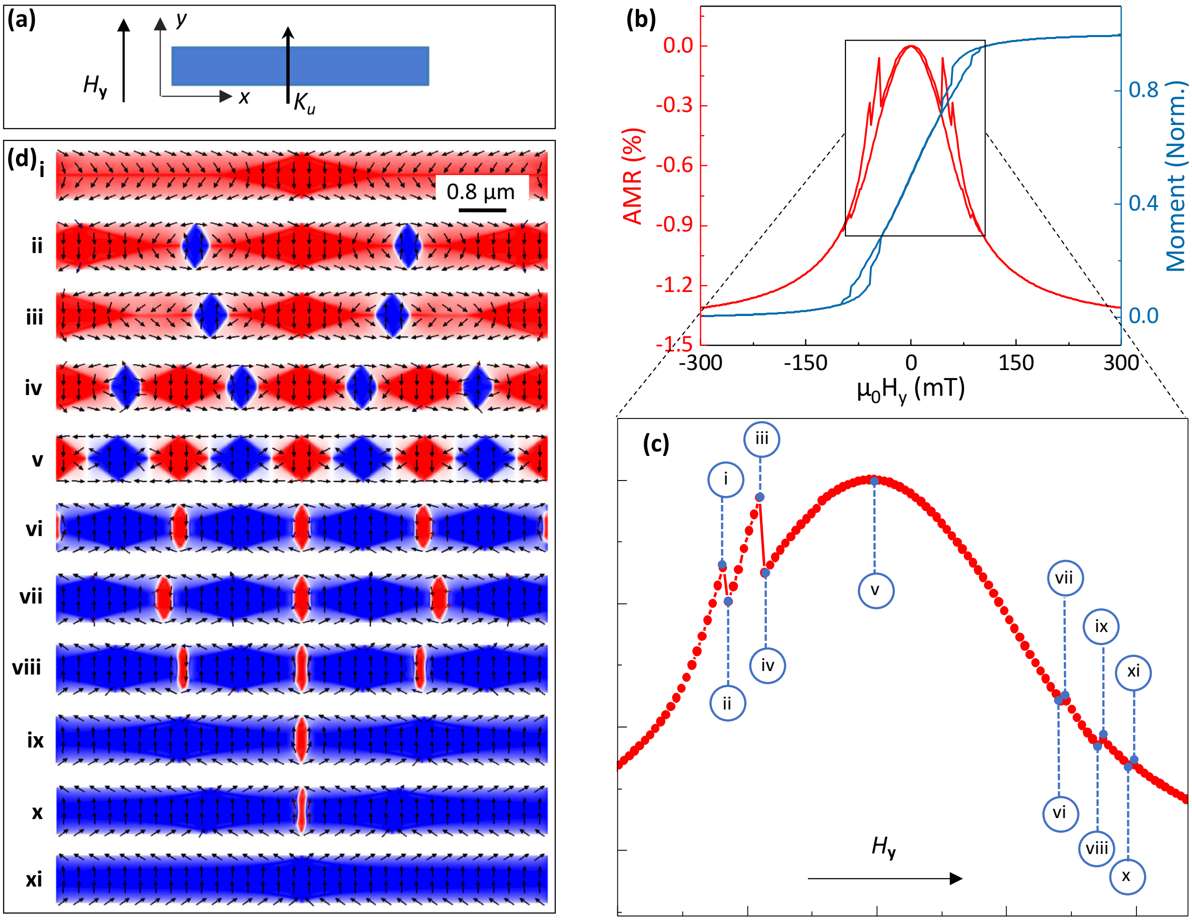

Figure 5.11: Magnetization reversal of planar permalloy stripes [L = 8 µm, W = 0.8 µm, d = 100 nm, with uniaxial transverse magnetic anisotropy magnitude, K_u = 12 kJ.m^{-3}] in a transverse field: (a) A schematic representation of the simulated stripe. **(b)** Magnetic hysteresis and the associated AMR hysteresis. **(c)** A magnified view of the AMR hysteresis for sweeping the field from the negative to the positive *y*-direction. The numbers i, ii, iii...) in the graph represent the AMR values in the respective magnetic domain states i, ii, iii...) shown in **(d).**

5.4. CONCLUSION

Geometrical transformations, such as rolling a 2D ferromagnetic extended film into a 3D cylinder, allow controlling its magnetic properties by generating different magnetic ground states that can emerge from a variety of sources.[66,89,90] Rolled-up magnetic membranes with azimuthal magnetic anisotropy are highly desirable due to a stray-field free flux-closure state and anticipated much higher domain wall velocity (compared to their planar counterparts)[86] which makes these structures promising for applications like impedance-based field sensors[1] and storage devices. Still, a clear recipe for obtaining a desired magnetic anisotropy in a soft ferromagnetic tubular geometry is missing.

Chapter 5 showed a controlled tailoring of rolling-induced uniaxial magnetic anisotropy in $Ni_{78}Fe_{22}$ stripes solely due to strain. The influence of curvature-driven shape anisotropy and exchange in the induced magnetic anisotropy could be disregarded due to the reduced dimensions of magnetic stripes along the circumference and its small curvature, respectively. A self-assembly rolling technology based on a polymeric platform was used to controllably bend/roll microscale magnetic structures fabricated on top of the platform. Consequently, the magnitude of tensile and compressive strains on the magnetic structure was varied by rolling the structures with different diameters in different directions (downwards and upward). The strain-induced magnetic anisotropy of magnetoelastic origin is thus tuned to achieve azimuthal anisotropy of different magnitude. Understanding of magnetization reversal in curved stripes was achieved by probing the magnetization reversal through direct domain observation using magneto-optical Kerr imaging and global anisotropic resistance measurement. This assisted in quantifying the induced azimuthal magnetic anisotropy using electrical (AMR) measurements that could provide magnetic properties of magnetic structures hidden under the 3D polymer architecture.

Chapter 6 DIRECT IMAGING OF NANOSCALE DOMAIN WALL OSCILLATIONS

This chapter introduces a novel imaging method for directly visualizing nanoscale domain wall oscillation trajectory and amplitude. Using the high-resolution capability of magnetic force microscopy (MFM) for imaging purposes, sub-micrometer amplitudes of domain wall oscillation are imaged with nanoscale spatial precision, and measurements are extended for larger amplitudes (above one micrometer) using optical microscopy based on the Kerr effect. For the development of these imaging methods, a 180-degree Néel domain wall in a permalloy Landau structure is used, and the developed methods are implemented to study the DW oscillation dependency on excitation strength, frequency, structure size, and thickness. Micromagnetic simulations are in great accord with the experimental results and contribute to the explanation of the observed dependencies. The selection of a rectangular structure with a size of some ten micrometers guarantees the formation of the desired DW and supports the ease of imaging. The scientific development discussed in this chapter was published in the scientific journal listed below[135] and is reproduced here under the terms of license CC BY 3.0:

"B. Singh, R. Ravishankar, J. A. Otálora, I. Soldatov, R. Schäfer, D. Karnaushenko, V. Neu and O. G. Schmidt, Direct imaging of nanoscale field-driven domain wall oscillations in Landau structures, *Nanoscale*, 14, 13667 (2022)".

6.1. MFM IMAGING

6.1.1. MAGNETIC DOMAIN WALLS

In a demagnetized micron-sized rectangular thin-film element, magnetic domains self-organize themselves to avoid surface charges. As a result, magnetization forms well-known flux-closure patterns, either the Landau pattern (shown in Figure **6.1**a) or the diamond pattern (not shown here). The MFM image illustrated in Figure **6.1**a consists of in-plane magnetization locally aligned parallel to the element edge, separated by four 90-degree DWs and one 180-degree DW. The latter possesses a contrast variation along its length and is additionally divided by horizontal lines known as cross-tie domain walls. Cross-tie DWs are anticipated to form in rectangle-shaped structures with thicknesses between 30 nm and 90 nm. In this stray-field-free configuration, the position of the 180-degree DW follows the principle of minimum magnetic energy, making it suited for harmonic oscillation around this zero-field minimum.

Magnetic domain walls in regions free of cross-tie walls (at positions p and q; solid white lines in Figure **6.1**a) are chosen to perform the dynamic measurement in order to simplify the interpretation of the results. MFM scans in 'slow scan axis' disabled mode (see chapter 4) at the selected y-position produce data with the vertical axis now resembling the time-axis. In the absence of an external magnetic field, the DW position stays unaltered as shown in Figures **6.1**b.i and c.i.

6.1.2. REAL-TIME IMAGING

In the presence of a sinusoidal ac-magnetic field along the y-axis, the domain wall oscillates periodically with the same frequency as the applied field and linearly follows the excitation field. The property of a slowly varying DW in the presence of a low-frequency (0.01 Hz) ac-field enables real-time imaging of the DW oscillation. With a cantilever scan rate of 1.0 Hz (along the fast scan axis, i.e., the x-axis), which is 100 times faster than the oscillation frequency of the domain wall, each scan line in the MFM image records the profile of the quasi-static DW, with the DW position dependent on the momentary field value. Thus, the sinusoidal DW oscillation can be immediately observed in the recorded MFM image with an oscillation period of T = 100 sec (Figure **6.1**b.ii), and the peak-to-peak oscillation amplitude can be easily retrieved from the displacement in the line scans that correspond to opposite return points. As anticipated, the oscillation amplitude x_{amp} (half the peak-to-peak amplitude) varies linearly with the peak ac-field amplitude $\mu_0 H_y$, and will be discussed later.

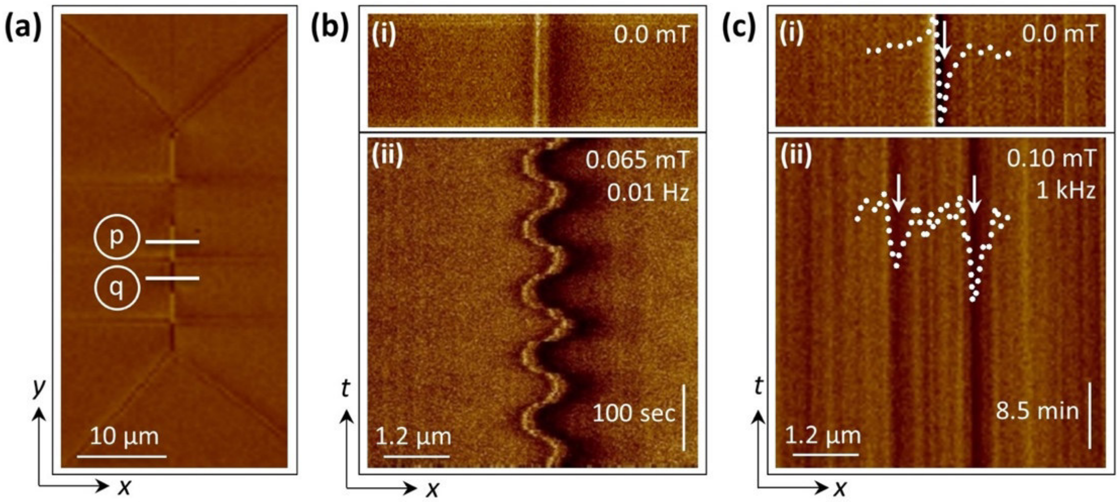

Figure 6.1: Real-time and time-averaged imaging of domain wall oscillations: (a) Demagnetized state of the permalloy rectangle (L = 50 µm, W = 25 µm, d = 50 nm). The white lines at positions p and q represent the lines where real-time (Figure 6.1b) and time-averaged (Figure 6.1c) imaging is performed, respectively, with the 'slow-scan-axis' deactivated. **(b)** Real-time imaging, **i** – static DW, **ii** – oscillating DW. **(c)** Time-averaged imaging, **i** – static DW, **ii** – oscillating DW. In panel c, the white dotted lines represent the static and dynamic DW profiles. Note the different timescales along the time axis in b and c.

6.1.3. TIME-AVERAGED IMAGING

At higher ac-field frequencies (above 0.1 Hz), real-time imaging starts to fail because the DW's periodic motion becomes faster and competes with the cantilever's scan speed. Therefore, time-averaged imaging was developed for frequencies exceeding 100 Hz.

Time-averaged imaging is based on a quantitative evaluation of the time-averaged MFM phase shift signal and its description by the locally varying dwell time function of an oscillating DW. In the case of a static DW (Figure **6.2**a1), the domain wall's spatial position does not change with time, hence the dwell-time, t_D of the DW, i.e., the time spent by the domain wall at a particular position, peaks at the static DW position (Figure **6.2**b1). For a sinusoidally excited DW (Figures **6.2**a2 and a3), the periodicity and waveform of ac excitation strictly define the DW position ($\propto B$) and DW velocity ($\propto dB/dt$). Due to the position-dependent velocity of the DW, the dwell time (Figures **6.2**b2 and b3) is dependent on the momentary position of the DW with respect to its static position.

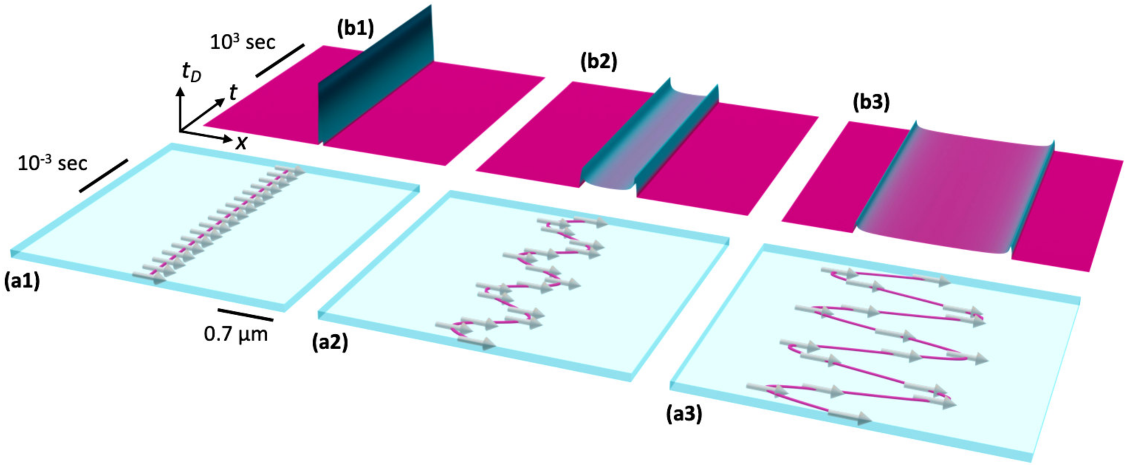

Figure 6.2: Schematic illustration of the time-averaged MFM imaging concept: (a) Schematics of a static and oscillating Néel type domain wall in the position-time (x-t) plane. The Néel type DW center is depicted by the magenta line and magnetic moment vectors parallel to the surface in figures a1 to a3. DW position as a function of time **(a1)** for static and dynamics with amplitudes **(a2)** and **(a3)** of 0.3 µm and 0.76 µm, respectively, at a frequency of 1 kHz. **(b)** Normalized dwell-time t_D for **(b1)** static and oscillating DW with **(b2)** 0.3 µm amplitude and **(b3)** 0.76 µm amplitude. Note the different time scales in panels (a) and (b).

The time-averaged MFM signal of a dynamically oscillating DW (Figure **6.1**c.ii) therefore comprises information regarding the oscillation's trajectory and amplitudes. With a cantilever scan rate of 0.1 Hz (along the fast -scan axis), which is 10^4 times smaller than the DW oscillation frequency (1 kHz), even within the acquisition time of one pixel, the DW performs several periods of motion. Consequently, the MFM tip detects the time-averaged phase change signal proportional to the amount of time the DW is present at that location. Due to position-dependent DW velocities, this dwell time t_D is likewise position-dependent in the case of a sinusoidal DW oscillation. As a result, the longest tip-DW interaction appeared as two darker vertical lines at the return points (or amplitude) of the DW oscillation (Figure **6.1**c.ii). The intensity profile of this measurement (obtained by averaging the line contrast along the time axis) is superimposed as a white dashed line onto the image. The peak positions of the oscillating DW are represented by the two minima in the intensity signal.

This intensity profile is again shown in Figure **6.3**a, along with additional measurements, the oscillation profile at $\mu_0 H_y$ = 0.064 mT (blue dotted line), and at zero excitation field (red dotted line). The static DW signal reveals the normal MFM interaction between the magnetic tip and the DW stray fields. In the presence of a nonzero ac-field strength, the

DW signal first broadens before splitting into two minima. When the amplitude of the excitation is increased further, the peak positions move farther apart, and the minima become shallower. Figure **6.3**b depicts a dynamic MFM picture intensity profile of another rectangle, that initially broadens and then splits into two peaks.

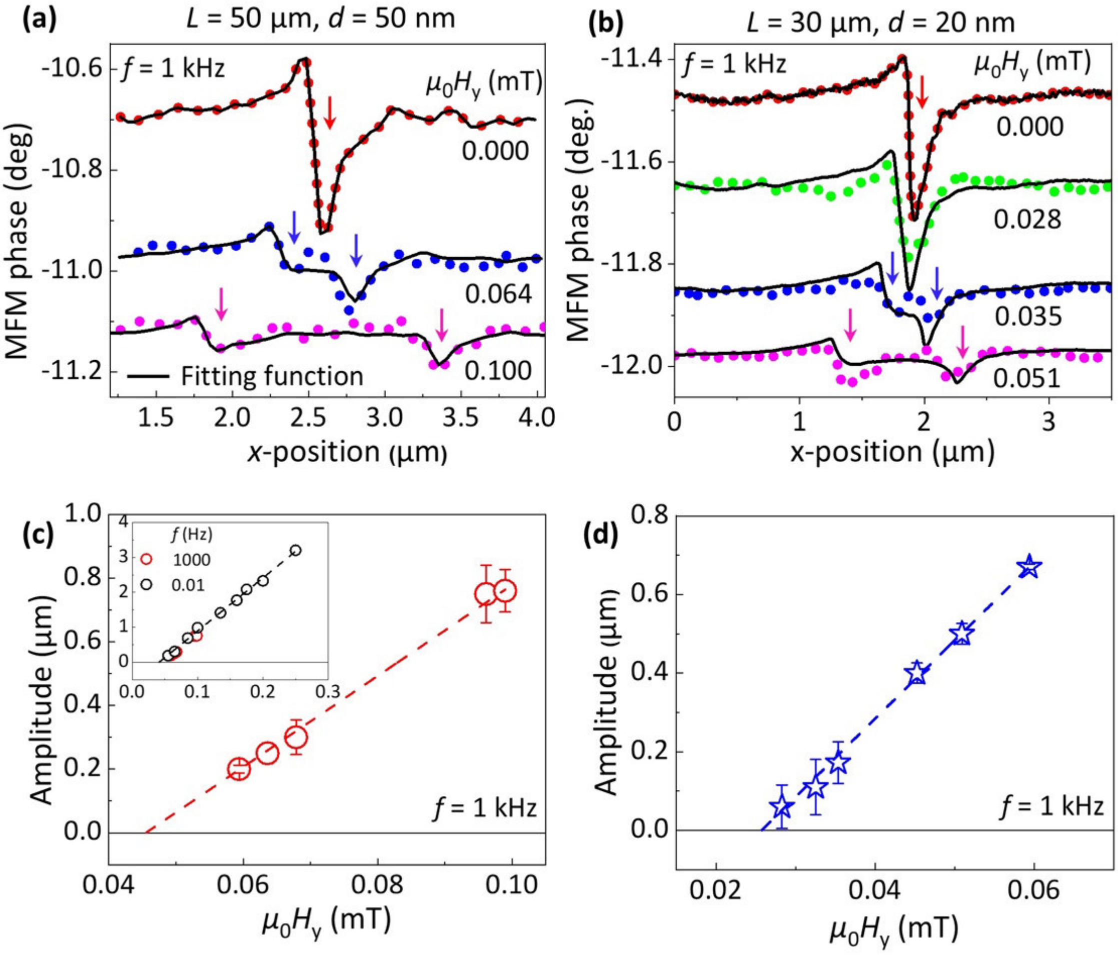

Figure 6.3: Imaging of DW oscillations using MFM: The measured intensity profiles of the static DW and the time-averaged DW oscillating at 1 kHz (dotted lines) for the rectangles with dimensions **(a)** L = 50 μm, W = 25μm, d = 50 nm, and **(b)** L = 30 μm, W = 15 μm, d = 20 nm. The solid lines represent the analytical function that was used to fit the experimental data. The arrows represent the fixed position of the DW at zero fields and the two extreme positions of an oscillating DW. DW oscillation amplitudes vs. field amplitude for rectangle of dimensions **(c)** L = 50 μm, W = 25μm, d = 50 nm, and **(d)** L = 30 μm, W = 15 μm, d = 20 nm. The inset graph in Figure 6.4c depicts the oscillation amplitudes for slow (0.01 Hz, imaged in real-time) and high (1 kHz) frequencies with axis labels and units as used in the main panel.

A full quantitative understanding of these dynamic MFM intensity profiles is based on the measured intensity profile of a static DW and its modification by the dwell time function of a given oscillation. DW oscillations are sketched in Figure **6.4**a in a *x*-*t*-diagram and are considered to be purely periodic and sinusoidal. This assumption was motivated by the periodic and sinusoidal field excitation. The DW contributes to the signal at a certain position x_i along the scan line when it resides at this position x_i within the pixel size Δx (resolution of static and dynamic MFM images). The effect on the dwell time is depicted in Figure **6.4**a for two positions x_1 and x_2. At position x_1, close to the return point of the DW, the dwell time is significantly longer, but at x_2, close to the equilibrium position, the fast-moving DW causes the tip to interact with the DW for only a brief period of time during the pixel acquisition time. The dwell time, t_D is expressed as:

$$t_D(x_i) \;=\; \frac{1}{N}\left[\sin^{-1}\left\{\left(x_i+\frac{\Delta x}{2}\right)\Big/ x_{\mathrm{amp}}\right\} - \sin^{-1}\left\{\left(x_i-\frac{\Delta x}{2}\right)\Big/ x_{\mathrm{amp}}\right\}\right] \qquad (6.1a)$$

where x_{amp} is the peak amplitude of the DW oscillation, and N is the normalization factor (period of oscillation, T), which can be written as follows,

$$N \;=\; \sum_{i=-(n-1)}^{(n-1)}\left[\sin^{-1}\left\{\left(x_i+\frac{\Delta x}{2}\right)\Big/ x_{\mathrm{amp}}\right\} - \sin^{-1}\left\{\left(x_i-\frac{\Delta x}{2}\right)\Big/ x_{\mathrm{amp}}\right\}\right], \qquad (6.1b)$$

Here, i runs from $-(n-1)$ to $(n-1)$ generating a total $2n-1$ of dwell time points at positions, $x_i = (i \times \Delta x)$. n is the number of lines utilized in MFM imaging, $x_{\mathrm{scan-size}} = n \cdot \Delta x$ is the width of the MFM image, and x_{amp} is the peak amplitude of DW oscillations. This definition guarantees that t_D is provided for a data set twice as large as the MFM intensity profile and thus allows convolution of the two discrete data sets.

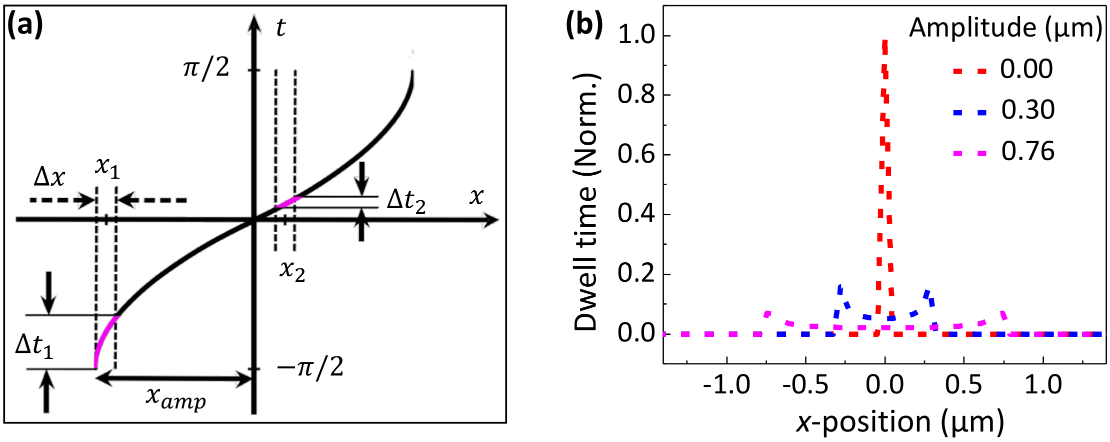

Figure 6.4: Mathematical model for dwell time function for the sinusoidal motion of DW: (a) A sketch of sinusoidal domain wall oscillation depicting the amplitude of the dwell time (magenta color region) at two distinct pixel positions. **(b)** The dwell time

determined for sinusoidally oscillating DW with varying peak amplitudes (the 3D view is shown in Figure **6.2**b).

Figure **6.4**b depicts the normalized dwell time data computed using Eq (6.1a) for a static DW and for oscillating DWs with two distinct amplitudes (0.30 µm and 0.76 µm). For the static DW, the dwell time peaks at the DW position, but for oscillating DW, the dwell time is dispersed over the region of DW motion and hence peaks at the two return points of the oscillation.

Due to the fact that the MFM contrast of a magnetic DW is necessarily widened by the typical tip – stray field interaction,[57] the MFM signal recorded of the oscillating DW is the convolution[136] of the static MFM profile with the aforementioned normalized dwell time function.

$$\mathrm{MFM}_{\mathrm{ac}}(x) \;=\; \mathrm{MFM}_{\mathrm{static}}(x) \otimes t_{\mathrm{D}}\big(x; x_{\mathrm{amp}}\big), \tag{6.2a}$$

which for the two discrete data sets reads,

$$\mathrm{MFM}_{\mathrm{ac}}(x_i') \;=\; \textstyle\sum_{x_i} \mathrm{MFM}_{\mathrm{static}}(x_i)\, t_{\mathrm{D}}(x_i' - x_i), \tag{6.2b}$$

Since the tip-DW interaction (static DW profile) was used in the convolution method to generate the dynamic MFM signal, it is important that all the measurement parameters during dynamic DW imaging, such as the magnetic properties of the MFM tip and the scanning parameters (scan rate, number of pixels per scan line, lift height), should be identical to those used during static DW imaging.

This model now allows a mathematical description of the measured data displayed in Figure **6.3**a and b. The solid black lines in Figures **6.3**a and b represent the convolved signals, using Eq (6.2b), which are based on the measured static MFM profile and include just the oscillation amplitude as a free fitting parameter.

All experimental features are well described by the model (Figure **6.3**a), confirming the correct assumptions of periodicity, sinusoidal DW movement, and the ansatz of a time-averaged phase shift signal. As depicted in Figure **6.3**b, for DW oscillations up to an amplitude of about 100 nm, the peak does not split but expands relative to the signal in the static domain, and only as the field amplitude increased, it did split into two minima. The fitting technique retrieves the smallest peak oscillation amplitude, 60 nm in size. Nevertheless, the visible deviation of the fitting functions from the measured MFM signal in Figure **6.3**b indicates either a deviation of the DW oscillation from an ideal sinusoidal wall oscillation (possible causes include an asymmetric DW oscillation due to inhomogeneities in the pinning landscape) or, slight changes in the magnetic properties of the MFM tip between scanning static and dynamic measurements. The oscillation amplitude x_{amp} increased linearly as a function of $\mu_0 H_y$ (Figures **6.3**c and d) with good agreement between the quasi-static (inset in Figure **6.3**c) and dynamic DW amplitudes despite the largely different excitation frequencies. Besides confirming the linear increase of DW oscillation amplitude with $\mu_0 H_y$, these measurements in the small field regime allow a precise determination of the depinning field H_p from the intercept with the abscissa. Below a value of $\mu_0 H_\text{p}$ = 0.05 mT (rectangle, L = 50 um, d = 50 nm), the 180-degree DW movement is suppressed due to pinning, which is believed to be increased by pinning of the associated Blochlines and cross-tie walls. A characteristic of the time-averaged signal for sinusoidal oscillations is that the signal strength drops constantly as the oscillation amplitude increases. The time averaged MFM method is therefore most effective under the following conditions:

(i). Study of oscillation amplitudes at or below the micrometer range, where also the high lateral resolution MFM comes as a benefit.

(ii). Imaging of DW with sufficient MFM signal in the static regime to cultivate a high signal-to-noise ratio.

(iii). Easy wall movement and low pinning to guarantee an unperturbed response of the DW to the applied ac field.

180-degree DWs in Landau domain configuration locate itself at the lowest energy in a magnetic energy well (discussed in section 6.4). Low anisotropy of permalloy material ensures linear DW motion in response to external excitation due to low DW pinning. As a result, appropriate ac-excitation can controllably oscillate the DW around the minimum energy position. Moreover, stray-fields produced by internal charges in the Neel type DWs in thin rectangles provide significant MFM signal of the DW oscillations thus making thin micron-sized permalloy rectangles suited for the development of the time-averaged MFM imaging technique.

6.2. TIME-AVERAGED KERR IMAGING

The concept of time-averaged magnetic imaging can also be applied to Kerr microscopy, which offers an easy characterization of magnetic domains on a length scale of some tenths of micrometers and above. After the ac-field demagnetizing procedure, the Landau pattern obtained at zero-field is depicted in Figure **6.5**a. By selecting a vertical sensitivity orientation, bright and dark regions correspond to magnetic domains oriented parallel and antiparallel to the long axis. Cross-tie walls give additional weak contrast in this 50 nm thick rectangle. To examine ac-field-excited DW oscillations, the zero-field image characterized by the four-domain state (Figure **6.5**a) was used as a reference and subtracted from a live image (Figure **6.5**b). Without application of external fields, the blank difference image (Figure **6.5**b) confirms the unchanged domain configuration. An external ac-field applied along the long axis of the rectangle drives the DW in phase with the applied excitation field, and the DW areas influenced by the DW dynamics appears as regions of dark and bright contrast as shown in Figure **6.5**c. Figure **6.5**d depicts the intensity profile of dynamic Kerr pictures in the presence of varying magnetic field strengths (and constant frequency). Using the following mathematical model, these intensity profiles can be explained. The intensity at a particular location along the x-axis is proportional to the average time the magnetic domain is expanded beyond that location during the DW oscillation. This is depicted in Figure **6.5**e, where the sinusoidal DW movement is plotted in a time-position diagram, and the respective time for two different positions x_1 and x_2 is depicted by Δt_1 and Δt_2, respectively. Clearly, at position x_1 close to the equilibrium ($x = 0$), the DW spends a longer period Δt_1 beyond x_1, whereas at position x_2 (close to the return point), the DW only enters the region at and beyond x_2 for a brief time interval Δt_2 where it contributes to the measured difference image. Apart from being determined by the length of the time interval, the intensity changes sign also with the sign of x. In addition, due to the spatial extension of the DW signal (provided by the optical resolution, Δx), the intensity is given by the integral across the resolution width of the sign-weighted dwell time. Thus, the intensity is described by

$$I_{\mathrm{Kerr}}(x) = C.\int_a^b [(\pi/2)\cdot \mathrm{sign}(x) - \mathrm{Sin}^{-1}(x - x_{\mathrm{offset}}/x_{\mathrm{amp}})]dx \qquad (6.3)$$

where sign(x) is the sign function, C is a scaling factor, and x_{amp} is the DW oscillation peak amplitude. The integration boundaries depend on the DW position x and are defined as,

$$a = \max(x - \Delta x/2\,, -x_{\mathrm{amp}})$$

$$b = \min(x + \Delta x/2\,, x_{\mathrm{amp}})$$

The above model contains the lateral resolution of the Kerr imaging (Δx) and a possible offset in DW oscillation (x_{offset}) to describe the observed dynamic Kerr signal. The introduction of Δx in the model is necessary to explain the finite slope of the linear intensity region around $x = 0$. A value of $\Delta x = 115$ nm is in agreement with the utmost optical resolution obtained with a 100X objective. The introduction of x_{offset} explains the asymmetry in the intensity profiles.

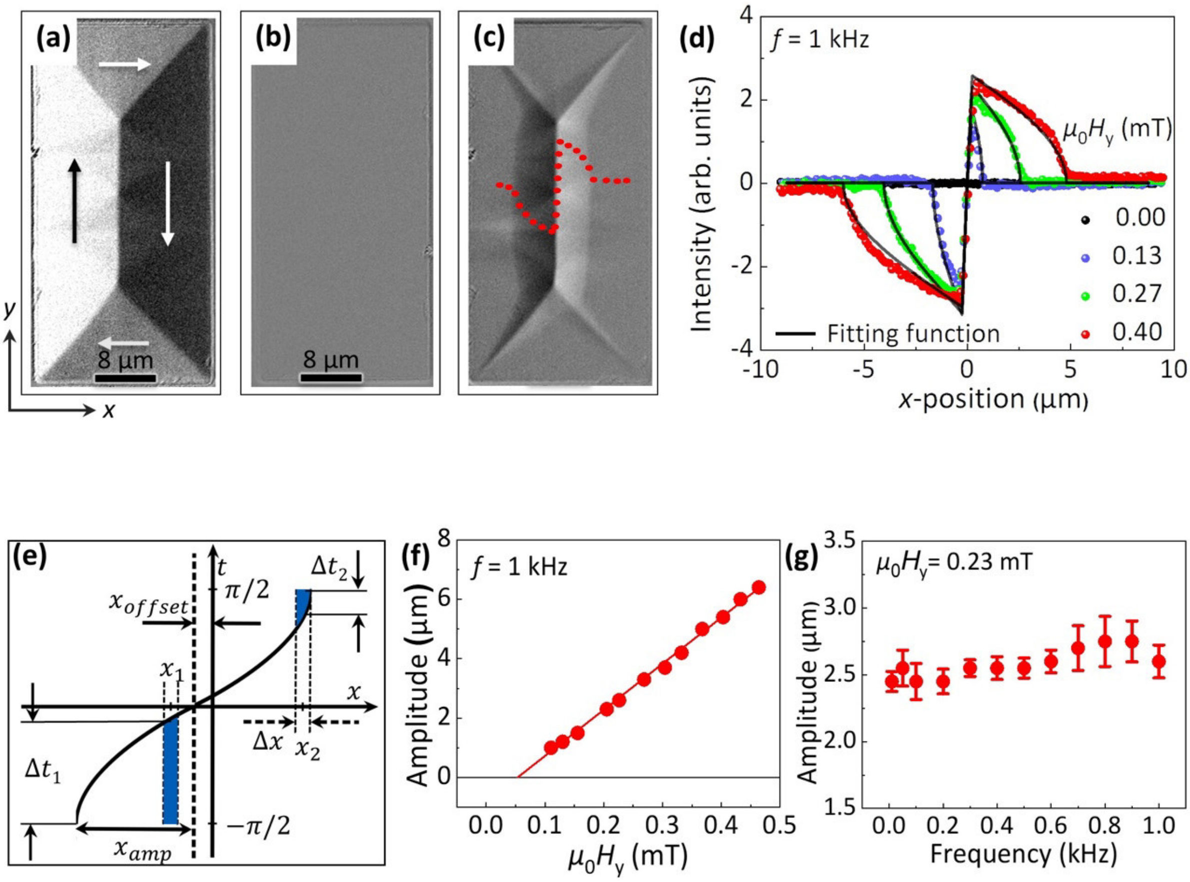

Figure 6.5: Time-averaged Kerr imaging of DW oscillation: (a) Rectangle (L = 50 µm, W = 25 µm, d = 50 nm) in ac-demagnetized state. **(b)** After subtracting the background (Figure 6.6a). **(c)** Image with the background subtracted in the presence of an ac-field. The red dashed line illustrates the intensity profile (line scan) of the oscillating 180-degree domain wall. **(d)** Measured intensity profile of dynamically averaged difference images at 1 kHz for various DW oscillation amplitudes (colored symbols). Based on the concept depicted in, the solid black lines represent the experimental data fitting functions **(e)**. **(f)** DW oscillation amplitude vs field amplitude at a constant excitation frequency. **(g)** The amplitude of DW oscillation as a function of excitation frequency at a fixed field amplitude.

The intensity profiles derived according to Eq (6.3) are fitted to the experimental data by adjusting the oscillation amplitude x_{amp} and x_{offset} keeping C and Δx constant for a given set of experimental data. For the data in Figure **6.5**d, $x_{\text{offset}} = 0.5$ µm is obtained irrespective of oscillation amplitude. One probable explanation for this asymmetry is that the 180-degree DW in the zero-field domain free difference image was not exactly in the middle of the rectangle's width since the dark domain is slightly larger than the bright domain. The extremely close correlation between the observed and the modeled signal validates the sinusoidal DW motion and gives a robust evaluation of x_{amp}. Figures **6.5**f and g summarize the results of various field amplitudes and excitation frequencies, respectively. In the examined frequency range of 100 Hz to 1 kHz, the DW oscillation amplitude increases linearly with the field amplitude $\mu_0 H_y$ but exhibits no significant dependence (within the error bars) on the excitation frequency. Regarding magneto-optical signal detection, the time-averaged measurement method imposes no upper limit on the DW oscillation amplitude and frequency; however, the power supply and the inductance of the field coils restricted the present experiments to excitation frequencies of maximum 1 kHz.

6.3. INFLUENCE OF STRUCTURE SIZE AND THICKNESS

To gain a better understanding of the DW dynamics in permalloy rectangles, two additional rectangles of varying dimensions were fabricated (Figure **6.7**a) and investigated using time averaged MFM and Kerr imaging. In comparison to the previously discussed structure (rectangle 1) with an edge length of 50 µm and a permalloy thickness of 50 nm, rectangle 2 has a film thickness of 20 nm. Rectangle 3 (partially discussed in Figures **6.4**b and d) maintains a thickness of 20 nm while its edge length is lowered to L = 30 µm. After ac-demagnetization, rectangles 2 and 3 exhibit the Landau ground state with 180-degree domain walls, but without crossties, consistent with the decreased thickness (microscopic images are shown in Figures **6.7**b and c).[31] It is found that the geometry has a decisive effect on the oscillation amplitude, with a strong increase in amplitude as film thickness decreases (compare rectangles 1 and 2) and a strong decrease in amplitude as the planar dimensions are decreased (compare rectangles 2 and 3) as demonstrated in Figure **6.7**d. The depinning fields for thin rectangles 2 and 3 are comparable to each other ($\mu_0 H_{\mathrm{p}}$ = 0.02 mT) but are smaller than for rectangle 1 ($\mu_0 H_{\mathrm{p}}$ = 0.05 mT), supporting the idea of the cross-tie walls as additional source of pinning. Concerning dynamic behavior, the oscillation amplitude is independent of excitation frequency up to 1 kHz, as measured by MFM and Kerr microscopy for rectangles 1 and 3 at two distinct excitation field amplitudes $\mu_0 H_y$ (Figure **6.7**e).

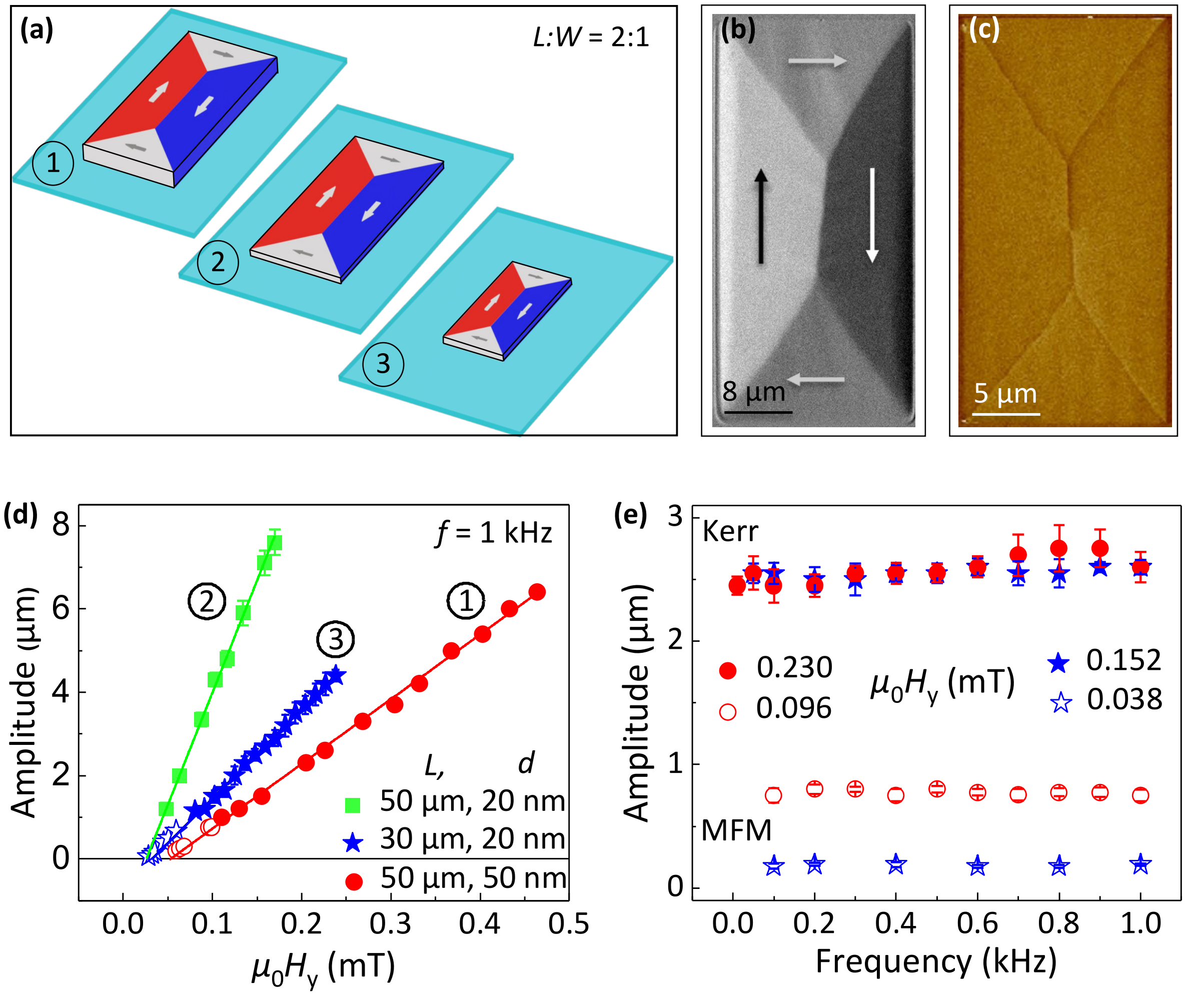

Figure 6.6: Oscillation amplitude dependency on structure size and thickness: (a) Schematics of rectangles of various sizes labeled 1 to 3 (**1.** L = 50 µm, W = 25 µm, d = 50 nm; **2.** L = 50 µm, W = 25 µm, d = 20 nm; **3.** L = 30 µm, W =15 µm, d =20 nm). **(b)** Cross-tie-free DW configuration in rectangle 2 observed by Kerr microscopy. **(c)** MFM image of cross-tie free DW in rectangle 3. **(d)** Oscillation amplitudes as a function of field amplitude for rectangles 1, 2, and 3 at a constant frequency of 1 kHz. **(e)** Oscillation amplitude versus excitation frequency for rectangles 1 and 3 at constant excitation amplitude. MFM and Kerr' data are represented by open and solid symbols, respectively.

Even at f_{ac} = 1 kHz, the data demonstrates that the DW immediately follows the excitation field. Studies utilizing Kerr susceptometry on Co$_2$MnGe[137] and Co[50] stripes revealed that the DW oscillation amplitude is dependent on both excitation amplitude and frequency. The DW oscillation amplitude varies with excitation frequency for a fixed excitation amplitude. At a field value close to the coercive field of the magnetic structure, for instance, the DW oscillation amplitude begins to decrease above a cutoff frequency (which is between 28 Hz and 38 Hz and 1500 Hz to 3700 Hz, depending on the field value applied in Co_2MnGe and Co stripes, respectively) and approaches zero as the excitation frequency is further increased. The cutoff frequency is proportional to the DW mobility, which the experiment reveals to be 11 m·[sec]$^{-1}$·[mT]$^{-1}$ for the 60 nm thick Co_2MnGe film and 150 m·[sec]$^{-1}$·[mT]$^{-1}$ for the 40 nm thick Co film. These results show that in these 50 nm thick permalloy structures, for which a DW mobility of around 100 m·[sec]$^{-1}$·[mT]$^{-1}$ is anticipated,[138,139] the DW amplitudes up to 1 kHz excitation frequency should not decline with frequency, in agreement with the experimental findings of this dissertation. In addition, it was determined that the DW dynamics in permalloy rectangles in the applied field and frequency range occur in the flow regime.

A simple reasoning for the increasing amplitude with increasing edge length L is as follows: regardless of the size of the structure, a given field $\mu_0 H_y$ applied to a permalloy rectangle will result in about the same normalized net magnetization. m_y. Thus, the wider structure ($W = L/2$) will permit a larger absolute DW movement. This, however, cannot account for the increase in x_{amp} when film thickness d decreases. A comprehensive explanation must consider the actual magnetization configuration and related energy terms, including demagnetization energy and exchange energy contained in the field-dependent domain pattern and domain walls.

6.4. MICROMAGNETIC SIMULATIONS

6.4.1. INFLUENCE OF STRUCTURE SIZE AND THICKNESS

Numerical micromagnetic simulations were performed to mimic the quasi-static DW dynamics in permalloy rectangles. To examine the effect of structural size and thickness on DW dynamics, simulations were performed beginning with rectangles almost 10 times smaller (due to limits in computational capacity) and ending with the dimensions of the smallest experimentally realized rectangle (rectangle 3). The dimensions chosen for simulation were sufficiently large to mimic the experimentally observed domain arrangement, with the exception of the cross-tie walls, which were absent in even the thickest (50 nm) rectangle simulated.

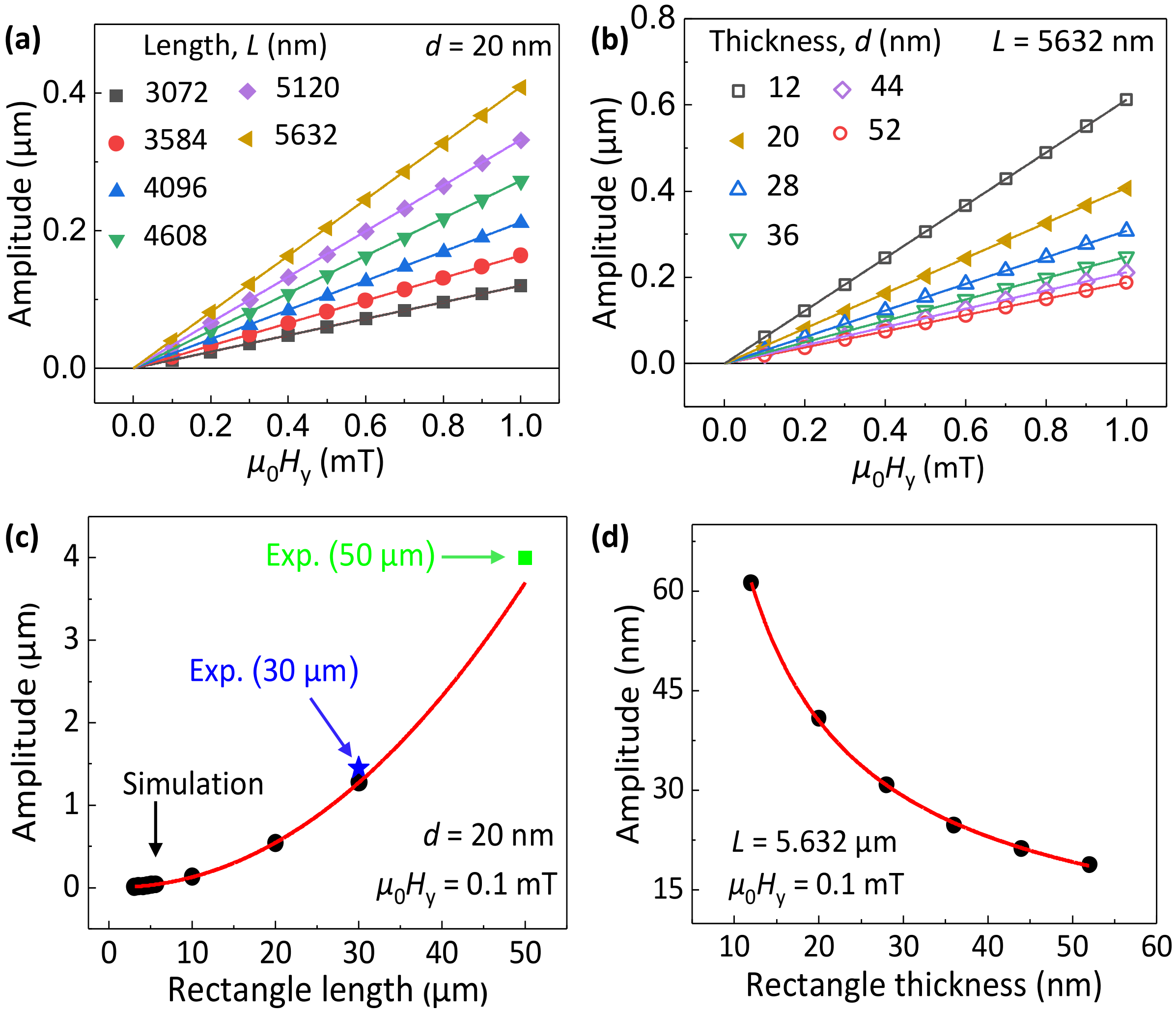

Figure 6.7: Oscillation amplitude dependency on structure size and thickness: DW oscillation amplitude versus field amplitude for rectangles of **(a)** various sizes having a constant thickness, and **(b)** various thicknesses for constant size. DW oscillation amplitudes at constant excitation amplitude for **(c)** various rectangle sizes while maintaining thickness, and **(d)** various rectangle thicknesses while maintaining size. All rectangles possess an aspect ratio L:W = 2:1 as used experimentally.

For the purpose of analyzing DW dynamics, magnetic domain configurations were produced by applying fields (μ_0H_y) up to 1 mT in increments of 0.1 mT, and the DW displacement was examined. Experiments revealed that when $m_y \leq 0.5$, the amplitude (displacement) increases linearly with μ_0H_y (as depicted in Figures **6.7**a and b for rectangles of varying sizes and thicknesses). The DW displacement at a constant field μ_0H_y = 0.1 mT is plotted in Figures **6.7**c and d as a function of the edge length L, and thickness d, respectively. In Figures **6.7**a and c, simulations for permalloy structures with 20 nm thickness and edge lengths L ranging from 3.7 µm to 30 µm are summarized, and the displacement (amplitude) rises with L, as observed experimentally. The data can be represented by a power law with the exponent p equal to 2.09. Due to restricted computer memory, simulations for L = 50 µm were not possible; instead, the fitted power law was extrapolated to 50 µm length (red solid line in Figure **6.7**c). In Figures **6.7**b and d, simulations for rectangles of constant size (L = 5.6 µm) but varying thicknesses between 12 and 52 nm are summarized. As in the experimental observations, the DW displacement for a fixed field decreases with increasing thickness. The data can be represented by an inverse power function, with the exponent p equal to 0.81. Besides this qualitative comparison, which verifies the observed dependency on the pattern geometry, the simulations depicted in Figure **6.7**a also offer a direct quantitative comparison with the experiment. The experimentally obtained dynamic amplitudes at f = 1 kHz for the two 20 nm thick rectangles with L = 30 µm and 50 µm are included in the graph and correspond well to the static simulations (maximum discrepancy of 7.5%). This again confirms that the DW immediately follows the externally applied field and that, with the exception of the minor effect of the depinning field, the DW displacement in this frequency range is unaffected by the microstructural features of the material. This is undoubtedly a result of the 'self-sustaining' domain configuration of the Landau pattern, in which the equilibrium position of the DW in a given field is decided purely by the gain in Zeeman energy versus the costs of an increased exchange and demagnetizing energy. When a good approximation of the two latter energy terms is known, a simple energy approach provides a complete description of the investigated domain structure.

In order to accomplish this, the sum of demagnetizing energy and exchange energy was retrieved from micromagnetic simulations as a function of m_y for modest external fields near zero. In every simulation, the energy density increases quadratically with m_y (Figures **6.8**a and b), which can be phrased as

$$E_{\mathrm{ex+demag}} = c_0 + c \cdot m_y^2 \tag{6.4}$$

where the stiffness parameter c measures the restoring force on the DW when displaced from its equilibrium position at m_y = 0.

The stiffness parameter c exhibits a hyperbolic decrease as a function of the edge length, L, ($c \propto L^{-1.03}$), as depicted in Figure **6.8**c. Figure **6.8**d depicts the analogous analysis for variable film thickness, which yields a stiffness parameter that varies roughly linearly with the thickness ($c \propto d^{0.84}$).

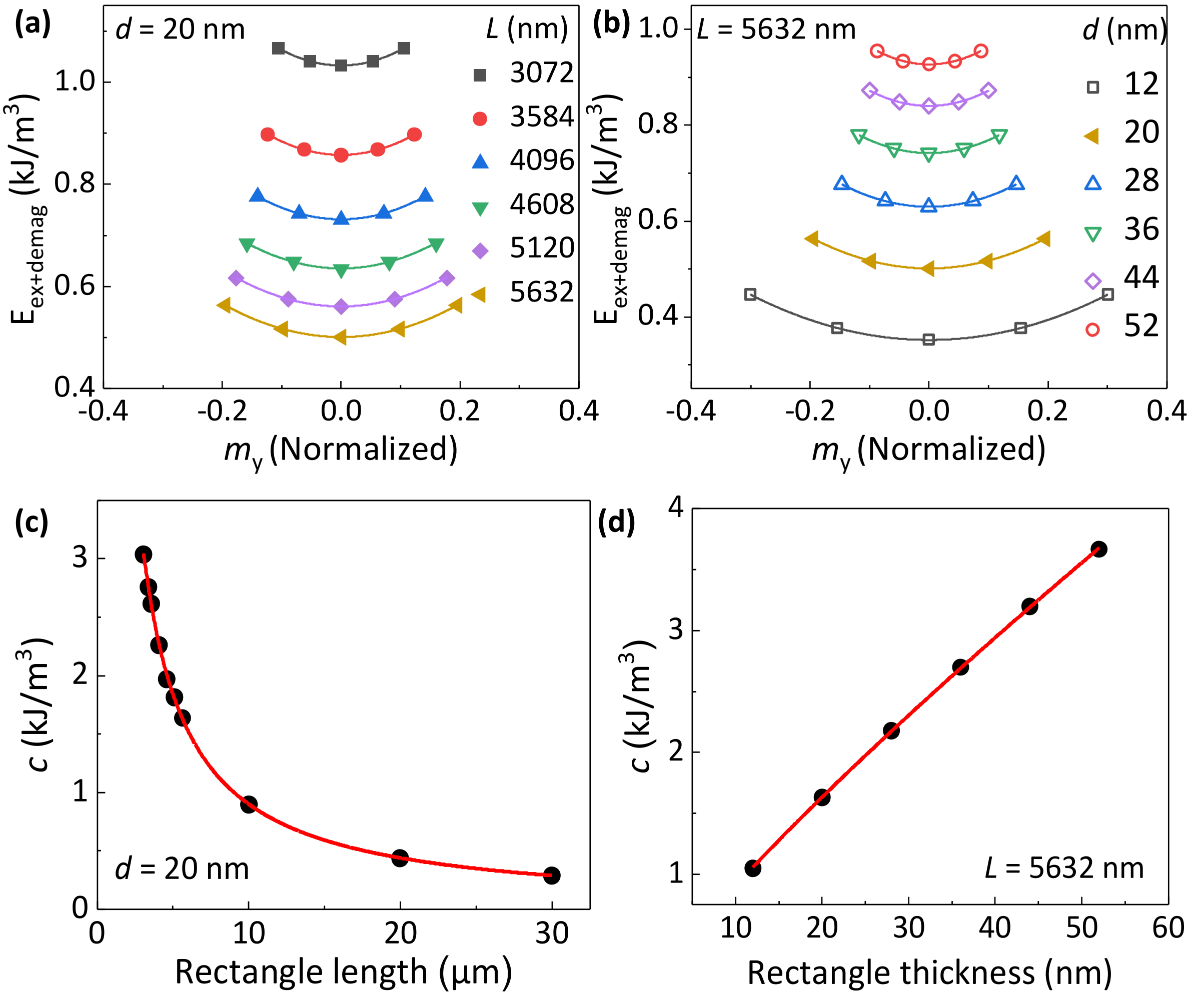

Figure 6.8: Influence of energy (magnetostatic and exchange) densities on DW displacement: The relationship between energy density and net magnetization m_y in rectangles [m_y originating from DW displacement from its equilibrium position ($m_y = 0$)], **(a)** of varied rectangular sizes with constant thickness, and **(b)** of varying thicknesses with constant size. Stiffness parameter derived from the parabolic fit of energy density plots **(c)** shown in Figure 6.9a and **(d)** shown in Figure 6.9b.

The equilibrium DW position x_{amp} can then be calculated using the minimal total energy density,

$$E_{tot} \;=\; E_{\text{ex}} + E_{demag} + E_{Zeeman} \tag{6.5}$$

with respect to m_y via,

$$\partial E_{tot} \big/ \partial m_y \;= 0 \tag{6.6}$$

applying,

$$E_{\text{Zeeman}} \;=\; -\mu_0 \cdot M_s \cdot H \cdot m_y \tag{6.7}$$

and,

$$m_y \;=\; \beta \cdot \left({}^{2\,\cdot\, x_{\mathrm{amp}}}\!/_{W}\right) = \beta \cdot \left({}^{4\,\cdot\, x_{\mathrm{amp}}}\!/_{L}\right) \tag{6.8}$$

Eq (6.8) relies on a rigid, constant-length, 180-degree DW that is valid for moderate amplitudes. This equation was derived considering Figure **6.9** for zero and nonzero DW displacement and therefore, m_y magnitude. The factor β corrects for closure domains magnetized along the x-axis. By substituting Eqs (6.4, 6.5, 6.7), and (6.8) into Eq (6.6), one obtains,

$$x_{amp} \;=\; \left({}^{\mu_0 M_s}\!/_{8\beta}\right) \cdot \left({}^{L}\!/_{c}\right) \cdot H \tag{6.9}$$

This final expression Eq (6.9) has a linear dependence on H, as well as an explicit linear dependence on the edge length L, which is already addressed with reference to the experimental finding. The stiffness parameter c contains geometry-specific information. The hyperbolic decline $c \propto L^{-1.03}$ largely explains the quantitatively observed dependence $x_{\mathrm{amp}} \propto L^{2.09}$. Similarly, the thickness dependence $x_{\mathrm{amp}} \propto d^{-0.81}$ is understood from $c \propto d^{0.84}$.

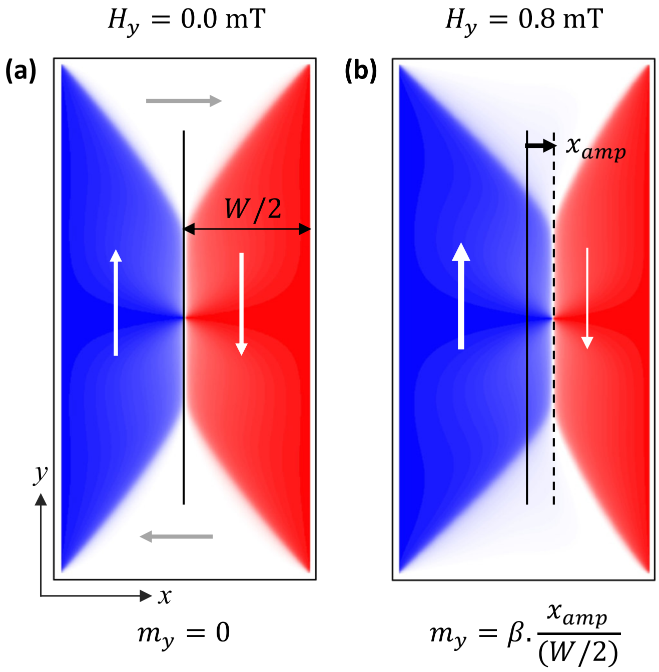

Figure 6.9: DW displacement in terms of m_y in rectangle (L = 5632 nm, W = 2816 nm, and d = 20 nm) at **(a)** zero and **(b)** 0.8 mT fields.

6.5. CONCLUSION

AC-excited domain wall processes play a crucial role in modern domain wall (DW) based microscale devices such as giant-magneto impedance sensors and magnetophoretic circuits and are relevant to minimize core losses in soft magnetic electrical transformer sheets. However, the major challenge in understanding the oscillatory DW dynamics is to track the DW trajectory and amplitude while it is in motion. Successful imaging of such dynamics will implicate deeper insight into the underlying micromagnetic processes and their connection to extrinsic and intrinsic materials properties and the functionality of DW oscillation-based devices.

Chapter 6 presented new imaging approach to investigate nanoscale magnetic domain wall oscillations. For the development of the technique, 180-degree DW of Landau domain pattern induced by an ac-field was directly imaged and analyzed. DW oscillations of low and high frequency were visualized with nanoscale resolution using real-time and time averaged MFM imaging, respectively. For oscillation amplitudes greater than a few micrometers, the time-averaged imaging technique was applied to Kerr microscopy. The developed imaging techniques were able to investigate the oscillation trajectory of the DW and quantify the oscillation amplitude. DW oscillations up to 1 kHz for amplitudes as small as 60 nm were determined using an analytical dwell-time theory and the convolution principle of MFM image formation. Given that both the saturation magnetization and the mobility of permalloy and Cobalt are of the same order of magnitude, the results correspond well with the reported values for this frequency range. Time-averaged imaging can function at frequencies in the megahertz region. However, the increasing inductance of the electromagnetic coils limited the maximum frequency achieved in the present experiments. Consequently, ac-current-induced Oersted fields can be utilized to oscillate the DW in the MHz range. Using the developed imaging approach, the dependence of oscillation amplitude on excitation strength, frequency, and rectangle parameters (size and thickness) was investigated.

The dependencies of the oscillation amplitude on the rectangle's dimensions were discovered via micromagnetic simulations due to the magnetostatically generated restoring force acting on the DW.

Chapter 7 DOMAIN WALL DYNAMICS OF ROLLED MEMBRANES

Continuing the idea of examining DW dynamics in curved structures and expanding knowledge of tubular geometry-induced changes in dynamic magnetic properties, this chapter investigates the impact of rolling-induced anisotropy energy on domain wall dynamics. Knowledge from chapter 5 and 6 on strain-induced anisotropy in microscale elements and time-averaged DW oscillation imaging is used to produce the desired induced anisotropy direction and to image the domain wall oscillations before and after rolling the permalloy rectangle. Micromagnetic simulations support the findings. The scientific development discussed in this chapter was published in the scientific journal listed below[135] and is reproduced here under the terms of license CC BY 3.0:
"B. Singh, R. Ravishankar, J. A. Otálora, I. Soldatov, R. Schäfer, D. Karnaushenko, V. Neu and O. G. Schmidt, Direct imaging of nanoscale field-driven domain wall oscillations in Landau structures, *Nanoscale*, 14, 13667 (2022)".

7.1. MAGNETIC DOMAINS AND DOMAIN WALL OSCILLATIONS

To perform DW dynamics in curved structures with a direct imaging method, the entire magnetic structure must be accessible to microscopy techniques, i.e., sit on the dome of the tubular geometry. To accomplish this, a planar $Ni_{81}Fe_{19}$ rectangle (L = 30 µm, W = 15 µm, and d = 20 nm, rectangle 3 in chapter 6) as shown in Figure **7.1**a.i, was rolled into a curved rectangle (Figure **7.1**b.i) utilizing the self-assembly roll-down approach based on the polymeric platform (Figure **7.1**c). The thin permalloy on top experiences a positive (tensile) stress ($\sigma > 0$) along the rolling direction, which is perpendicular to the rectangle's long axis (Figure **7.1**b.i). With a residual negative magnetostriction ($\lambda < 0$) value of $Ni_{81}Fe_{19}$ and the equation of magnetoelastic energy constant,[33] $K_\mathrm{u} = (3/2)\sigma\lambda$, the strain-induced uniaxial magnetic anisotropy (UMA) constant is negative and thus favors a magnetization orientation perpendicular to the strain direction, i.e., along the long rectangle edge. In its unrolled condition, the rectangle minimizes magnetostatic energy by conforming to the structure's shape, i.e., by producing the previously mentioned Landau pattern (Figure **7.1**a.ii).[31] After self-assembling in a rolled-down, the Kerr image Figure **7.1**b.ii shows that the area of the already existing domains that are aligned along the long axis and are therefore parallel to the UMA, has grown.

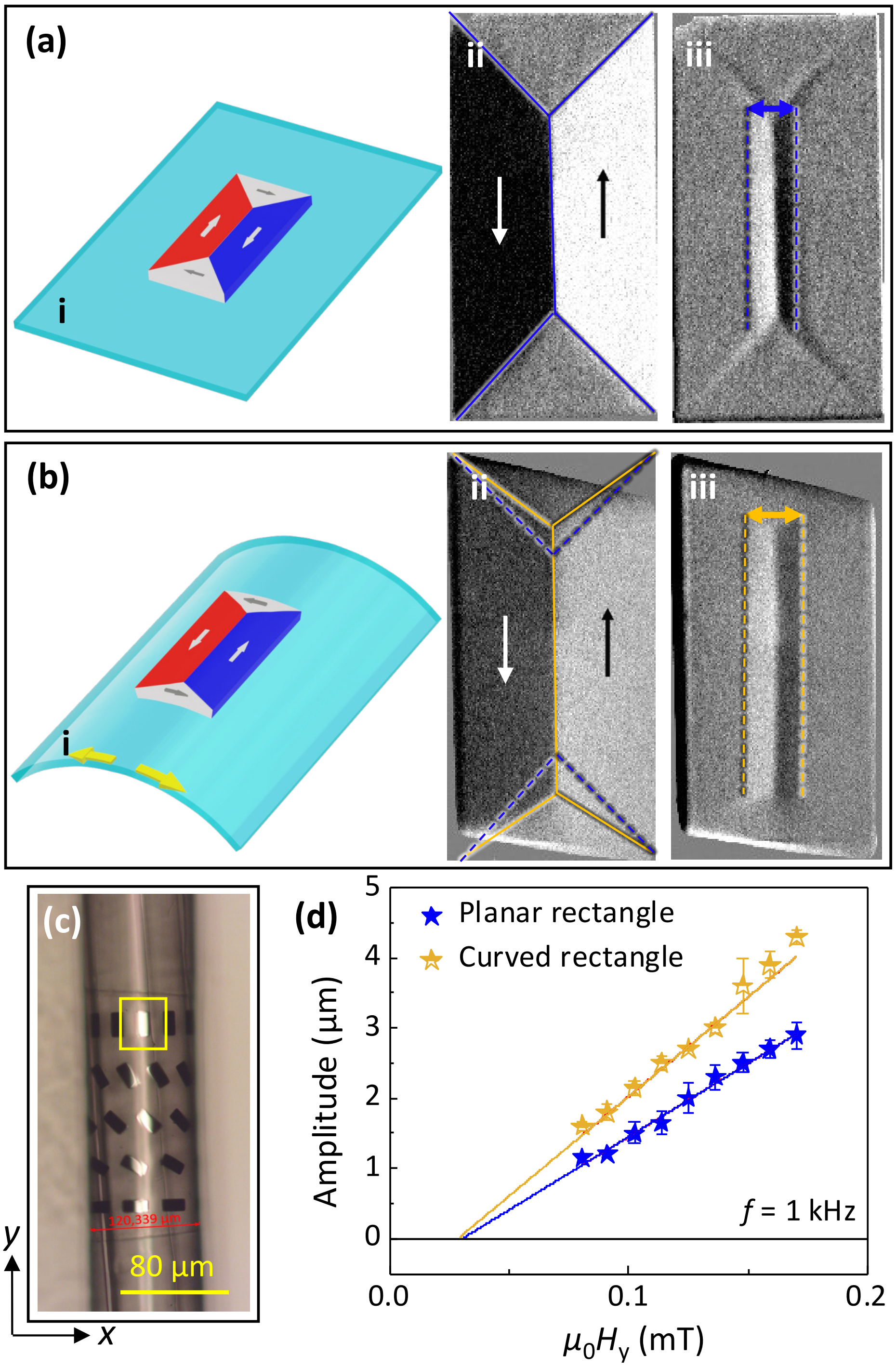

Figure 7.1: Effect of induced uniaxial magnetic anisotropy on DW oscillation amplitude: **(i)** Schematic, **(ii)** static domain, and **(iii)** time-averaged dynamic domain image of a permalloy rectangle placed on top of a polymeric platform **(a)** before rolling and **(b)** after self-assembled rolling down. In b.i, the yellow arrows show the direction of stress in the magnetic structure. **(c)** An optical image of a self-assembled, rolled-down polymeric platform with magnetic structures on it. **(d)** A comparison of the DW oscillation amplitude before and after rolling the rectangle (at a frequency of 1 kHz).

The DW dynamics were investigated using the time-averaged Kerr imaging technique. Comparing the time-averaged dynamic difference images of the rolled structure to those of the unrolled structure immediately reveals the increase in oscillation amplitude (Figures **7.1**a.iii and b.iii). Figure **7.1**d presents a quantitative comparison of the oscillation amplitudes at various field amplitudes. The strain-induced axial magnetic anisotropy clearly favors and enhances the amplitude of the DW oscillation, which is consistent with earlier studies based on global permeability measurements.[140]

7.2. MICROMAGNETIC SIMULATIONS

Micromagnetic simulations for a rectangular structure with L = 5632 nm, W = 2816 nm, and d = 20 nm demonstrate the influence of an induced axial anisotropy in the form of reduced closure domains in the ground state domain configuration and through an increased DW displacement (comparing the Figures **6.10**a and **7.2**a). For a fixed structure size, the DW displacement grows linearly with applied field and monotonically with increasing UMA along the rectangle's long axis (Figure **7.3**a). To obtain a better insight, the DW oscillation amplitude was plotted against the anisotropy magnitude at a fixed field value of 0.1 mT (Figure **7.3**b). Furthermore, an energy ansatz (as described in section 6.4) can explain the experimentally observed and simulated behavior in this scenario, however with a modified stiffness value c'. In short, with an extra UMA along the field direction, larger oscillation amplitudes are the result of a reduced stiffness and thus reduced restoring force.

The details are again approached by micromagnetic simulations. In rectangles with UMA, the equilibrium DW position in the presence of a field is determined by the gain in Zeeman energy density versus the costs involved through the remaining energy terms. To estimate those, the sum of demagnetizing, exchange, and uniaxial anisotropy energy density was evaluated as a function of m_y for small external fields around zero field

(Figure **7.3**c). In all simulations, a quadratic increase in energy density with m_y was observed, which can be represented as

$$E_{ex+demag+UMA} = c_0 + c' \cdot m_y^2, \tag{7.1}$$

where the stiffness parameter c' measures the DW's restoring force when it is displaced from the equilibrium position $m_y = 0$.

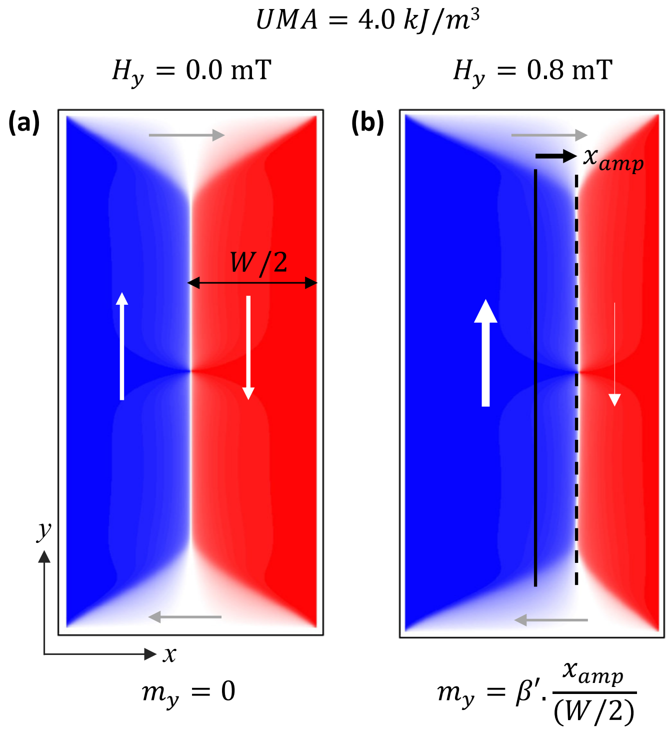

Figure 7.2: DW displacement in terms of m_y in rectangle (L = 5632 nm, W = 2816 nm, and d = 20 nm, UMA = 4.0 kJ[m]$^{-3}$ along the long axis) at **(a)** zero and **(b)** 0.8 mT fields.

The parameter c' for the rectangle as a function of UMA energy density (K_u) is shown in Figure **7.3**d, and it exhibits an exponential decline, which can be expressed as $c' \propto exp\left(\frac{-K_u}{9}\right)$.

The equilibrium DW position x_{amp} can now be determined by taking the minimum of the total energy density,

$$E_{total} = E_{ex} + E_{demag} + E_{Zeeman} + E_{UMA} \tag{7.2}$$

Analog to Eq (6.8) the equilibrium DW position x_{amp} is given by,

$$x_{amp} = \left({}^{\mu_0 M_s}/_{8\beta'}\right) \cdot \left({}^{L}/_{c'}\right) \cdot H \tag{7.3}$$

with c' replacing the former stiffness parameter c. Another small modification concerns the geometry factor β, which corrects for the presence of closure domains. With increasing UMA magnitude along the long element edge, the relative fraction of closure domains reduces. This is seen clearly in Figure **7.1**b.ii, where the size of the closure domains is smaller after the rectangle is bent. The parameter β was thus replaced by β', which now is a weak function of UMA. The effect is however small, and the x_{amp} *vs.* UMA energy density plot (Figure **7.3**b) can be well described by Eq (7.3) with a fixed value of β' as a fitting parameter and the formerly derived expression $c' \propto exp\left({}^{-K_{\mathrm{u}}}/_{9}\right)$.

Eq (7.3) with $c'$and variable β' is used to successfully model the x_{amp} *vs.* UMA energy density plot (Figure **7.3**b).

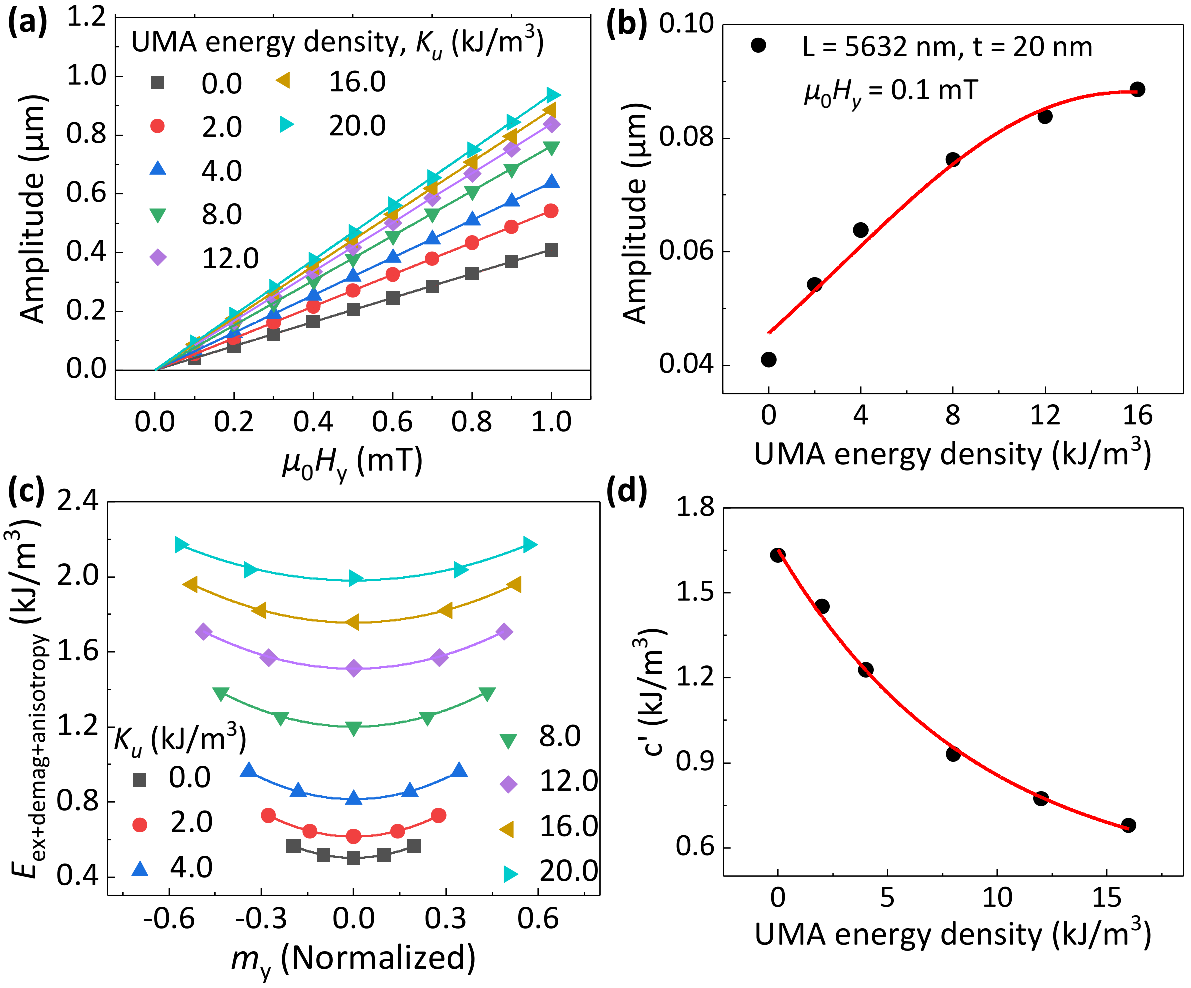

Figure 7.3: Influence of UMA on quasi-static DW dynamics (L = 5632 nm, W = 2816 nm, and d = 20 nm): (a) DW oscillation amplitude as a function of applied magnetic field strength at constant UMA applied along the long axis of the rectangle. **(b)** DW oscillation amplitude at 0.1 mT with increasing UMA energy density, K_{u}. **(c)** The energy density (demagnetizing + exchange + uniaxial magnetic anisotropy) as a function of m_{y}. **(d)**

Stiffness parameter c' vs UMA energy density. The red solid line is a fit to the simulation data, as described in the main text.

7.3. CONCLUSION

Chapter 7 compared DW oscillation in planar and curved rectangles due to the growing interest in DW dynamics in curved geometries, particularly in tubular architectures. The DW oscillation amplitude was found to be increased when the excitation field was applied along the induced-anisotropy direction in the curved rectangle. The energy ansatz explained the increased DW amplitude as a result of a reduced restoring force.

Chapter 8 CONCLUSION & OUTLOOK

In the past decade, magnetic tubular geometries have been the focus of interest due to their promising properties resulting from residual strain, modified exchange and modified magnetostatic interactions, caused by rolling a thin film into a tubular geometry. Understanding the rolling-induced changes in the magnetic domain pattern and domain wall dynamics is crucial for determining and tuning the response of tubular-structure-based microelectronic devices. State-of-the-art experimental studies show that rolling an extended thin film can cause axial, helical, and azimuthal magnetic anisotropies once it adopts the tubular geometry. These observations and theoretical investigations have demonstrated that strain-induced effects and shape-induced magnetostatic interactions are influential on several length scales, whereas curvature- and shape-driven exchange interactions are governed by the gradient of curvature, which for tubular geometries becomes significant only at small radii (hundreds of nanometers and below). Consequently, the induced anisotropy in tubes with a diameter of tens of micrometers is an effective anisotropy resulting from various factors such as magnetostatic interaction between the side edges of the film, strain encountered during rolling, and the shape of the extended thin film. Regarding the DW propagation, theoretical calculations and micromagnetic simulations suggest that DW in cylindrical nanotubes can achieve significantly higher velocities and exhibit magnetochirality due to a geometrically driven symmetry break in the exchange and magnetostatic energy. Whereas the modification due to strain the DW propagation in curved surfaces is not yet explored. The appealing theoretical predictions hold great promise for use in data storage, logic applications, magnetic field sensors and biomedical applications.

This dissertation aims to provide a deep understanding of the various physical causes of different domain configurations in 3D tubular geometries with a diameter of tens of micrometers and demonstrates how to control the domain configuration by tuning the effective magnetic anisotropy. To accomplish this, the influence of strain on the induced anisotropy is separated from other contributions (such as the shape of the film and the magnetostatic interaction) by fabricating magnetic isotropic structures with a width that is small in comparison to the circumference of the tube. As the standard table-top imaging techniques established for imaging the domain pattern of 2D thin film structures are incapable of revealing the structures hidden beneath the 3D polymeric tubular architecture, electrical measurements-based approaches are improved since they are simple and rapid to perform. To address the open question of DW motion, a second part of the dissertation is focused on establishing an imaging technology capable of imaging DW oscillations with nanoscale spatial resolution, as well as applying the developed technique to explore the curvature/strain-induced modification of DW oscillations.

8.1. INDUCED ANISOTROPIES IN CURVED MAGNETIC MEMBRANES

A self-assembly rolling method based on a polymeric bilayer platform was utilized to controllably bend or roll a functional thin film microstructure. Through this platform, both the sign and amplitude of the applied stress could be adjusted. This method opens a wide range of possibilities for modifying the properties of functional materials for micron-sized devices. Controlled bending/curving of permalloy elements with positive ($Ni_{78}Fe_{22}$) magnetostriction produced strain-induced uniaxial anisotropy in the azimuthal or axial direction. This was instantly apparent in the equilibrium domain state of small structural elements and thus, encourage azimuthal domains in tubular GMI sensors. Due to the fact that permalloy has a measurable anisotropic magnetoresistance, the modified magnetic configuration and reversal behavior in applied fields had a substantial effect on the resistance signal, thus making the AMR measurements possible to quantify the induced uniaxial anisotropy. The established electrical characterization method is simple to perform and capable of revealing the properties of magnetic structures hidden behind the 3D polymer architecture. Furthermore, a permalloy structure placed on a polymeric platform could be employed as a strain gauge in "Swiss-roll" architecture-based devices due to its sensitivity to strains as low as 0.17 % with the possibility of further increasing the sensitivity.

8.1.1. OUTLOOK

After studying strain-induced magnetic anisotropy and developing a means to quantify it, extended magnetic membranes might be self-assembled to form multi-winding tubular geometries. Thus, by selecting the magnetic membrane width and self-assembly rolling diameter appropriately, it may be possible to effectively "close" the membrane and achieve magnetic flux closure irrespective of induced magnetoelastic anisotropies. That would allow for the investigation of the flux-closure impact on the magnetic domain configuration. Furthermore, it would allow studying the factors that affect the strength of the flux-closure formation, such as the membrane's thickness and the distance between its two edges. A deeper comprehension of rolling-induced anisotropies would allow to further improve the performance of field sensors based on GMI. Furthermore, the polymeric layer stack as a controllable straining platform would enable straining and investigation of thin film membranes of various materials, resulting in a major impact on physics and materials science.

8.2. DW OSCILLATIONS IN PLANAR AND CURVED STRUCTURES

Using the ac-field-induced DW motion on permalloy Landau structures, a novel imaging technique was developed for direct imaging of periodic DW oscillations at nanoscale spatial resolution with conventional MFM. For oscillation amplitudes in the micrometer range and beyond, Kerr microscopy observations complemented these investigations. Using an analytical dwell-time theory and the convolution principle of MFM image formation, time-averaged MFM data was modeled and DW oscillations with amplitudes as small as 60 nm were determined. The current experimental ac-field arrangement was limited to 1 kHz frequencies due to an increase in coil inductance and hence a loss in field amplitude at higher frequencies, but the novel imaging technique is expected to work in a much greater frequency range, as long as the domain wall motion remains periodic and the detected phase signal averages during the integration time. However, the method is expected to fail in the frequency range near the cantilever's resonance frequency f_0, because at those frequencies a more complex direct excitation of the cantilever will significantly alter the measuring scheme. Additionally, deviations from a non-sinusoidal DW motion are anticipated to be apparent in the shape of the time averaged MFM profile. A comparable dwell-time function-based model was constructed to analyze time-averaged dynamical difference images acquired by Kerr microscopy. As the image intensity is simply accumulated over time, this approach is independent of the DW frequency as long as the amplitudes are greater than the optical resolution. Using these techniques, it was discovered that the oscillation amplitude of the 180-degree DW in a permalloy Landau structure is constant with frequency (up to 1 kHz) and increases linearly with excitation amplitude. The former indicates that the DW has sufficient mobility to instantly follow the applied field. The current results for this frequency region correlate well with the existing data for Cobalt structures, implying that the DW mobility of $Ni_{81}Fe_{19}$ films is at least 105 m[sec]$^{-1}$[T]$^{-1}$. In addition, the DW oscillation amplitude as a function of magnetic structure size, thickness, and strain-induced uniaxial magnetic anisotropy was investigated. The aforementioned observations were well verified by micromagnetic simulations and could be explained by a simple domain model that describes the excited Landau DW configuration as a forced damped harmonic oscillator, with the restoring force influenced by the size, thickness, and anisotropy of the permalloy structure.

8.2.1. OUTLOOK

Developed time-averaged MFM imaging is a novel imaging approach for probing nanoscale DW dynamics, thus it can be used as an effective tool for characterizing DW motion in nanoscale flat and curved geometries. Nanoscale curved geometries, like zigzag-shaped nanowires and rolled-up nanomembranes, can be studied to learn how their curvature, geometry, confinement and material property affects their DW propagation, to develop novel spintronic devices. In this thesis, time-averaged imaging was employed for DW oscillations up to kHz frequency. Future iterations will use the approach to examine the DW dynamics in the MHz frequency range, induced by the ac current Oersted field. Higher frequency dynamics, for instance, would enable the extraction of material parameters such as the mobility of the DW in materials with high permeability and the mass of the DW when the DW is excited with resonance frequency. Furthermore, direct imaging of DW oscillations from low to high frequency would allow for a more in-depth comprehension of the origin of high frequency DW processes-based phenomena such as giant magnetoimpedance (GMI).

MAGNETIC TEXTURE AS A TOOL FOR PROBING NANOSCALE MECHANICS OF BIOMOLECULES:

Combining the knowledge of rolling-induced anisotropies gained in this thesis with a direct imaging technique to image nanoscale oscillating DWs will pave the way for a novel approach to characterizing the nano-mechanics of biomolecules. Figure 8.1 depicts a conceptual representation of an integrated sensor device for characterizing nanoscale mechanics biomolecules.

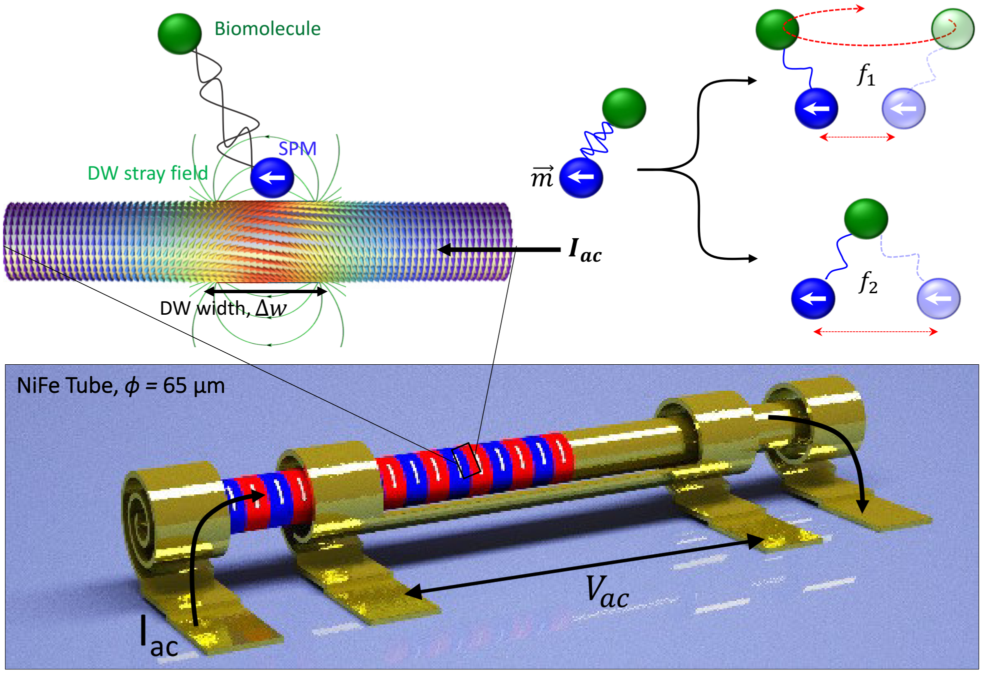

Figure 8.1: Conceptual image of integrated microtubular magneto-mechanical impedance sensor based on ac-current induced oscillating magnetic texture, operating as probing sites for biomechanical studies through the use of biofunctionalized superparamagnetic particles. Magnetic bead oscillating with different characteristic frequencies, f_1, and f_2. Image credit goes to, Dr. Daniil Karnaushenko (MAIN Chemnitz) and Prof. Jorge A. Otálora (UCN Chile).

In section 1.1.2, it is demonstrated how oscillating DW can be utilized to characterize the mechanics of magnetic particles. However, instead of employing a massive electromagnetic coil to drive the DW, the application of a small-amplitude oscillating magnetic stray field would be sufficient to characterize the linear mechanical properties of the attached species. Oersted fields of an alternating electric current and the spin transfer torque (STT) of spin-polarized electrons provide the means to interact with the magnetization of ferromagnetic structures, causing such a displacement in magnetic texture and their stray fields. Intrinsically coupled to mechanical vibrations of the magnetically labeled species the stray field affects back the oscillation of the magnetic texture modifying the electric impedance of the structure. A similar effect is observed in giant magnetoimpedance structures (GMI).[1] For instance, variation in a bio-molecular conformation will affect mechanical motion of the nanoparticle-molecular assembly such as losses, resonances or phase shifts that can be detected in an impedance spectrum of the structure. Application of tube-like structures increases the domain wall velocity up to about two orders of magnitude and possesses stronger coupling with the Oersted field of an AC current than in thin-films. This effect can be explored in a broad range of frequencies being dependent on several material factors, biasing fields and excitation conditions. Using magnetic and electric biases the magnetic state of the structure can be altered enabling simultaneous manipulation of nano-scale objects and mechanical characterization. Being developed this device would allow an acquisition of a complex valued spectrum of mechanical oscillations probed at the frequency range (> 1 kHz) not accessible by state-of-the-art techniques. The realization of a purely electrical (no external bulky devices, optical setup, magnets, or coils) excitation and detection method will provide the field of bio-medicine with a unique nano-mechanic testing capability.

Bibliography

1. Karnaushenko, D. *et al.* Self-Assembled On-Chip-Integrated Giant Magneto-Impedance Sensorics. *Adv. Mater.* **27**, 6582–6589 (2015).

2. Melzer, M. *et al.* Imperceptible magnetoelectronics. *Nat. Commun.* **6**, 1–8 (2015).

3. Rivkin, B. *et al.* Electronically integrated microcatheters based on self-assembling polymer films. *Sci. Adv.* **7**, eabl5408 (2021).

4. Rivkin, B. *et al.* Shape-Controlled Flexible Microelectronics Facilitated by Integrated Sensors and Conductive Polymer Actuators. *Adv. Intell. Syst.* **3**, 2000238 (2021).

5. Becker, C. *et al.* Self-assembly of highly sensitive 3D magnetic field vector angular encoders. *Sci. Adv.* **5**, 1–11 (2019).

6. Becker, C. *et al.* A new dimension for magnetosensitive e-skins: active matrix integrated micro-origami sensor arrays. *Nat. Commun.* **13**, 1–11 (2022).

7. Wyllie, R., Kauer, M., Smetana, G. S., Wakai, R. T. & Walker, T. G. Magnetocardiography with a modular spin-exchange relaxation-free atomic magnetometer array. *Phys. Med. Biol.* **57**, 2619–2632 (2012).

8. Hari, R. & Salmelin, R. Magnetoencephalography: From SQUIDs to neuroscience. Neuroimage 20th Anniversary Special Edition. *Neuroimage* **61**, 386–396 (2012).

9. Kondo, M. *et al.* Imperceptible magnetic sensor matrix system integrated with organic driver and amplifier circuits. *Sci. Adv.* **6**, 1–11 (2020).

10. Melzer, M. *et al.* Elastic magnetic sensor with isotropic sensitivity for in-flow detection of magnetic objects. *RSC Adv.* **2**, 2284–2288 (2012).

11. Melzer, M. *et al.* Direct transfer of magnetic sensor devices to elastomeric supports for stretchable electronics. *Adv. Mater.* **27**, 1333–1338 (2015).

12. Lim, B., Vavassori, P., Sooryakumar, R. & Kim, C. Nano/micro-scale magnetophoretic devices for biomedical applications. *J. Phys. D. Appl. Phys.* **50**, 033002 (2017).

13. Saitoh, E., Miyajima, H., Yamaoka, T. & Tatara, G. Current-induced resonance and mass determination of a single magnetic domain wall. *Nature* **432**, 203–206 (2004).

14. Donolato, M. *et al.* On-Chip Manipulation of Protein-Coated Magnetic Beads via

Domain-Wall Conduits. *Adv. Mater.* **22**, 2706–2710 (2010).

15. Rapoport, E., Montana, D. & Beach, G. S. D. Integrated capture, transport, and magneto-mechanical resonant sensing of superparamagnetic microbeads using magnetic domain walls. *Lab Chip* **12**, 4433–4440 (2012).

16. Mallary, M., Torabi, A. & Benakli, M. One terabit per square inch perpendicular recording conceptual design. *IEEE Trans. Magn.* **38**, 1719–1724 (2002).

17. Marchon, B. & Olson, T. Magnetic spacing trends: From LMR to PMR and beyond. *IEEE Trans. Magn.* **45**, 3608–3611 (2009).

18. Moser, A. *et al.* Magnetic recording: Advancing into the future. *J. Phys. D. Appl. Phys.* **35**, (2002).

19. Parkin, S. S. P., Hayashi, M. & Thomas, L. Magnetic Domain-Wall Racetrack Memory. *Science (80-.).* **320**, 190–194 (2008).

20. Beach, G. S. D., Tsoi, M. & Erskine, J. L. Current-induced domain wall motion. *J. Magn. Magn. Mater.* **320**, 1272–1281 (2008).

21. Yan, M., Andreas, C., Kákay, A., García-Sánchez, F. & Hertel, R. Fast domain wall dynamics in magnetic nanotubes: Suppression of Walker breakdown and Cherenkov-like spin wave emission. *Appl. Phys. Lett.* **99**, 2011–2014 (2011).

22. Yershov, K. V. *et al.* Geometry-induced motion of magnetic domain walls in curved nanostripes. *Phys. Rev. B* **98**, 1–6 (2018).

23. Giordano, M. C., Escobar Steinvall, S., Watanabe, S., Fontcuberta I Morral, A. & Grundler, D. Ni80Fe20nanotubes with optimized spintronic functionalities prepared by atomic layer deposition. *Nanoscale* **13**, 13451–13462 (2021).

24. Schäfer, R., Soldatov, I. & Arai, S. Power frequency domain imaging on Goss-textured electrical steel. *J. Magn. Magn. Mater.* **474**, 221–235 (2019).

25. Richert, H. *et al.* Dynamic Magneto-Optical Imaging of Domains in Grain-Oriented Electrical Steel. *steel Res. Int.* **87**, 232–240 (2016).

26. Harti, R. P. *et al.* Dynamic volume magnetic domain wall imaging in grain oriented electrical steel at power frequencies with accumulative high-frame rate neutron dark-field imaging. *Sci. Rep.* **8**, 1–7 (2018).

27. Stephen Blundell. Magnetism in Condensed Matter. *Oxford Univ. Press* 80–81 (2001).

28. Dubuisson, J., Fehlmann, A. & Petignat, P. Management of presumed benign giant

ovarian cysts: A minimally invasive technique using the alexis laparoscopic system. *J. Minim. Invasive Gynecol.* **22**, 540 (2015).

29. Kalubowilage, M., Janik, K. & Bossmann, S. H. Magnetic nanomaterials for magnetically-aided drug delivery and hyperthermia. *Appl. Sci.* **9**, (2019).

30. Feynman, R. P., Leighton, R. B. & Sands, M. The Feynman Lectures on Physics, Vol. II. *US: California Inst. of Technology.* 37.5–37.6 at (1963).

31. Hubert, A. Schäfer, R. *Magnetic Domains: The Analysis of Magnetic Microstructures*. (Springer, Berlin, 1998).

32. Malinowski, G., Boulle, O. & Kläui, M. Current-induced domain wall motion in nanoscale ferromagnetic elements. *J. Phys. D. Appl. Phys.* **44**, 384005 (2011).

33. Cullity, B. D. & Graham, C. D. *Introduction to Magnetic Materials*. (John Wiley & Sons, Inc., 2008). doi:10.1002/9780470386323.

34. Chikazumi, Stanley H. Charap, S. *Physics of Magnetism*. (Wiley, 1964).

35. Bozorth, R. M. The permalloy problem. *Rev. Mod. Phys.* **25**, 42–48 (1953).

36. Beach, G. S. D., Nistor, C., Knutson, C., Tsoi, M. & Erskine, J. L. Dynamics of field-driven domain-wall propagation in ferromagnetic nanowires. *Nature Materials* vol. 4 741–744 at https://doi.org/10.1038/nmat1477 (2005).

37. Nakatani, Y., Thiaville, A. & Miltat, J. Faster magnetic walls in rough wires. *Nat. Mater.* **2**, 521–523 (2003).

38. Atkinson, D. *et al.* Magnetic domain-wall dynamics in a submicrometre ferromagnetic structure. *Nat. Mater.* **2**, 85–87 (2003).

39. Schryer, N. L. & Walker, L. R. The motion of 180° domain walls in uniform dc magnetic fields. *J. Appl. Phys.* **45**, 5406–5421 (1974).

40. Bocklage, L. *et al.* Time-resolved imaging of current-induced domain-wall oscillations. *Phys. Rev. B - Condens. Matter Mater. Phys.* **78**, 3–6 (2008).

41. Bedau, D. *et al.* Detection of current-induced resonance of geometrically confined domain walls. *Phys. Rev. Lett.* **99**, 5–8 (2007).

42. Van Waeyenberge, B. *et al.* Magnetic vortex core reversal by excitation with short bursts of an alternating field. *Nature* **444**, 461–464 (2006).

43. Khan, M. I. *et al.* Current-induced domain wall oscillations in a nanowire imaged by time-resolved photoemission electron microscopy. *J. Magn. Magn. Mater.* **476**, 538–545 (2019).

44. Möller, M., Gaida, J. H., Schäfer, S. & Ropers, C. Few-nm tracking of current-driven magnetic vortex orbits using ultrafast Lorentz microscopy. *Commun. Phys.* **3**, 36 (2020).

45. Neudert, A., McCord, J., Chumakov, D., Schäfer, R. & Schultz, L. Small-amplitude magnetization dynamics in permalloy elements investigated by time-resolved wide-field Kerr microscopy. *Phys. Rev. B* **71**, 134405 (2005).

46. Chumakov, D. *et al.* Nanosecond time-scale switching of permalloy thin film elements studied by wide-field time-resolved Kerr microscopy. *Phys. Rev. B* **71**, 014410 (2005).

47. Urs, N. O. *et al.* Advanced magneto-optical microscopy: Imaging from picoseconds to centimeters - imaging spin waves and temperature distributions (invited). *AIP Adv.* **6**, 055605 (2016).

48. Schäfer, R. Investigation of Domains and Dynamics of Domain Walls by the Magneto-optical Kerr-effect. in *Handbook of Magnetism and Advanced Magnetic Materials* (John Wiley & Sons, Ltd, 2007). doi:10.1002/9780470022184.hmm310.

49. Topping, C. V. & Blundell, S. J. A.C. susceptibility as a probe of low-frequency magnetic dynamics. *J. Phys. Condens. Matter* **31**, 013001 (2019).

50. Kataja, M. & van Dijken, S. Magneto-optical Kerr effect susceptometer for the analysis of magnetic domain wall dynamics. *Rev. Sci. Instrum.* **82**, 103901 (2011).

51. Gross, K., Westerholt, K. & Zabel, H. Domain wall dynamics of periodic magnetic domain patterns in Co 2 MnGe-Heusler microstripes. *New J. Phys.* **18**, 033007 (2016).

52. Betancourt, I., Valenzuela, R. & Vazquez, M. Giant magnetoimpedance in Co-based microwires at low frequencies (100 Hz–13 MHz). *J. Appl. Phys.* **91**, 8423 (2002).

53. Valenzuela, R. & Betancourt, I. Giant magnetoimpedance, skin depth and domain wall dynamics. in *IEEE International Digest of Technical Papers on Magnetics Conference* vol. 38 CD1 (IEEE, 2002).

54. Sánchez, M. L., Betancourt, I., Valenzuela, R. & Hernando, B. Frequency evolution of the magnetoimpedance effect in stress annealed Co-rich amorphous ribbons. *Appl. Phys. A Mater. Sci. Process.* **81**, 1299–1301 (2005).

55. Betancourt, I. & Valenzuela, R. Magnetization Dynamics of Pinned Domain Walls in Partially Crystallized Ribbons. *IEEE Trans. Magn.* **33**, 3973–3974 (1997).

56. Kataja, M. & Van Dijken, S. Magneto-optical Kerr effect susceptometer for the analysis of magnetic domain wall dynamics. *Rev. Sci. Instrum.* **82**, (2011).

57. Kazakova, O. *et al.* Frontiers of magnetic force microscopy. *J. Appl. Phys.* **125**, 060901 (2019).

58. Yoshimura, S., Zheng, F., Yasui, S., Egawa, G. & Saito, H. AC Magnetic Field Imaging of Perpendicular Magnetic Write Head without Image Distortion on Alternating Magnetic Force Microscopy using a Cone-Shape FePt-coated Tip. *J. Magn. Soc. Japan* **42**, 5–10 (2018).

59. Abe, M. & Tanaka, Y. High frequency write head measurement with the phase detection magnetic force microscope. *J. Appl. Phys.* **89**, 6766–6768 (2001).

60. Koblischka, M. R., Wei, J. D., Kirsch, M. & Hartmann, U. High frequency magnetic force microscopy-imaging of harddisk write heads. *Japanese J. Appl. Physics, Part 1 Regul. Pap. Short Notes Rev. Pap.* **45**, 2238–2241 (2006).

61. Li, Z. *et al.* AC driven magnetic domain quantification with 5â €...nm resolution. *Sci. Rep.* **4**, 1–7 (2014).

62. Streubel, R., Tsymbal, E. Y. & Fischer, P. Magnetism in curved geometries. *J. Appl. Phys.* **129**, (2021).

63. Sheka, D. D. *et al.* Fundamentals of Curvilinear Ferromagnetism: Statics and Dynamics of Geometrically Curved Wires and Narrow Ribbons. *Small* **2105219**, 2105219 (2022).

64. Streubel, R. *et al.* Magnetism in curved geometries. *J. Phys. D. Appl. Phys.* **49**, (2016).

65. Staňo, M. & Fruchart, O. Magnetic Nanowires and Nanotubes. *Handb. Magn. Mater.* **27**, 155–267 (2018).

66. Streubel, R. *et al.* Magnetism in curved geometries. *J. Phys. D. Appl. Phys.* **49**, 363001 (2016).

67. Hertel, R. Curvature-induced magnetochirality. *SPIN* **3**, 1340009–1 (2013).

68. Sheka, D. D., Kravchuk, V. P. & Gaididei, Y. Curvature effects in statics and dynamics of low dimensional magnets. *J. Phys. A Math. Theor.* **48**, 125202 (2015).

69. Gaididei, Y., Kravchuk, V. P. & Sheka, D. D. Curvature effects in thin magnetic shells. *Phys. Rev. Lett.* **112**, 1–5 (2014).

70. Volkov, O. M. *et al.* Experimental Observation of Exchange-Driven Chiral Effects in Curvilinear Magnetism. *Phys. Rev. Lett.* **123**, 077201 (2019).

71. Logic, M. D. Magnetic Domain-Wall Logic. **309**, 1688–1693 (2005).

72. Yan, M., Andreas, C., Kákay, A., García-Sánchez, F. & Hertel, R. Chiral symmetry

breaking and pair-creation mediated Walker breakdown in magnetic nanotubes. *Appl. Phys. Lett.* **100**, 252401 (2012).

73. Otálora, J. A., Yan, M., Schultheiss, H., Hertel, R. & Kákay, A. Curvature-Induced Asymmetric Spin-Wave Dispersion. *Phys. Rev. Lett.* **117**, 1–6 (2016).

74. Bran, C. *et al.* Magnetization Ratchet in Cylindrical Nanowires. *ACS Nano* **12**, 5932–5939 (2018).

75. Fernández-Pacheco, A. & Donnelly, C. The racetrack breaks free from the substrate. *Nat. Nanotechnol.* **17**, 1038–1039 (2022).

76. Landeros, P., Suarez, O. J., Cuchillo, A. & Vargas, P. Equilibrium states and vortex domain wall nucleation in ferromagnetic nanotubes. *Phys. Rev. B - Condens. Matter Mater. Phys.* **79**, 1–10 (2009).

77. Escrig, J., Landeros, P., Altbir, D., Vogel, E. E. & Vargas, P. Phase diagrams of magnetic nanotubes. *J. Magn. Magn. Mater.* **308**, 233–237 (2007).

78. Buchter, A. *et al.* Reversal mechanism of an individual Ni nanotube simultaneously studied by torque and SQUID magnetometry. *Phys. Rev. Lett.* **111**, 1–5 (2013).

79. Rüffer, D. *et al.* Magnetic states of an individual Ni nanotube probed by anisotropic magnetoresistance. *Nanoscale* **4**, 4989–4995 (2012).

80. Weber, D. P. *et al.* Cantilever magnetometry of individual Ni nanotubes. *Nano Lett.* **12**, 6139–6144 (2012).

81. Salinas, H. D., Restrepo, J. & Iglesias, Ò. Change in the magnetic configurations of tubular nanostructures by tuning dipolar interactions. *Sci. Rep.* **8**, 1–15 (2018).

82. Makarov, D. & Sheka, D. D. *Curvilinear micromagnetism*. (Springer International Publishing, 2022).

83. Rüffer, D. Magnetic states and spin-wave modes in single ferromagnetic nanotubes. 108 at (2014).

84. Yan, M., Andreas, C., Kákay, A., García-Sánchez, F. & Hertel, R. Chiral symmetry breaking and pair-creation mediated Walker breakdown in magnetic nanotubes. *Appl. Phys. Lett.* **100**, (2012).

85. Schöbitz, M. *et al.* Fast Domain Wall Motion Governed by Topology and Œrsted Fields in Cylindrical Magnetic Nanowires. *Phys. Rev. Lett.* **123**, 1–6 (2019).

86. Hurst, J. *et al.* Theoretical study of current-induced domain wall motion in magnetic nanotubes with azimuthal domains. *Phys. Rev. B* **103**, 1–13 (2021).

87. Otálora, J. A., López-López, J. A., Landeros, P., Vargas, P. & Nunez, A. S. Breaking of chiral symmetry in vortex domain wall propagation in ferromagnetic nanotubes. *J. Magn. Magn. Mater.* **341**, 86–92 (2013).

88. Körber, L. *et al.* Symmetry and curvature effects on spin waves in vortex-state hexagonal nanotubes. *Phys. Rev. B* **104**, 1–10 (2021).

89. Streubel, R. *et al.* Magnetic Microstructure of Rolled-Up Single-Layer Ferromagnetic Nanomembranes. *Adv. Mater.* **26**, 316–323 (2014).

90. Streubel, R. *et al.* ROLLED-UP PERMALLOY NANOMEMBRANES WITH MULTIPLE WINDINGS. *SPIN* **03**, 1340001 (2013).

91. Li, D., Thompson, R. S., Bergmann, G. & Lu, J. G. Template-based synthesis and magnetic properties of cobalt nanotube arrays. *Adv. Mater.* **20**, 4575–4578 (2008).

92. Chen, J. Y. *et al.* Fabrication and magnetic properties of La-X (X = Co, Ni, and Fe) nanotube arrays prepared by electrodeposition methods. *J. Appl. Phys.* **114**, 054303 (2013).

93. Songmuang, R., Deneke, C. & Schmidt, O. G. Rolled-up micro- and nanotubes from single-material thin films. *Appl. Phys. Lett.* **89**, (2006).

94. Müller, C. *et al.* Tuning magnetic properties by roll-up of Au/Co/Au films into microtubes. *Appl. Phys. Lett.* **94**, 1–4 (2009).

95. Balhorn, F., Jeni, S., Hansen, W., Heitmann, D. & Mendach, S. Axial and azimuthal spin-wave eigenmodes in rolled-up permalloy stripes. *Appl. Phys. Lett.* **100**, (2012).

96. Deneke, C. *et al.* Structural and magnetic properties of an InGaAs/Fe3Si superlattice in cylindrical geometry. *Nanotechnology* **20**, (2009).

97. Bermúdez Ureña, E. *et al.* Fabrication of ferromagnetic rolled-up microtubes for magnetic sensors on fluids. *J. Phys. D. Appl. Phys.* **42**, 055001 (2009).

98. Karnaushenko, D. D., Karnaushenko, D., Makarov, D. & Schmidt, O. G. Compact helical antenna for smart implant applications. *NPG Asia Mater.* **7**, 1–10 (2015).

99. Lee, Y. *et al.* Nano-biosupercapacitors enable autarkic sensor operation in blood. *Nat. Commun.* **12**, 4967 (2021).

100. Li, F. *et al.* Self-Assembled Flexible and Integratable 3D Microtubular Asymmetric Supercapacitors. *Adv. Sci.* **6**, 1901051 (2019).

101. Becker, C. *et al.* Self-assembly of highly sensitive 3D magnetic field vector angular encoders. *Sci. Adv.* **5**, eaay7459 (2019).

102. Karnaushenko, D. *et al.* Biomimetic Microelectronics for Regenerative Neuronal Cuff Implants. *Adv. Mater.* **27**, 6797–6805 (2015).

103. Soldatov, I. V. & Schäfer, R. Selective sensitivity in Kerr microscopy. *Rev. Sci. Instrum.* **88**, 073701 (2017).

104. Soldatov, I. V. *et al.* Advanced, Kerr-microscopy-based MOKE magnetometry for the anisotropy characterisation of magnetic films. *J. Magn. Magn. Mater.* **529**, 167889 (2021).

105. Chizhik, A., Gonzalez, J., Zhukov, A., Gawronski, P. & Stupakiewicz, A. Helical magnetic structures in magnetostrictive amorphous microwires. *Phys. B Condens. Matter* **604**, 412718 (2021).

106. Fischer, P. X-Ray Imaging of Magnetic Structures. *IEEE Trans. Magn.* **51**, 1–31 (2015).

107. Donnelly, C. & Scagnoli, V. Imaging three-dimensional magnetic systems with x-rays. *J. Phys. Condens. Matter* **32**, (2020).

108. Streubel, R. *et al.* Retrieving spin textures on curved magnetic thin films with full-field soft X-ray microscopies. *Nat. Commun.* **6**, 1–11 (2015).

109. Streubel, R. *et al.* Imaging of buried 3D magnetic rolled-up nanomembranes. *Nano Lett.* **14**, 3981–3986 (2014).

110. McGuire, T. R. & Potter, R. I. Anisotropic Magnetoresistance. *IEEE Trans. Magn.* **11**, 1018–1038 (1975).

111. Baumgaertl, K. *et al.* Magnetization reversal in individual Py and CoFeB nanotubes locally probed via anisotropic magnetoresistance and anomalous Nernst effect. *Appl. Phys. Lett.* **108**, (2016).

112. Wang, Z. *et al.* Highly Sensitive Flexible Magnetic Sensor Based on Anisotropic Magnetoresistance Effect. *Adv. Mater.* **28**, 9370–9377 (2016).

113. Zimmermann, M. *et al.* Origin and Manipulation of Stable Vortex Ground States in Permalloy Nanotubes. *Nano Lett.* **18**, 2828–2834 (2018).

114. Wegrowe, J. E., Gilbert, S. E., Kelly, D., Doudin, B. & Ansermet, J. P. Anisotropic magnetoresistance as a probe of magnetization reversal in individual nano-sized nickel wires. *IEEE Trans. Magn.* **34**, 903–905 (1998).

115. Prinz, V. Y. *et al.* Free-standing and overgrown InGaAs/GaAs nanotubes, nanohelices and their arrays. *Phys. E Low-Dimensional Syst. Nanostructures* **6**, 828–831 (2000).

116. Schmidt, O. G. & Eberl, K. Thin solid films roll up into Nanotubes. Nature **410**, 168 (2001).

117. Thurmer, D. J., Bof Bufon, C. C., Deneke, C. & Schmidt, O. G. Nanomembrane-based mesoscopic superconducting hybrid junctions. *Nano Lett.* **10**, 3704–3709 (2010).

118. Smith, E. J. *et al.* Lab-in-a-tube: Ultracompact components for on-chip capture and detection of individual micro-/nanoorganisms. *Lab Chip* **12**, 1917–1931 (2012).

119. Cesar, C. *et al.* Strained Nanomembranes. *Nano* **11**, 3727–3733 (2011).

120. Karnaushenko, D. Shapeable microelectronics. 108 (2016).

121. Sáenz, J. J., García, N. & Slonczewski, J. C. Theory of magnetic imaging by force microscopy. *Appl. Phys. Lett.* **53**, 1449–1451 (1988).

122. Sáenz, J. J. *et al.* Observation of magnetic forces by the atomic force microscope. *J. Appl. Phys.* **62**, 4293–4295 (1987).

123. Freeman, M. R. & Choi, B. C. Advances in magnetic microscopy. *Science (80-.).* **294**, 1484–1488 (2001).

124. Schwarz, A. & Wiesendanger, R. Magnetic sensitive force microscopy. *Nano Today* **3**, 28–39 (2008).

125. Asenjo, A., Jaafar, M., Navas, D. & Vázquez, M. Quantitative magnetic force microscopy analysis of the magnetization process in nanowire arrays. *J. Appl. Phys.* **100**, (2006).

126. Li, X. *et al.* Quantitatively probing the magnetic behavior of individual nanoparticles by an AC field-modulated magnetic force microscopy. *Sci. Rep.* **6**, 1–8 (2016).

127. Schäfer, R. *Handbook of Magnetism and Magnetic Materials*. (Springer International Publishing, Cham, 2021). doi:10.1007/978-3-030-63101-7.

128. Kim, W. J., Lee, T. D., Choa, S. H., Seo, S. M. & Lee, K. J. Effect of ac on current-induced domain wall motion. *J. Appl. Phys.* **101**, 7–10 (2007).

129. Thomson, W. XIX. On the electro-dynamic qualities of metals:—Effects of magnetization on the electric conductivity of nickel and of iron. *Proc. R. Soc. London* **8**, 546–550 (1857).

130. Singh, B. *et al.* Self-assembly as a tool to study microscale curvature and strain-dependent magnetic properties. *npj Flex. Electron.* **6**, 76 (2022).

131. Sander, D. The magnetic anisotropy and spin reorientation of nanostructures and

nanoscale films. *J. Phys. Condens. Matter* **16**, R603–R636 (2004).

132. Asai, R. *et al.* Stress-induced large anisotropy field modulation in Ni films deposited on a flexible substrate. *J. Appl. Phys.* **120**, 083906 (2016).

133. Amjadi, M. & Sitti, M. Self-Sensing Paper Actuators Based on Graphite-Carbon Nanotube Hybrid Films. *Adv. Sci.* **5**, 1800239 (2018).

134. Li, X., Ding, G., Ando, T., Shikida, M. & Sato, K. Micromechanical characterization of electroplated permalloy films for MEMS. *Microsyst. Technol.* **14**, 131–134 (2007).

135. Singh, B. *et al.* Direct imaging of nanoscale field-driven domain wall oscillations in Landau structures. *Nanoscale* **14**, 13667–13678 (2022).

136. Nečas, D. *et al.* Determination of tip transfer function for quantitative MFM using frequency domain filtering and least squares method. *Sci. Rep.* **9**, 3880 (2019).

137. Gross, K., Westerholt, K. & Zabel, H. Domain wall dynamics of periodic magnetic domain patterns in Co2MnGe-Heusler microstripes. *New J. Phys.* **18**, (2016).

138. Fukumoto, K. *et al.* Mobility of domain wall motion in the permalloy layer of a spin-valve-like trilayer. *J. Magn. Magn. Mater.* **293**, 863–871 (2005).

139. Konishi, S., Kusuda, T. & Yamada, S. Domain-wall velocity, mobility, and mean-free-path in permalloy films. *IEEE Trans. Magn.* **7**, 722–724 (1971).

140. González, M. T., García, K. L. & Valenzuela, R. Circumferential magnetization curves of Co-rich amorphous wires under tensile stress. *J. Appl. Phys.* **85**, 319–324 (1999).

List of Figures and Tables

Figure 1.1: Field sensors based on magnetoresistance 2
Figure 1.2: Magnetic bead manipulation using domain wall. 4
Figure 1.3: DW dynamics in nanostructures 6
Figure 2.1: Magnetization configuration 12
Figure 2.2: Rotation of spin vectors from one to another neighboring domain in permalloy structures 13
Figure 2.3: Demagnetizing field (H_d) of the bar magnet. 15
Figure 2.4: Schematic view of the mechanism of magnetostriction 17
Figure 2.5: Schematic view of in-plane domain configuration of a magnetic element with positive magnetostriction under (a) tensile and (b) compressive stress 19
Figure 2.6: Magnetic properties of permalloy 20
Figure 2.7: DW dynamics in magnetic nanowires 22
Figure 2.8: Ultrafast Lorentz imaging of vortex dynamics. 24
Figure 2.9: Imaging of periodic wall oscillation processes in a nanocrystalline ribbon ($Fe_{73}Cu_1Nb_3Si_{16}B_7$, thickness, 20 µm). 24
Figure 2.10: Magneto-optical Kerr effect susceptometry measurements. 26
Figure 2.11: Phase diagrams for magnetic nanotubes 29
Figure 2.12: DW dynamics in nanotube. 30
Figure 2.13: Spin waves in nanotube 31
Figure 2.14: Magnetic domain configuration of micro-tubes. 32
Figure 2.15: Giant magnetoimpedance in tubular structures 33
Figure 2.16: Fabrication of nano- and micro-tubes. 34
Figure 2.17: Self-rolled micro-tubes based on the shapeable polymer stack. 35
Figure 2.18: Kerr imaging of 3D structures. 36
Figure 2.19: Schematics of magnetic nanotomography with MTXM and X-PEEM. 37
Figure 2.20: Global characterization of nanotubes. 38
Figure 3.1: Lithography processing of microstructures. 43
Figure 3.2: Micro-structuring process. 43
Figure 3.3: Microscale magnetic rectangles. 44
Figure 3.4: Fabrication of rolled-down and rolled-up magnetic structures with a curved shape 45
Figure 3.5: Fabrication of arrays consisting of self-assembled rolled-down structures. 46
Figure 3.6: Fabrication steps for rolling polymeric platform (with AMR device) downwards. 48
Figure 3.7: Fabrication steps for rolling polymeric platform (with AMR device) upwards. 49
Figure 4.1: Magnetic force microscopy setup 51
Figure 4.2: Topography and magnetic contrast of a permalloy thin-film structure. 52
Figure 4.3: Kerr imaging. 54
Figure 4.4: Kerr microscopy setup and imaging. 55
Figure 4.5: Micromagnetic OOMMF simulations. 57
Figure 4.6: Illustration of subdivision of stripe into cells for the AMR calculations 60

Figure 5.1: Schematics of (a) roll-down and (b) roll-up self-assembly approaches. 63
Figure 5.2: Magnetic domains before and after rolling the elements. 64
Figure 5.3: Hysteresis measurements on a permalloy stripe. 66
Figure 5.4: Magnetization reversal of rolled magnetic stripes 68
Figure 5.5: Magnetization reversal of a rolled-down stripe in a transverse field. 70
Figure 5.6: Rolled-down magnetic stripes with different curvatures. 73
Figure 5.7: Schematic depiction of the neutral axis and cross-section of the functional magnetic layer deposited on top of the polyimide film 75
Figure 5.8: Quantification of strain-induced anisotropy. 76
Figure 5.9: Magnetization reversal of planar permalloy stripes in an axial field [with uniaxial magnetic anisotropy magnitude, K_u = 40 kJ.m^{-3}] 77
Figure 5.10: Estimation of induced uniaxial transverse magnetic anisotropy using simulated AMR hysteresis in the presence of an axial field. 78
Figure 5.11: Magnetization reversal of planar permalloy stripes [L = 8 µm, W = 0.8 µm, d = 100 nm, with uniaxial transverse magnetic anisotropy magnitude, K_u = 12 kJ.m^{-3}] in a transverse field 80
Figure 6.1: Real-time and time-averaged imaging of domain wall oscillations 84
Figure 6.2: Schematic illustration of the time-averaged MFM imaging concept 85
Figure 6.3: Imaging of DW oscillations using MFM 86
Figure 6.4: Mathematical model for dwell time function for the sinusoidal motion of DW 87
Figure 6.5: Time-averaged Kerr imaging of DW oscillation. 91
Figure 6.6: Oscillation amplitude dependency on structure size and thickness 93
Figure 6.7: Oscillation amplitude dependency on structure size and thickness 95
Figure 6.8: Influence of energy (magnetostatic and exchange) densities on DW displacement 97
Figure 6.9: DW displacement in terms of m_y in rectangle. 98
Figure 7.1: Effect of induced uniaxial magnetic anisotropy on DW oscillation amplitude. 102
Figure 7.2: DW displacement in terms of m_y in rectangle 103
Figure 7.3: Influence of UMA on quasi-static DW dynamics. 104
Figure 8.1: Conceptual image of integrated microtubular magneto-mechanical impedance sensor based on ac-current induced oscillating magnetic texture, operating as probing sites for biomechanical studies through the use of biofunctionalized superparamagnetic particles 110

Table 4.1: Material parameters for permalloy used in micromagnetic 56

Selbstständigkeitserklärung

1. Die folgende Promotionsordnung in ihrer gültigen Fassung erkenne ich an:
Bereich Mathematik und Naturwissenschaften - Promotionsordnung vom 23.02.2011

2. Die Promotion wurde an folgendem Institut/an folgender Professur durchgeführt:
Leibniz-Institut für Festkörper- und Werkstoffforschung Dresden

3. Folgende Personen haben die Promotion wissenschaftlich betreut und/oder mich bei der Auswahl und Auswertung des Materials sowie bei der Herstellung des Manuskripts unterstützt:
Prof. Dr. Oliver G. Schmidt
Dr. Volker Neu
Dr. Daniil Karnaushenko
Prof. Dr. Jorge A. Otálora

4. Ich bestätige, dass für meine Person bisher keine früheren, erfolglosen Promotionsverfahren stattgefunden haben. Andernfalls habe ich diesem Antrag eine Erklärung bzw. Nachweise beigelegt, in dem ersichtlich ist, wo, wann, mit welchem Thema und mit welchem Bescheid diese Promotionsversuche stattgefunden haben

5. Ich versichere weiterhin, dass

(a) ich die vorliegende Arbeit mit dem Titel „Magnetic Domains and Domain Wall Oscillations in Planar and 3D Curved Membranes” ohne unzulässige Hilfe Dritter und ohne Benutzung anderer als der angegebenen Hilfsmittel selbst angefertigt habe. Hilfe Dritter wurde nur in wissenschaftlich vertretbarem und prüfungsrechtlich zulässigem Ausmaß in Anspruch genommen. Es sind keine unzulässigen geldwerten Leistungen, weder unmittelbar noch mittelbar, im Zusammenhang mit dem Inhalt der vorliegenden Dissertation an Dritte erfolgt. Insbesondere habe ich nicht die Hilfe einer kommerziellen Promotionsberatung in Anspruch genommen.

(b) die aus fremden Quellen direkt oder indirekt übernommenen Gedanken als solche kenntlich gemacht sind.

(c) ich die vorliegende Arbeit bisher weder im Inland noch im Ausland in gleicher oder ähnlicher Form einer anderen Prüfungsbehörde zum Zwecke einer Promotion oder eines anderen Prüfungsverfahrens vorgelegt habe.

6. Mir ist bekannt, dass die Nichteinhaltung dieser Erklärung oder unrichtige Angaben zum Verfahrensabbruch oder zum nachträglichen Entzug des Doktortitels führen können.

……………………………………	…………………………………………
Ort, Datum	Unterschrift

Acknowledgements

Here, I would like to express my gratitude to the several individuals whose guidance and support was essential to the completion of my Ph.D. work.

I would like to express my deepest gratitude to my supervisor Prof. Dr. Oliver G. Schmidt (head of the research center MAIN, Chemnitz), for providing me the opportunity to investigate this fascinating topic, for motivating me, and for consistently supporting the realization of my ideas.

My sincere appreciation goes to my co-supervisors Dr. Volker Neu (head of department for Magnetic Microscopy and Thin Film Devices at Leibniz IFW Dresden), Dr. Daniil Karnaushenko (senior research scientist at research center MAIN, Chemnitz), and Prof. Dr. Jorge A. Otálora (UCN Chile). Who have always been supportive and consistently guided my scientific work and personal growth and helped me grow as a scientist. I feel fortunate to get the opportunity to work with them and to share wonderful personal and professional moments of my life. Working under collaborative supervision on experiments, micromagnetic simulations, and article writing significantly improved my abilities as a researcher.

I am grateful to Prof. Dr. Rudolf Schafer (head of department for Magnetic Microstructures at IFW Dresden) for fruitful discussions about my research and for allowing me to use Kerr microscopy lab at IFW Dresden, where I've completed a large portion of my research projects. I thank him for the administrative help he provided while being the director of the Institute for Integrative Nanosciences at IFW Dresden.

I am grateful to Dr. Andy Thomas (head of department for Spin Transport and Devices at IFW Dresden), who provided me the access to the workstation for performing micromagnetic simulations.

I truly appreciate the technical assistance provided by Dr. Ivan Soldatov and Stefan Pofahl (Leibniz IFW Dresden) in the Kerr microscopy lab, Dr. Martin Hantusch (Leibniz IFW

Dresden) for the XPS characterization of the my samples, Karsten Peukert, Torsten Seidemann, Biscop Uwe, and Ullrich Julian (Leibniz IFW Dresden) for building electromagnetic coil for MFM, Cornelia Krien and Irina Fiering (Leibniz IFW Dresden) for the deposition of metallic thin films, and Kristina Leger (Leibniz IFW Dresden) for polymer synthesis.

Also, thanks to Ronny Engelhard, Carol Schmidt, Sandra Nestler, Martin Bauer, Liesa Raith for maintaining the clean room operational and thereby facilitating our work. I'd like to thank current and former secretaries of the Institute for Integrative Nanosciences, Ines Firlle, Kristina Krummer-Meier, and Julia Abram, for handling all the administrative paperwork.

I am thankful to my collaborator Rachappa Ravishankar for sharing the laboratory workload by assisting in sample preparation and measurements and for fruitful discussions and to Aman for reading this thesis. Many Thanks to Dr. Dmitry Karnaushenko (MAIN, Chemnitz), Tong Kang, Alaleh Mirhajivarzaneh, Dr. Boris Rivkin, Dr. Raphael Doineau, Zehua Dou (TU Dresden), Dr. Christian Saggau, Renato Huber, Dr. Farzin Akbar, Zehua Dou, and Christian Becker for their assistance with sample preparation, measurements, equipment introduction, and interesting work-related conversations. Apart from scientific work, I would like to thank all the current and former colleagues of Institute for Integrative Nanosciences with whom I spent my PhD, shared friendship and enjoyed wonderful time at IFW.

I am grateful to my friends Rachappa, Aleena, Labeesh, Elham, and Aditya for their friendship in my early years in Dresden.
My heartfelt gratitude goes to my close friends Gargi, Kush, Preetam, Sukriti, Maneesha, Warsha, Sabour and Arnab for all the fun we had together outside of working time celebrating festivals and exploring Dresden, and Gargi for reading my research articles. Their Friendship and support made my stay in Dresden unforgettable.

Last but not least, I would like to thank my parents and family members for their never-ending support.

List of Publications

1) Boris Rivkin, Christian Becker, **Balram Singh**, Azaam Aziz, Farzin Akbar, Aleksandr Egunov, Dmitriy D. Karnaushenko, Ronald Naumann, Rudolf Schäfer, Mariana Medina Sánchez, Daniil Karnaushenko, Oliver G. Schmidt, "Electronically integrated micro-catheters based on self-assembling polymer films", *Science Advances*, 7, 51, eabl5408, (2021).

2) **Balram Singh**, Jorge A. Otálora, Tong H. Kang, Ivan Soldatov, Dmitriy D. Karanushenko, Christian Becker, Rudolf Schäfer, Daniil Karnaushenko, Volker Neu and Oliver G. Schmidt, "Self-assembly as a tool to study microscale curvature and strain-dependent magnetic properties". *npj Flex Electron* 6, 76 (2022).

3) **Balram Singh**, Rachappa Ravishankar, Jorge A. Otálora, Ivan Soldatov, Rudolf Schäfer, Daniil Karnaushenko, Volker Neu and Oliver G. Schmidt, "Direct imaging of nanoscale field-driven domain wall oscillations in Landau Structures", *Nanoscale*, 14, 13667 (2022).

List of Presentations

1) **Balram Singh**, "Magnetic textures as a tool to study nano-mechanics of biomolecules" IMW-Leibniz IFW Dresden Workshop, **poster** presentation, Wittenberg, Germany, Feb. 2019.

2) **Balram Singh**, "Magnetic textures as a tool to study nano-mechanics of biomolecules" 1st Ph.D. seminar, **oral** presentation, Leibniz-IFW Dresden, Germany, 17th Jun. 2019.

3) **Balram Singh**, "Magnetic textures as a tool to study nano-mechanics of biomolecules" Summer school of the CRC 1261: Magnetic sensing and applications in medicine and industry – state-of-the-art and new prospects, poster flash presentation and **poster** presentation, Kiel, Germany, Aug. 2019.

4) **Balram Singh**, "Imaging nanoscale domain wall oscillations in thin film ferromagnetic structures", Annual IFW Summer School for Ph.D. students, **poster** presentation, Szczecin, Poland, Sep. 2019.

5) **Balram Singh**, "Towards probing nano-scale mechanics using magnetic domain wall" 2nd Ph.D. seminar, **oral** presentation, Leibniz-IFW Dresden, Germany, 16th Apr. 2021.

6) **Balram Singh**, "Magnetic domains and domain wall oscillations in planar and rolled microstructures" 3rd Ph.D. seminar, **oral** presentation, Leibniz-IFW Dresden, Germany, 20th May 2022.

7) **Balram Singh**, "Tuning strain-induced anisotropy of soft ferromagnetic structures", IIN-Leibniz IFW Dresden Seminar, **oral** presentation, Holzhau, Germany, Jun. 2022.

8) **Balram Singh**, "Tuning strain-induced anisotropy of soft ferromagnetic structures", Joint European Magnetic Symposia (JEMS) conference, **oral** presentation, Warsaw, Poland, Jul. 2022.

9) **Balram Singh**, “Self-assembly as a tool to study strain-dependent magnetic properties”, Magnetism and Magnetic Materials (MMM) conference, **oral** presentation, Minneapolis, USA, Nov. 2022.

10) **Balram Singh**, “Direct imaging of nanoscale field-driven domain wall oscillations in Landau structures”, American Physics Society (APS) March meeting conference, **oral** presentation, Las Vegas, USA, Mar. 2023 (upcoming).

11) **Balram Singh**, “Self-assembly as a tool to study microscale curvature and strain-dependent magnetic properties”, American Physics Society (APS) March meeting conference, **poster** presentation, Las Vegas, USA, Mar. 2023 (upcoming).

Curriculum Vitae

Personal Information

Name:	Balram Singh
Date of birth:	4th September 1995
Place of birth:	Arjunpur, Chitrakoot, India
Nationality:	Indian

Scientific Education

Since Sep. 2018	**PhD candidate** at Leibniz IFW Dresden, Institute for Integrative Nanosciences **Topic:** *Magnetic Domains and Domain Wall Oscillations in Planar and 3D Curved Membranes* **Supervisors:** Prof. Dr. Oliver G. Schmidt Dr. Volker Neu Dr. Daniil Karnaushenko Prof. Dr. Jorge A. Otálora
Jul. 2017 – Jul. 2018	**Junior Research Fellow** at Indian Institute of Technology (IITD)
Jul. 2015 - Apr. 2017	**Master of Science** in Physics at the Indian Institute of Technology Bombay (IITB) **Topic:** *Structural and magnetic properties of transition metal compounds* **Supervisor:** Prof. Dr. Avinash V. Mahajan
Jul. 2012 – Apr. 2015	**Bachelor of science** in Physics at the University of Delhi (DU)